Multi-Messenger Indirect Dark Matter Searches in Milky Way Satellites

RAEES NOORBHAI

University of the Witwatersrand
Centre for Astrophysics
rnoorbhai@gmail.com

Supervised by Dr Geoffrey Beck
University of the Witwatersrand
Centre for Astrophysics
geoffrey.beck@wits.ac.za

September 2023

Dissertation submitted to the School of Physics of the University of the Witwatersrand, in fulfillment of the academic requirements of the Master of Science postgraduate degree

Abstract

First suggested 90 years ago, the Dark Matter (DM) mystery has been deepened by a range of astronomical observations, from the galactic to the cosmological scale, demonstrating anomalous gravitational phenomena which necessitate the existence of some unknown DM. In the 1970s, particle DM models, including the WIMP hypothesis considered in this work, were proposed and have subsequently been subjected to empirical scrutiny. Over the past 2 decades, all DM direct detection experiments, collider searches and indirect detection searches have failed to detect a DM signal, placing stringent constraints upon WIMP parameters and ruling out WIMP-Hadron interactions. Following the detection of an excess $e-/e^{+}$ flux at approximately 1.4 TeV by DAMPE in 2017, a number of Massive Leptophilc Majorana Particle (MLMP) WIMP hypotheses were proposed to explain the flux. To conduct a model-independent test of these hypotheses, Leptophilic WIMPs in the 1-2 TeV mass-energy range are considered, accounting for self-Annihilation along all leptonic channels, as well as the 3l democratic case. The dwarf spheroidal galaxies orbiting the Milky Way (MW), particularly the Ultrafaints, are DM-dominated and are thus strong candidates for indirect DM searches using next-generation telescopes - such as CTA in gamma, KM3NeT in neutrinos and MeerKAT in radio, with sensitivities that dwarf those of prior telescopes like LHAASO. Accounting for the respective fields-of-view of these telescopes, 6 dwarf spheroidals, 4 Ultrafaints and 2 Classicals, are chosen as potential target environments for the multi-messenger analysis. Equations are also derived for the Mean Free Path (MFP) and Mean Annihilation Period (MAP) of the WIMPs in the respective DM Halos, for the case of both an arbitrary Halo boundary and at the virial radius boundary. Utilising conservative estimates of telescope sensitivities, non-detection upper bounds are placed upon the Annihilation cross-section $\langle\sigma v\rangle_{\psi}$ and Decay rate Γ_{ψ}. These bounds are taken in comparison to the bounds imposed by the Super-Kamiokande neutrino search in the MW Halo and centre, the ATCA radio search in Reticulum II and the ASKAP/EMU radio search in the LMC. In all cases, the non-detection bounds imposed by observations of the Ultrafaints are more stringent, but with greater error margins than is the case with the Classicals. For CTA, non-detection bounds in the case of all Ultrafaints are competitive with those imposed by the ASKAP/EMU search and stronger than those imposed by both the ATCA and the Super-Kamiokande searches. For KM3NeT, no novel non-detection bounds are imposed for observations of all 6 dwarf spheroidals. For MeerKAT, in the case of the μ^{-}/μ^{+} channel, observations of Reticulum II are competitive with the ASKAP/EMU bounds. From the multi-messenger analysis, it is concluded that the strongest non-detection bounds are imposed by CTA observations of Segue 1 and MeerKAT observations of Reticulum II. In the Decay case, the bounds are compared to those imposed by the Fermi indirect search in the IGRB. In the case of all next-generation telescopes, no novel non-detection constraints can be imposed upon Γ_{ψ}. In the case of the MFP and MAP results, the non-detection lower limits are often many orders of magnitude greater the Hubble time. At the relic density limit, the Halo-independent MAP at the virial limit is 14 orders of magnitude greater than the age of the Universe. This illustrates the severe extent to which the Annihilation channel for WIMPs has been suppressed, since successive instances of non-detection have placed tight bounds on $\langle\sigma v\rangle_{\psi}$. In light of this, proposed astrophysical explanations for the DAMPE flux are favourable, as they do not require the presupposition of WIMP Dark Matter.

Dedication and Acknowledgments

For Raees at six years old, dreaming out loud about being a scientist one day. This one's for you.

With boundless gratitude to Dr. Geoffrey Beck. For his insight, feedback and guidance. For his understanding, sympathy and patience. And for a kindness all too rare, in a world where cruelty is too often normalised.
To have conducted this research under his supervision has been nothing short of a blessing.

With many thanks too to my father, Mubeen Noorbhai, for his repeated assistance in dealing with the unique way in which my work is obstructed by the deafening nag of a cigarette craving.

And lastly, with much gratitude to my mother, Yasmeen Omar, for her needed material support and, more importantly, for always taking my calls at odd hours of the morning when I have to share with someone the overwhelming joy of finding out something new.

Contents

I. Introduction

Dark Matter (DM) dominates the matter content of the Cosmos, from the galactic scale to that of the particle horizon, yet questions around its nature and properties remain open and pressing. First suggested over 80 years ago by Fritz Zwicky [1], DM constitutes approximately 25 percent of all mass-energy in the Universe [2]. Since Zwicky's observation of the Coma Cluster's missing mass in the early 1930s [1], anomalies from different sources - multiple observations of unexpected galaxy rotation curves as in [3], along with the studies of the stability of disk galaxies as in [4], began to necessitate the existence of an unobserved DM halo, as suggested by Zwicky [1]. Moreover, in order to account for observations of the Cosmic Microwave Background (CMB) radiation (see [5] [6] [7]) and to account for structure formation in the early Universe, the existence of an unobserved 'Cosmological Dark Matter', which constitutes the majority of the Universe's mass content, became necessary [8]. The interactions of this substance with ordinary (Baryonic) matter are overwhelmingly and primarily through gravitation, and so the gravitational implications of its existence alone can theoretically account for the aforementioned gravitational anomalies observed through the 20th Century [9].

However, beyond its bulk mass properties, we have no firm understanding of this mysterious, invisible substance. A number of hypothetical extensions to the Standard Model that conceptualise DM as a particle have been proposed, notably with the introduction in 1977 of heavy neutral particles which would have observable interactions on the scale of the Weak force [10] [11]. This Weakly Interacting Massive Particle (WIMP) hypothesis is the most extensively studied contender for particle DM and is the DM model under consideration in this work [2]. Yet with each passing experiment, the empirical ground is shrinking beneath its feet.

Collider searches [12] [13] [14] and Direct detection experiments [15] [16] [17] have thus far failed to detect any WIMPs, ruling out the hypothetical particle over significant mass ranges and imposing stringent constraints, particularly with respect to WIMPs that couple to Standard Model (SM) Hadrons. This led to the postulation of DM particles with no hadronic interactions, interacting exclusively with Standard Model (SM) leptons at tree-level, as laid out in [2]. DM indirect detection is capable of constraining the annihilation cross-section and decay rate of these Leptophilic WIMPs by searching for the products of DM Annihilation and Decay.

A set of such Leptophilic WIMP models [18] [19] [20] were put forward to account for the detection of the excess electron/positron flux at approximately 1.4 TeV by Wukong, the Dark Matter Particle Explorer, in 2017 [21]. These models must now be tested in the context of new observational targets. The dwarf spheroidal galaxies which orbit the Milky Way are chosen as observational targets for the multi-messenger indirect search. These ancient dwarf spheroidal galaxies are DM dominated, with high mass-to-luminosity ratios, and are thus prime targets of observation for multi-messenger indirect DM searches [22].

Through simulating the expected indirect emissions from DM annihilation or decay in the gamma ray, radio and neutrino domains, we can utilize the predicted sensitivities of upcoming multi-messenger experiments, including the expected performance of MeerKAT, to calculate non-detection constraints by these next-generation telescopes. The projected non-detection upper limits upon $\langle \sigma v \rangle_{\psi}$ are compared to those imposed by previous searches using ATCA in radio [23] and Super-Kamiokande in neutrinos [24]. Projected non-detection constraints by LHAASO are also calculated as a point of comparison. The constraints imposed are a metric of both the suitability of

Ultrafaint dwarf spheroidal galaxies as suitable observational targets for DM indirect detection, along with the large extent to which detector sensitivities, in multiple observational domains, have improved, allowing them to probe deeper into the nature of DM through indirect detection experiments.

Through calculating the consequences of non-detection for multi-messenger observations in the case of each target dwarf galaxy, we can suggest the optimal combinations of telescope and target galaxy to impose the most stringent constraints upon the WIMP parameter space, primarily with respect to the Annihilation channel, since the Decay channel is highly suppressed in the WIMP model under consideration. We nonetheless calculate the decay rate upper limits and utilise the Γ_ψ non-detection constraint from the Fermi indirect search in the Isotropic Gamma Ray Background as a point of comparison [25].

The large extent to which the Decay channel has been suppressed can be contextualised through comparison of the Decay lifetime (the inverse of the Decay rate) to the Hubble time. In order to afford us a similar point of comparison for the Annihilation channel, we derive equations for the Mean Free Path ($\langle\lambda\rangle_\psi$) and Mean Annihilation Period $\left(\langle T\rangle_\psi\right)$ for a DM particle in a particular Halo, as a function of both the particle's velocity-averaged Annihilation cross-section and the global properties of the Halo environment. Through linking the particle physics to the physics governing the macroscopic properties of the Halo, we can describe the kinematic behaviour of the WIMPs, calculating the Mean Annihilation Period and affording us a physical interpretation of the Annihilation cross-section constraints. Like the Decay lifetime, the Mean Annihilation Period can be contextualised through comparison to the age of the universe.

This work begins with a a review of the relevant body of literature in Chapter 2, beginning with a sub-chapter synthesising the salient points in the history of the Dark Matter mystery into a coherent historical overview of the Dark Matter paradigm and the means through which we've attempted to solve the *Mystery of the Missing Mass*, along with the testable consequences of these hypotheses and the extent to which they have been empirically constrained. The literature review thereafter expands and elaborates upon aspects of the historical overview in the first sub-chapter, beginning with a sub-chapter on Collider searches and Direct detection experiments, followed by a sub-chapter on indirect detection, juxtaposed by the preceding sub-chapter to motivate indirect detection as a means through which we can probe the remaining regions of the WIMP parameter space which cannot be probed by Collider and Direct detection experiments.

In the next sub-chapter, our analysis on DM indirect detection is extended through consideration of the unexplained e^-/e^+ flux detected by Wukong in 2017 [21], along with the Leptophilic WIMP models proposed to explain the flux [18] [19] [20]. This is followed by a sub-chapter exploring existing empirical constraints upon the annihilation channel, imposed by Collider searches, Direct detection and indirect detection. Similarly, the subsequent sub-chapter considers existing constraints upon the Decay channel. In the final two sub-chapters of the literature review, we investigate the suitability of dwarf spheroidal galaxies as observational targets for DM indirect detection and subsequently investigate the discovery potential of next-generation telescopes with unprecedented sensitivities in the gamma ray, radio and neutrino domains.

Chapter three focuses on the theoretical basis of the research, investigating different halo density profiles, conceptualising and defining the astrophysical J- and D-factors, reproducing the derivation for $\langle\sigma v\rangle_\psi$ and Γ_ψ and presenting the derivation of $\langle\lambda\rangle_\psi$ and $\langle T\rangle_\psi$. In the neutrino domain, we also derive equations which account for neutrino oscillations and in the radio domain, it also becomes necessary to extend the theory to account for the fact that we are working with diffuse synchrotron emission, which results when electrons produced via DM Annihilation interact with the magnetic field of the Halo.

Chapter four then goes on to detail the manner in which the theoretical analysis is implemented. In the first sub-chapter, a set of six suitable dwarf spheroidals are motivated as promising observational targets for the purposes of this work. Thereafter, the WIMP Annihilation and Decay spectra, produced using event generators, are discussed, since we utilise them for imposing constraints in the gamma ray and neutrino domains. The next sub-chapter focuses upon imposing constraints with CTA and LHAASO, detailing how the Annihilation and Decay spectra, along with the sensitivity data for the respective telescope, are combined to calculate the projected non-detection constraints for both instruments in the gamma ray domain.

The following sub-chapter focuses upon KM3NeT, with the implementation process differing for telescopes operating within different observational domains. Therefore, the implementation in the neutrino domain differs from the implementation process for CTA and LHAASO, both of which operate within the gamma ray domain. In the case of KM3NeT, the phenomenon of neutrino oscillations must be taken into account when calculating the non-detection constraints. This is achieved through the amendment of the equations for $\langle \sigma v \rangle_{\psi}$ and Γ_{ψ} to reflect the influence of oscillations. These amended equations are then solved, utilising the KM3NeT sensitivity data, to produce the constraints imposed upon the WIMP parameters in the case of non-detection by the KM3NeT.

The implementation process for MeerKAT differs substantially from those in the gamma ray and neutrino domains, since we are searching for synchrotron emission in the radio domain, resulting from the hypothetical production of relativistic electrons through the Annihilation of Leptophilic WIMPs and the subsequent interaction between the electron and the magnetic field of the DM Halo under consideration. Therefore, imposing non-detection constraints in the radio domain requires for us to provide additional information concerning the properties of the Halo environment, including its magnetic field profile, electron gas profile and diffusion environment. In order to compute the constraints imposed by the non-detection of synchrotron emission by MeerKAT, we must again solve amended equations for the WIMP Annihilation cross-section and Decay rate, which must now take into account the necessary theoretical extension required in order to impose constraints in the radio domain.

Having established the methodology for computing constraints in the gamma ray, neutrino and radio domains respectively, a strategy is then formulated for conducting a multi-messenger analysis, comparing the constraints imposed by non-detection for observations with CTA, KM3NeT and MeerKAT, for cases where the chosen target dwarf spheroidal is within the fields of view of our multi-messenger telescopes. The final sub-chapter of Chapter four proposes a strategy for interpreting the bounds on the Mean Free Path and Mean Annihilation Period, both of which are calculated using the equations derived in this work.

Chapter five presents the results and discussions of the projected multi-messenger non-detection constraints, beginning with the non-detection constraints imposed by CTA and LHAASO in the gamma ray domain. This is followed by the projected non-detection constraints using KM3NeT in the neutrino domain and MeerKAT in the radio domain. A multi-messenger analysis is thereafter conducted, comparing the bounds imposed by non-detection utilising the telescopes under consideration in this work, each of which operates within a specific observational domain. The final set of results are obtained by setting $\langle \sigma v \rangle_{\psi}$ to a constant value (which we have chosen as the canonical Annihilation cross-section) and thereafter computing both the Mean Free Path and the Mean Annihilation Period for a subset of dwarf spheroidals, at both the scale and virial radii, utilising the equations derived in this work. These MFP and MAP results are then interpreted through comparison to the Hubble distance and the Hubble time, along with the lower limits imposed upon the WIMP lifetime, τ_{ψ}.

Chapter six goes on to summarise the body of work, highlighting and contextualising its most crucial tenets. The salient conclusions of this work (which are considered in relation to the aims and objectives outlined in the sub-section following this introduction) are also highlighted and situated within the evolving, mysterious Dark Matter paradigm.

In the Appendices, Appendix A investigates alternative, non-Dark Matter explanations for the excess flux detected by Wukong in [21]. Appendix B explores the empirical scaling relations for the J- and D-factors presented in [26], while Appendix C considers the calculated D-factors at the Halo virial radius, solving the equation which emerges from those derived in this work for the WIMP MFP and MAP. Appendix D conducts a brief review of alternative DM hypotheses to WIMPs, while Appendix E presents the error analysis for this work.

Aims and Objectives

- Explore the historical search for Dark Matter, the evidence for its existence and the trajectory of the Dark Matter mystery to the present day.

- Investigate the potential of DM indirect detection, in contrast to DM Direct detection and Collider experiments, in honing in on the properties of DM.

- Investigate dwarf spheroidal galaxies, particularly the Ultrafaints, as target environments for DM indirect detection and based upon this investigation, accounting in particular for the astrophysical J- and D- factors, to select a sample DM-dominant dwarf spheroidals as suitable observational targets for multi-messenger astronomy.

- Explore the potential of next-generation telescopes - CTA, KM3NeT and MeerKAT - for multi-messenger DM indirect detection, in the gamma ray, neutrino and radio domains, utilising published sensitivity data sets. This will be contrasted with the sensitivity of the earlier LHAASO telescope in the gamma ray domain.

- Explore the various Leptophilic WIMP hypotheses put forward to excess DAMPE flux detected in 2017 and formulate a generalized model to be tested in the context of the target dwarf spheroidals.

- Compute upper limits on the Velocity-Averaged Annihilation Cross Section $\langle \sigma v \rangle_\psi$ and the Decay Rate Γ_ψ of the Leptophilic WIMPs (ψ) imposed by non-detection in the case of the various telescopes under consideration.

- Compare: The projected performance of CTA in constraining the parameter space to that of LHAASO; the projected bounds imposed by MeerKAT non-detection to prior bounds set by the indirect radio search by ATCA; the bounds imposed by projected KM3NeT non-detection to those impose by the indirect neutrino search by Super Kamiokande.

- Interpret the non-detection upper bounds and their consequences for the generalised Leptophilic WIMP hypothesis put forward to explain the DAMPE flux, along with the WIMP hypothesis more generally.

- Derive equations for the Mean Free Path $\langle \lambda \rangle_\psi$ and Mean Annihilation Period $\langle T \rangle_\psi$ of WIMPs in the Halo, at both the scale and virial radius, and compute lower limits imposed by non-detection in each case. Thereafter analyze and interpret these lower limits and explore their physical consequences.

- Motivate strategies for observations using multi-messenger astronomy that would be optimal in further constraining the parameter space for the hypothetical DM particle.

- Explore the terrain of alternate hypotheses that have been put forward as candidates for DM.

II. Literature Review

1. A Historical Overview of the Dark Matter Mystery

In 1933, the Swiss Astronomer Fritz Zwicky published a paper in which he highlighted that in order to gravitationally bind the Coma Galaxy Cluster, the actual mass had to be around 2 orders of magnitude larger than the observed mass in stars [1]. Zwicky's anomalous Coma cluster observations were simply the first of many anomalous gravitational phenomena, observed over decades, deepening the mystery of the *"missing mass"*, which remains unsolved to this day, almost 9 decades after Zwicky's Coma cluster observations [1]

The next direct clue for DM came more than 25 years after Zwicky's observations, utilising observations in the optical domain of the Milky Way's neighbouring galaxy: Andromeda [3]. In 1970, Vera Rubin and Kent Ford, Jr published a spectroscopic survey of emission regions in Andromeda, producing rotation curves for Andromeda that ran contrary to expectations for a bound mass distribution [3]. Beyond a certain threshold, as the distance from the galactic centre grew, the rotational velocity remained constant [3].

Also in the early 1970s, radio astronomers at NRAO in Virginia were observing the distribution and motion of neutral hydrogen in the outer regions of galaxies [9]. In 1973, a collaboration between Morton Roberts at NRAO and Arnold Rots at the Dutch Westerbork Synthesis Radio Telescope (WSRT) discovered three galaxies with rotational curves that suggested the presence of a DM Halo with undetected mass at large distances from the galactic centre [27]. They found that the rotational velocity of the gas remains constant with distance from the galactic centre, beyond the visible edge of the galaxy, contrary to what one would expect for a bound mass distribution [9]. These galactic-scale gravitational anomalies observed in the radio domain mirror the gravitational anomalies that were detected three years prior through observations in the optical domain [3].

In the same year that the NRAO/WSRT collaboration discovered the triplet of galaxies with anomalous rotation curves [27], Ostriker and Peebles published a paper in which they claimed, supported by their N-body simulations of disk galaxies, that such galaxies cannot be rotationally-supported, and as such another, massive spheroidal component of the galaxies – an unobserved Dark Matter Halo, stretching beyond the visible region of the galaxy - must exist [4]. Taking this massive Dark Halo into consideration allows for an explanation of the anomalous galaxy rotation curves observed in both the optical [3] and radio [27] domains.

Following the observational and theoretical work on the gravitational anomalies in the early 1970s, two non-Baryonic particle DM models were put forward in 1977, both of which remain contenders for the constituents of the universe's missing mass. The first emerges from the work independently done by Lee and Weinberg on the one hand [10] and Piet Hut on the other [11]. In both [10] and [11], a new, heavy, neutral particle, which interacts on the scale of the Weak nuclear force, is introduced. This class of DM Candidates came to be known has WIMPs (Weakly Interacting Massive Particles), which is the primary DM hypothesis considered in this work.

The second model introduced in 1977 follows from the work of Peccei and Quinn, who theoretically account for Charge Parity Conservation in the case of Strong force interactions [28] and then Weak and EM interactions [29], through introduction of a new scalar field. Although the term isn't used explicitly in the initial papers by Peccei and Quinn, the ultra-light, bosonic quanta of this scalar field came to be known as *Axions* (after a cleaning detergent) which quickly established itself as a strong candidate for particle DM [30].

Departing from the Particle DM paradigm, Mordehai Milgrom published three papers in the Astrophysical Journal in 1983, the first of which lays out a proposed modification of Newtonian dynamics (termed *MOND*) which would hypothetically eliminate the need for particle DM, or indeed any "missing mass" at all [31]. The second explores the consequences of MOND hypothesis for galaxies [32] and the third explores the consequences for galaxy systems [32]. In 1994, Dodelson and Widrow established another non-Baryonic particle DM candidate, *Sterile, Heavy Neutrinos*, by extending their model into the Cold Dark Matter (CDM) paradigm and accounting for structure formation [33].

While the Cosmic Microwave Background (CMB) was first detected in 1965 [5] and accounted for within the framework of Big Bang cosmology in the same volume of the Astrophysical Journal [6], it was decades before the anisotropies were first noticed, requiring a DM component to account for structure formation and thereby allowing for constraints to be imposed upon models for particle Dark Matter. When small fluctuations in the CMB spectrum were first observed, non-Baryonic particle DM candidates like WIMPs and Axions, which interact with photons and matter primarily through gravitation, became necessary to explain Cosmological evolution [8]. Since these hypothetical particles would be decoupled from radiation in the early Universe, this would allow for the formation of structure within the confines of a Hot Big Bang [8].

At the beginning of the 21st century, a multitude of gravitational anomalies, such as galaxy rotation curves observed in both the optical and radio domains which ran contrary to expectations, along with the necessary mass required to bind galaxy clusters and stabilise disk galaxies, had established the need DM for DM super-structures like Zwicky's postulated *Dark Halos*. The CMB anisotropies further bolstered the case for Cosmological particle DM in order to account for structure formation in the universe. It is generally assumed that the Cosmological DM and the DM comprising the Halos are one and the same. Thus, with the existence of DM firmly established, experiments began to constrain the parameters characterising different DM models. Powerful particle colliders like the Large Electron-Positron (LEP) collider and CERN's Large Hadron Collider (LHC) began to probe for physics beyond the Standard Model, attempting to detect a signal on account of the hypothetical Z′ gauge boson [12] [13] [14], which in our case mediates the interaction between the Leptophilic WIMPs and the SM Lepton. However, neither collider has detected a DM signal.

In 2006, the LEP Collider announced that it found no evidence for physics beyond the SM, thereby imposing non-detection constraints upon the mass of Z′ [12]. In 2012, the CMS experiment at the LHC announced no evidence for physics beyond the SM, failing to detect (at centre-of-mass energy $\sqrt{s} = 7$ TeV) any signal consistent with the existence of Z′, thereby strengthening bounds on the parameter space of the mediator boson [13]. In 2014, the LHC's ATLAS experiment confirmed the CMS experiment's non-detection of a signal indicating physics beyond the SM [14]. The ATLAS results include those at $\sqrt{s} = 8$ TeV and so the bounds on the Z′ parameter space are further strengthened [14].

In light of the failure of Collider experiments to detect a DM signal, Direct detection experiments like PANDAX-II, LUX and XENON1T offer another avenue to probe the parameter space. They rely upon the detection of local WIMP-Nucleon scattering events in the detector, presupposing a WIMP with Hadronic interactions [2]. However, in all three cases, no DM signal has been detected.

In 2016, the PANDAX-II collaboration announced that in its first 98.7 days of data, no signal consistent with the existence of WIMPs was detected [17]. The following year, the Large Underground Xenon (LUX) collaboration announced that it too had found no evidence for WIMP-nucleon scattering events [15]. In 2018, the XENON1T experiment announced its failure to detect WIMP-nucleon scattering events as well, producing the most stringent Direct detection constraints upon the WIMP parameter space [16] [34].

Given the consecutive failures by the aforementioned Collider and Direct detection experiments to identify a DM signal, the development of a third avenue - DM indirect detection, employing observational astronomy to detect the products of DM Annihilation or Decay - was a needed one. Indirect searches can potentially probe the WIMP parameter space more deeply than is possible with terrestrial methods like Collider and Direct detection experiments.

Some part of the discovery potential for Indirect detection is reliant upon the choice of a DM-dominated observational target, with the sensitivity of the respective telescope apparatus serving as a limiting factor in constraining the WIMP parameter space. Over the past decade, several Indirect searches, observing a range of target environments, utilising a number of telescopes in different observational domains, have been conducted. However, as was the case for the Collider and Direct detection experiments, no DM signal has been detected to date.

In 2017, an indirect radio search was carried out using the Australia Telescope Compact Array (ATCA), detecting no diffuse synchotron emission from the Ultrafaint dwarf spheroidal galaxy Reticulum II [23], which is also an observational target in this work. In 2020, the Super-Kamiokande collaboration conducted an Indirect neutrino search in 20 years of observational data of the Milky Way halo and centre, finding no DM signal and imposing new upper bounds on $\langle \sigma v \rangle_{\psi}$ for a multitude of Annihilation channels, across a broad mass range [24].

In 2019, a deep indirect gamma search using Fermi, this time with the observational target as Isotropic Gamma Ray Background (GRB), failed to detect a WIMP signal, consequently driving the Decay Rate upper limits downwards and equivalently driving the WIMP mean lifetime lower limits upwards, further illustrating the extreme extent to which the Decay channel has been suppressed [25].

In 2021, Regis et. al. performed an indirect radio search in the Large Magellanic Cloud (LMC) [35]. In line with the Evolutionary Map of the Universe (EMU) survey, they process a deep image taken by ATCA and find no signal that would indicate the occurrence of WIMP Annihilation inside the LMC, thus imposing significant constraints upon the parameter space - eliminating all WIMPs with a mass below 480 GeV, along with all WIMPS which interact with quarks [35]. Thus, it is empirically established in [35] that WIMP-nucleon scattering events cannot occur, since that would require quark interactions and so this result poses challenges to Direct detection experiments which rely upon these interactions. Therefore, the result in [35] is also a vindication of the successive WIMP non-detection results from PANDAX-II [17], LUX [15] and Xenon1T [16]. A key component of the method for DM Indirect detection relies upon the detection of unexplained astrophysical fluxes, with DM models fit to the data so as to account for the unknown signal, which is presupposed to be a consequence of WIMP Annihilation or Decay [2]. As seen in Figure

1, one such excess e^-/e^+ flux at ~ 1.4 TeV was detected by Wukong, China's DArk Matter Partlice Explorer (DAMPE) in 2017 [21].

Following the DAMPE announcement of the excess flux, a number of TeV WIMP models (such as those in [18] [19] and [20]) were fit to the data, accounting for the previously-established constraints upon the WIMP parameter space. The TeV WIMP models put forward in [18] [19] and [20] to explain the excess DAMPE flux all share a significant characteristic - these WIMPs are Leptophilic. The Leptophilic WIMPS interact (via a TeV Z′ mediator boson) exclusively with electrons, muons and tauons, together with their associated neutrino flavours and all respective anti-particle counterparts [2].

Given that the decade prior featured the successive failures of both collider and direct detection experiments to detect a WIMP signal, the parameter space was quickly shrinking for WIMPs with Hadronic interactions [2]. Therefore, it is unsurprising that the models feature Leptophilic WIMPs, since both PANDAX-II [17] and LUX [15] had already announced the non-detection of a WIMP signal by their respective Direct detection experiments at the time when the DAMPE excess flux was detected in 2017 [21].

The 2021 Indirect radio search in the LMC extended this analysis to empirically rule out all WIMPs hypotheses with quark interactions [35]. Therefore, if WIMPs are truly the constituent particles of Dark Matter, then they can have no interactions with quarks. The Leptophilic WIMP models proposed in the wake of the DAMPE excess flux were initially introduced to relax the stringent constraints upon the parameter space of WIMPs with Hadronic interactions - constraints that were imposed by consecutive failures to detect a DM signal by Collider and Direct detection experiments. Given the result in [35], WIMPs are now necessarily Leptophilic, as presumed by the authors of the TeV WIMP models that were proposed to explain the detection of the anomalous e^-/e^+ excess flux detected by DAMPE in 2017.

Among the many instances of WIMP non-detection since the turn of the century is a single, controversial positive result from the DAMA/LIBRA experiment in 2008, claiming to have detected a seasonal variation consistent with the movement of the solar system through the distribution of (non-relativistic, CDM) WIMPs in the Milky Way Halo [36]. More than a decade later, the ANAIS direct detection experiment performed a model-independent test of the DAMA/LIBRA positive result, utilising the same NaI target medium and Photo-Multiplier Tube detection mechanism [37]. Having taken measurements in the same energy range as the DAMA/LIBRA experiment, the ANAIS experiment announced in 2021 a failure to detect the seasonal modulation reported by DAMA/LIBRA [36], with the results found to be inconsistent at a statistical significance of at least 2.6σ [37]. Therefore, the single positive DAMA/LIBRA result in [36] has been proven by the ANAIS experiment [37], with a high probability, to be a false positive. This is consistent with the failure of every other direct detection experiment, indirect detection experiment and collider search to detect DM and corroborate the anomalous DAMA/LIBRA result.

The key events and experimental tests in Figure 1 will feature throughout this work to further elaborate upon the contemporary state of the WIMP hypothesis and to motivate the discovery potential of upcoming telescopes like CTA, KM3NeT and MeerKAT to probe the nature of DM and empirically interrogate the WIMP hypothesis through Multi-messenger indirect DM searches. [1]

[1] Appendix F contains a table cross-referencing the references in the timeline with citations in this work's bibliography.

A Historical Overview of the Dark Matter Mystery

1933 — **Zwicky**: Calculates that in order to gravitationally bind the **Coma Cluster**, the actual mass had to be ~ 100 times greater than the observed mass in stars and so postulates an unseen **Dark Halo** engulfing the cluster *(a)*

1965
- **Penzias and Wilson**: Published on the detection of the **Cosmic Microwave Background** (CMB) radiation *(b)*
- **Peebles, Dicke, Roll and Wilkinson:** Concurrently published interpretations of the observed CMB which situates it within the predictions of a **Hot Big Bang** *(c)*

1970 — **Rubin and Ford**: Spectroscopic survey of **Andromeda** produced **anomalous rotation curves**, with rotational velocity remaining constant at large distances from the galactic centre *(d)*

1973
- **Ostriker and Peebles**: **N-Body Simulations** demonstrate that **disk galaxies** cannot be rotationally supported and thus another, **massive spheroidal component** of the galaxies must exist *(e)*
- **Roberts (NRAO) and Rots (WSRT):** Discovery of **three galaxies** with **rotation curves** that suggested the presence of a **Dark Halo** with undetected mass at large distances away from the galactic centre *(f)*

1977
- **Hut** *(g)* and **Lee & Weinberg** *(h)*: Independently introduced heavy, neutral particles which interact on the scale of the Weak Force - **Weakly Interacting Massive Particles (WIMPs),** a **candidate for particle DM**
- **Peccei and Quinn:** Theoretically account for **CP Conservation** in for **Strong force interactions** *(i)* and then **Weak and EM interactions** *(j)* through introduction of **a pseudo-scalar field** permeating all space. In **1978**, the quanta of the Peccei-Quinn field were studied independently by **Wilczek** *(k)* and **Weinberg** *(l)*, who termed them **Axions,** another **candidate for particle DM.**

1983 — **Milgrom**: Publishes 3 papers proposing a hypothetical model of **Modified Newtonian Dynamics (MOND)** *(m)* which would **eliminate the need for non-Baryonic DM** and then calculates its consequences for **galaxies** *(n)* and **galaxy systems** *(o)*

1994 — **Dodelson and Widrow**: Establish **Sterile, Heavy Neutrinos** as **particle DM candidates** by extending the model into the Cold Dark Matter paradigm and accounting for structure formation *(p)(q)*

2006 — **LEP Collider search:** No evidence found for physics beyond the Standard Model**,** constraining possible mass of the hypothetical **Z' gauge boson in WIMP models** *(r)*

2008 — **DAMA/LIBRA Direct detection experiment:** Announces a controversial **detection of a hypothesised annual modulation** in the observed detection rate, consistent with the presence of **DM particles in the Milky Way Halo** *(s)*

2012 — **CMS Detector at the LHC:** No signal consistent with the existence of **Z' boson**, with results taken at $\sqrt{s}$ **= 7 TeV** *(t)*

2014 — **ATLAS Detector at the LHC:** No signal consistent with physics beyond the standard model at $\sqrt{s}$ **= 7 TeV** and **8 TeV**, confirming CMS result in *(t)* and strengthening constraints upon the **Z' mediator boson** parameter space *(u)*

2015 — **Planck Satellite:** No evidence found for the existence of WIMP Dark Matter in observed **CMB anisotropies** *(v)*

2016 — **PANDAX-II Direct detection experiment:** No evidence found for existence of **WIMP DM** in first **98.7 days of data**, imposing stringent non-detection upper bounds on the **WIMP scattering cross-section in the 5 GeV – 1 TeV** mass/energy range *(w)*

2017
- **ATCA Indirect Radio search:** Non-detection of synchrotron emission from **WIMP Annihilation or Decay** by observations of **Reticulum II** *(x)*
- **LUX Direct detection experiment:** No evidence for **WIMP-Nucleon scattering** *(y)* and **Leptophilic WIMP models** subsequently introduced to relax heavy non-detection constraints upon WIMPs with Hadronic interactions *(z)*
- **Dark Matter Particle Explorer:** Detects **excess electron-positron flux at ~ 1.4 TeV** *(aa)*, with several **TeV Leptophilic WIMP** models proposed to explain the excess flux *(ab)(ac)(ad)*

2018 — **XENON1T Direct detection experiment**: Failure to detect significant **WIMP-Nucleon scattering** events, imposing the most stringent Direct detection constraints to date upon the WIMP parameter space *(ae)*

2019 — **Fermi Indirect Gamma Ray Search:** Severe non-detection constraints placed upon **Decay channel** by observational data of the **Isotropic Gamma Ray Background** radiation *(af)*

2020 — **Super-Kamiokande Indirect Neutrino Search:** Non-detection of WIMP signal in **20 years of observational data** of the **MW Halo and Centre** *(ag)*

2021
- **ANAIS Direct detection experiment:** Performed **model-independent test of the DAMA/LIBRA result** in *(s)* and failed to detect the modulation reported by DAMA, demonstrating with **high probability that the anomalous result was a false positive** *(ah)*
- **ASKAP/EMU Indirect Radio search:** Observations of the **Large Magellanic Cloud** places strong non-detection constraints on the Annihilation cross-section, ruling out WIMP masses below 480 GeV and Annihilation to quarks *(ai)*

Figure 1: *A timeline detailing the history of the Dark Matter mystery, beginning with Zwicky's studies of the Coma Cluster in 1933 [1] and following the trajectory of the WIMP hypothesis from its inception ([10] [11]) through to consecutive failures to detect a signal indicating the existence of WIMPs by Collider experiments ([12], [13], [14]), Direct detection experiments ([15], [37], [16] and Indirect Dark Matter searches ([23], [25], [24]) being conducted in the 21st century*

2. Collider Experiments and Dark Matter Direct Detection

In 2006, four collaborations at the Large Electron-Positron (LEP) collider published preliminary Electroweak Measurements , in additional to preliminary Standard Model constraints, following the summer conferences at which the results of the LEP experiments were presented [12]. They find no significant experimental evidence for the existence of the Z′ boson in the data and thus derive lower limits on the mass of the hypothetical Z′ boson, $m_{Z'}$ [12]. The LEP collider search will be discussed in further detail in the context of the constraints explicitly considered in the context of this work.

In 2012, the CMS experiment at CERN's Large Hadron Collider (LHC) announced the first non-observation of the Standard Model Z boson decaying to four leptons [13].

In 2014, CERN's ATLAS experiment published their own measurements of the four-lepton production cross section, in proton-proton collisions at the Z resonance in the LHC, operating at $\sqrt{s} = 7\,TeV\,and\,8\,TeV$ [14].

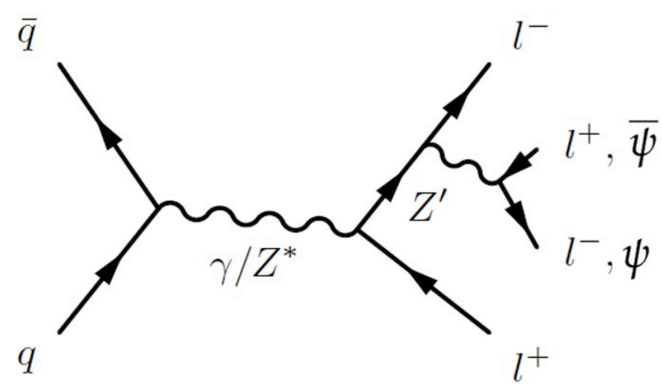

Figure 2: *Feynman diagram of production of a Z′ boson, radiated from a Lepton in the Drell-Yann process inside a Hadron collider, with the Z′ subsequently decaying to Leptons or WIMPs, ψ (adapted from [2])*

Given the failure of Collider experiments at LEP [12] and the LHC [13] [14] to provide any empirical evidence for the existence of WIMPs, Dark Matter Direct detection experiments offer an alternative, seeking to measure the recoil energy of SM nuclei, which would hypothetically arise through local scattering of the nuclei inside the detector by DM particles [2]. DM Direct detection therefore hinges upon DM-Nucleon interactions occurring within the detector medium and non-detection strongly constrains WIMP models with DM couplings to Hadrons.

In 2016, the PandaX-II Direct detection experiment, housed at the China JinPing underground Laboratory (CJPL), announced the results from its first 98.7 days of collecting data[17]. Utilising a dual-phase liquid Xenon Time Projection Chamber (TPC), it allows for the reconstruction of both the energy and position of an event [17]. With a total exposure of 33 tonnes $\times$ day, the PandaX-II experiment imposes competitive, stringent upper bounds on the scattering cross section for WIMP masses in the range of 5 GeV - 1 TeV, at a Confidence Level of 90% [17].

In March of 2017, in the proceedings of the 52nd *Rencontres de Moriond* conference in March 2017 on Very High Energy Phenomena in the Universe, the Large Underground Xenon (LUX) collaboration reported the results of a WIMP DM Direct detection search in data gathered by the LUX experiment [38]. The LUX Direct detection experiment is housed at the Davis Campus of the Sanford Underground Research Facility [38]. In the publication of the LUX results, the collaboration reports no WIMP signal above background, leading to stringent constraints being placed upon the spin-independent scattering cross-section [15]. Prior to the conference, the LUX collaboration published these results in the Physical Review Letters journal, elaborating upon the methodology employed in the Direct DM search [15]. As one of the Direct detection constraints explicitly considered in this work, the LUX upper bounds on Hadronic DM and its implications for the WIMP hypothesis will be discussed in further detail in a later chapter.

In 2018, the XENON collaboration published the results of a WIMP Direct detection experiment using the XENON1T detector, which utilises liquid Xenon with a fiducial mass of (1300 ± 10) kg to search for DM-Nucleon scattering events between the WIMPs and the Xenon nuclei [16]. Since Xenon is a scintillator, the scattering events will result in fluorescence in the visible spectrum, which would then be detected by Photo-Multiplier Tubes (PMTs) inside the detector[34]. DM-nuclei scattering will also result in ionization. Hence, this inert element is also used as the detector medium in both the PandaX-II and LUX experiments.

Observations were performed for a total exposure time of 278.78 days, with the background rate being minimised more than any prior DM search experiment [16]. Despite the reduced background rate and the low error margins, no significant excess was detected and thus non-detection constraints are placed upon the spin-independent cross-section for (elastic) DM-Nucleon scattering σ_{SI} [16], as shown in Figure 3.

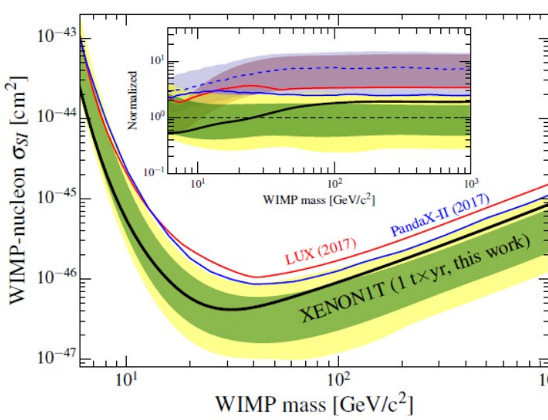

Figure 3: *Upper limits on the spin-independent WIMP-nucleon scattering cross section imposed by the failure of the XENON1T experiment to detect WIMPS [16], compared to the non-detection upper-limits imposed by the LUX experiment [15] and the PandaX-II experiment [17].*

Among the many instances of non-detection is the anomalous positive result announced by the DAMA/LIBRA direct detection experiment in 2008, reporting the observation of an annual variation in the detection rate, which is consistent with the predictions for DM particles in a typical galactic DM Halo [36]. Located in Italy, the subterranean DAMA/LIBRA detector comprised NaI(Tl) crystal scintillators (which are highly radiopure) connected to Photo-Multiplier Tubes (PMTs), with a total detector mass of approximately 250 kg [36]. DAMA/LIBRA's reported detection of the predicted model-independent annual modulation is reported at an exposure of 530 kg $\times$ yr, over four annual cycles [36]. By combining the data with the results of its earlier DAMA/NaI experiment, DAMA reported the detection of DM particles in the MW galactic Halo at a Confidence Level of 8.2 σ [36].

In 2021, the ANAIS (Annual Modulation with NaI Scintillators) Collaboration in Spain published the results of a three year long DM Direct detection search [37], with the aim of a model-independent test of the DAMA/LIBRA result in [36]. This followed more than a decade of increasingly sensitive experiments failing to corroborate DAMA/LIBRA's positive result [37]. Like the DAMA/LIBRA experiment, the subterranean ANAIS experiment utilises NaI(Tl) as the target medium, with a total detector mass of 112.5 kg in the case of ANAIS, which performed the experiment in the same energy regions, allowing for more direct comparisons to be made between the results [37].

At an effective exposure of 313.95 kg $\times$ yr, the ANAIS experiment measured modulation amplitudes which indicate the absence of any annual modulation in their data and thus their results are shown to be incompatible with the DAMA/LIBRA results at a statistical significance of at least 2.6 σ [37]. The ANAIS collaboration thereafter proceeds to devise and implement consistency checks for the methods employed in their analysis, demonstrating that their result is unbiased [37]. Even after accounting for the systematic effects, the ANAIS result remains consistent with an absence of annual modulation, with the collaboration aiming to increase the statistical significance of the result to 3 σ within its scheduled five years of operation [37].

Thus, the ANAIS result in [37] demonstrates an exceedingly high probability that the single anomalous DAMA/LIBRA positive result in [36] is due to that experiment's systematics and not due to interactions between DM particles and the target medium in the DAMA/LIBRA detector. Given this, it is evident that, like the Collider experiments, all Dark Matter Direct detection experiments to date have failed to detect a DM signal.

3. Dark Matter Indirect Detection

Dark Matter Indirect detection experiments seek to detect DM particles through detection of the secondary particles produced by their Annihilation or Decay [39]. It must account for the interplay between the "macrophysics" of the DM Halo and the "microphysics" that governs the particle interactions of a DM candidate [22].

This is done through scanning the astrophysical sky for unexplained fluxes that may be accounted for by DM annihilation or decay [2]. Hypotheses are subsequently put forward to explain the flux, fit to the data and a DM candidate particle is posited with properties that can be independently tested in the context of new observational targets. The candidate particle must also be consistent with prior constraints placed upon the parameter space for the particle DM model, which is the WIMP hypothesis in our case.

Given the failure of Direct detection and Collider experiments to shed light on the properties of DM, Indirect detection provides us with an exciting and promising alternate avenue to probe the nature of DM. Nascent astrophysical experiments like the CTA, KM3NeT and SKA (including MeerKAT) have unprecedented sensitivities, providing a new generation of telescopes for DM Indirect detection.

i Indirect Searches Conducted Thus Far

In 2017, Regis, Richter and Colafrancesco presented a deep radio search, conducted by the Australia Telescope Compact Array (ATCA), in the Reticulum II dwarf spheroidal galaxy [23]. The search found no evidence for a diffuse radio emission due to synchrotron emission from DM annihilation or decay [23]. They therefore place novel constraints/bounds upon the WIMP parameter space [23].

In 2019, Blanco et. al. published an indirect gamma ray search utilising Fermi observations of the Isotropic Gamma Ray Background. Stringent non-detection upper limits are placed upon the Decay rate, further establishing the relative stability of WIMPs. [25]. The Isotropic GRB search constraints in [25] are considered explicitly as a point of reference in this work and will be discussed in further detail in a later chapter.

In 2020, the Super-Kamiokande collaboration presented a search for excess neutrino interactions due to WIMP self-annihilation in the galactic centre or halo [24]. The reported non-detection by the neutrino search further tightens constraints on $\langle \sigma v \rangle_\psi$ over a range of channels for WIMPs in the 1 GeV to 10 TeV range [24]. These Annihilation constraints will be considered as a point of comparison for the calculated non-detection constraints in this work and will be discussed in further detail in the following chapter.

In 2021, an indirect radio search in the Large Magellanic Cloud (LMC), processing a deep image taken by ATCA as part of the Evolutionary Map of the Universe (EMU) survey, found no signal consistent with WIMP Annihilation [35]. This allows them to completely eliminate WIMPs which Annihilate to quarks and rules out all WIMPs with masses smaller than 480 GeV [35].

Several groups have recently reported an excess flux (over the expected background) in the anti-proton data from the AMS-02 detector aboard the International Space Station [40]. This excess flux is argued to be consistent with some DM annihilation signal, with the excess producing a common picture of DM properties from different DM models [40]. However, the significance of the excess is hotly debated [40] and so will not be taken into consideration for the purposes of this work.

The indirect search that is the primary focus of this work involves the detection of an excess electron/positron flux by the Dark Matter Particle Explorer (DAMPE) in late 2017 [21]. Several Leptophilic Weakly Interacting Massive Particle (WIMP) hypotheses were formulated to explain the excess, such as those contained in [18],[19], [20] and [41].

4. The Wukong WIMPs: Massive Leptophilic Majorana Particles

In late 2017, Wukong, the DArk Matter Particle Explorer (DAMPE), directly measured Cosmic Ray Electrons (plus Positrons) (CREs) in the energy range of 25 GeV - 4.6 TeV, in a setting with a low background signal and with unprecedented resolution [21]. As announced by the DAMPE collaboration, Wukong had detected an excess e^- / e^+ flux at approximately 1.4 TeV, as illustrated in Figure 4 [21].

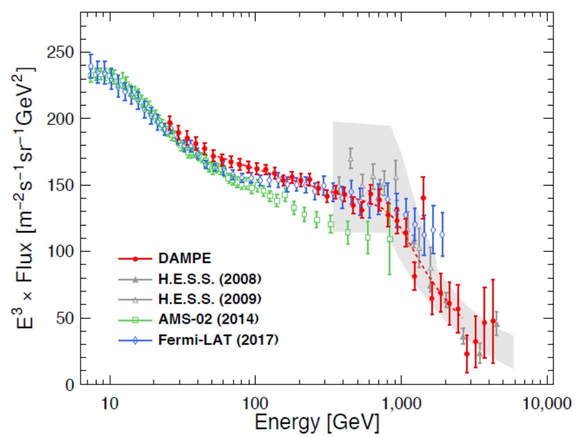

Figure 4: *The CRE flux spectrum (multiplied by E^3) measured by Wukong, with a clear spectral break at approximately 1.4 TeV [21].*

In Figure 4, a smoothly broken power-law model is used to fit the DAMPE data in the range of 55 GeV - 2.63 TeV, producing the dashed red line [21]. The excess flux is apparent when the DAMPE fit is compared with the measured data, represented by the red dots, with the error bars of $\pm 1\sigma$ account for systematic and statistical uncertainties [21].This measured flux spectrum in Figure 4 is contrasted by direct CRE measurements by AMS-02 and Fermi-LAT, along with indirect measurements made by H.E.S.S [21].

A number of Weakly Interacting Massive Particle (WIMP) models, as detailed in [18], [19], [41] and [20], were posited to explain the unexplained DAMPE flux. These Leptophilic WIMPs, ψ , are theoretically defined in [2]. The models put forward following the detection of the excess Wukong flux are detailed in Table 1. All masses are quoted in TeV.

Authors	m_ψ	$m_{Z'}$	**Particle Type**	**Annihilation/Decay Channels**	**Reference**
Fan, Huang et. al.	1.5	2.6	Vector-like fermion	e^-/e^+ and μ^-/μ^+	[20]
Yuan, Feng et. al.	1.5	$> m_\psi$	Dirac or Majorana fermion	e^-/e^+ or $e\mu\tau$	[18]
Yang and Su	1.4	$> m_\psi$	Dirac or Majorana fermion	e^-/e^+	[19]

Table 1: *Leptophilic WIMP models posited to explain the excess Wukong flux, as detailed in [18], [19] and [20].*

In Table 1, Z′ is a boson which mediates the interaction of the WIMPs with SM leptons, while $e\mu\tau$ refers to the $3l$ democratic case, with equal pairing to each lepton channel.

In this work, we adopt a model independent approach, considering WIMPs ψ that possesses the following common features of the models above:

- They are Leptophilic, that is, they interact, at tree level, exclusively with Standard Model leptons (electrons, muons and tauons, along with their associated neutrinos) - and their associated anti-particles [2].
- They couple to the leptons via a heavy bosonic mediator particle Z′.
- Their masses are on the TeV scale, as are the masses of Z′, with $m_{Z'} > m_\psi$.
- They are spin-half Fermions.
- They are Majorana particles, identical to their anti-particles and thus self-Annihilating

We thus term these particular WIMPs *Massive Leptophilic Majorana Particles* (MLMPs) which interact on the scale of the Weak force. The Feynman diagram for MLMP self-annihilation into SM Leptons is presented in Figure 5.

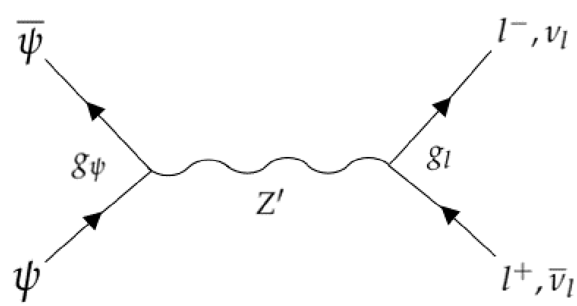

Figure 5: *Feynman diagram for MLMP Annihilation (adapted from [2])*

This work aims to test and constrain this generalised MLMP model, calculating projected non-detection bounds in the 1 TeV to 2 TeV range utilising multi-messenger observations of prime target objects by a number of next-generation telescopes.

5. Established Constraints on the Annihilation Cross-Section

We consider the constraints accounted for in [20] - the 2015 Planck CMB constraints [7], the DM Relic Density bound [42], the LEP Z′ constraints [12] and the LUX Direct detection constraints [15] fit to the DAMPE flux as in [20]. We also consider the constraints imposed by the Indirect radio search in Reticulum II using the Australia Telescope Compact Array [23], the constraints imposed by the Super-Kamiokande Indirect neutrino search in the MW Halo and Centre [24] and the constraints imposed by the ASKAP/EMU radio search in the LMC [35].

i The Relic Density Constraints

In 1977, astrophysicist Piet Hut [10] on one hand and Lee and Weinberg on the other [11] independently derived cosmological lower bounds between 1 and 5 GeV on the masses of heavy leptons which are neutral and interact weakly - in two senses, describing both the relative strength of the DM particle interactions, which are extremely low, along with the fact that the particle interactions occur on the scale of the Weak Force. Although neither of the authors of [10] nor [11] intended to put forward a hypothetical non-Baryonic particle model to account for the mounting evidence of the existence of DM, their work nonetheless heralded the birth of the Weakly Interacting Massive Particle (WIMP) Dark Matter hypothesis considered in this work, along with dawn of the field of Astro-Particle Physics [8].

The 'canonical' thermal cross-section (usually quoted as $\langle \sigma v \rangle_\psi \approx 3 \times 10^{-26}\text{cm}^3\text{s}^{-1}$) is the WIMP Annihilation cross-section required to account for the observed relic DM abundance, within the framework of Big Bang Cosmology, assuming s-wave Annihilation [42] [7]. The authors of [42] calculate the precise value of the thermal relic cross section as $\langle \sigma v \rangle_\psi = 2.2 \times 10^{-26}\text{cm}^3\text{s}^{-1}$ for WIMP masses above 10 GeV. Since we are working in this mass-energy range, we can thus state the relation between the canonical cross section and the DM relic density mathematically, following the form in [43]:

$$\Omega_\psi h^2 = \frac{2.2 \times 10^{-26}\text{cm}^3\text{s}^{-1}}{\langle \sigma v \rangle_\psi} \tag{1}$$

where Ω_ψ is the observed cosmological DM density parameter and h is the reduced Hubble constant.

ii The Planck CMB constraints

In 1965, Penzias and Wilson reported the detection of an excess antenna temperature at 3.5 K, utilizing the 20-foot horn-reflector at the Crawford Hill Laboratory [5]. The radio signal was reported to be isotropic, free from seasonal variations and unpolarized [5].

Concurrently, in the same volume of the Astrophysical Journal, Peebles, Dicke, Roll and Wilkinson published a paper putting forward a possible explanation for the radio signal which situates it within Big Bang Cosmology [6].

In 2015, the Planck collaboration published updated Cosmological Parameters derived from observations of the CMB with the space-based telescope [7]. The updated results helped to further reconcile the empirically calculated parameters, which characterise the features of our universe as a totality, with respect to the theoretical predictions for these parameters from the standard

ΛCDM Cosmological model [7].

During the early history of the universe, the injection of energy from Annihilating DM particles would have altered the event of recombination in a substantial manner, leaving a detectable imprint upon the CMB in the form of anistropies in the temperature, power and polarisation spectra of the CMB [7]. During this era of recombination, the particle cascades which result from WIMP Annihilation determine the heating and ionization of the surrounding gaseous medium [7].

Of particular interest are the e^{-}/e^{+} pairs, along with photons, produced through Annihilation, since they can couple to the ambient gaseous background [7]. To address this, the proportion of the rest mass/energy which is transferred to the gaseous medium is modelled by a dimensionless, redshift-dependent *efficiency factor*, $f(z)$, ranging between 0.01 and 1 [7]. They parameterise the effects of DM Annihilation by defining an Annihilation parameter, dependent on the redshift parameter and explicitly dependent on both the the WIMP mass and Annihilation cross-section [7]:

$$p_{\text{ann}}\left(z, m_{\psi}, \langle\sigma v\rangle_{\psi}\right) = f(z)\,\frac{\langle\sigma v\rangle_{\psi}}{m_{\psi}} \tag{2}$$

They set the efficiency factor to a constant f_{eff}, where every Annihilation channel has a corresponding efficiency factor [7]. Thus, the Annihilation parameter contains information on every parameter relevant to the Annihilating WIMP, allowing for the projection of the constraints upon p_{ann} for a particular WIMP model [7], where one can simply solve Equation 2 for $\langle\sigma v\rangle_{\psi}$, a specified Annihilation channel and mass range. Since the effect of DM Annihilation peaks at $z \approx 600$, they utilise this value of the cosmological redshift [7]. Given the proportionality of the Cosmological mass density, ρ_m, to $(1+z)^3$, this corresponds to an epoch where the mass density of the universe was more than 8 orders of magnitude greater than its current value.

Through constraining the Annihilation parameter, they find that the Planck TT spectra alone imposes the weakest constraints (which are upper limits at a 95% confidence level), due to the fact that WIMP Annihilation would act to increase the width of last scattering, thereby suppressing amplitude peaks in the temperature spectrum[7]. The strongest constraints are imposed in the case of the full Planck temperature and polarization likelihood (TT, TE, EE + lowP) [7] and the projection of these constraints upon particular DM models produces the plot in Figure 6.

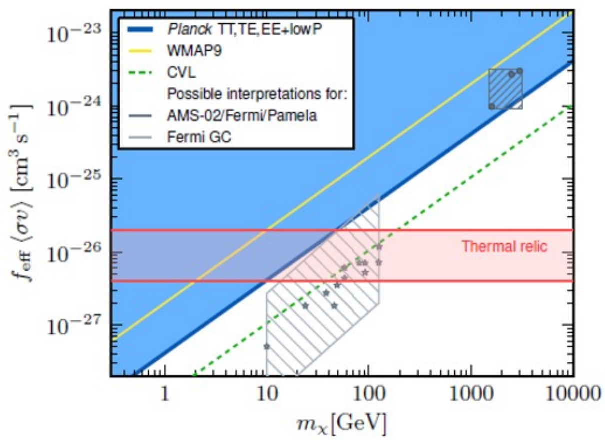

Figure 6: *Constraints (at a 95 % Confidence Level) imposed upon $\langle\sigma v\rangle_\psi$ at recombination (multiplied by the relevant efficiency factor), resulting from non-detection of a WIMP signal in the CMB anisotropies measured by Planck in 2015 [7].*

In Figure 6, the constant efficiency factors used for the respective leptonic Annihilation channels are taken from the results of a 2009 paper which calculates the constraints imposed upon WIMP Annihilation by observations of the CMB [44]. The results for the efficiency factor at a particular WIMP mass (also referred to as the "deposited power fraction") as a function of the redshift z is given in figure 4 of [44], where we focus only on the plots in the bottom two panels, since they concern WIMPs that couple to leptons via a bosonic mediator, as do the generalised Leptophilic WIMPs under consideration in this work. The efficiency factors for the leptonic channels are [44]:

- e^-/e^+ channel: $f_{eff} \approx 0.60$
- μ^-/μ^+ channel: $f_{eff} \approx 0.20$
- τ^-/τ^+ channel: $f_{eff} \approx 0.15$

Thus, the Thermal Relic cross-section bound appears as a red band and not a single line, with the upper red line being consistent with 10 GeV WIMPs Annihilating into e^-/e^+ pairs, where $f^e_{eff} = 0.67$ [7]. The shaded blue area in the upper left of the plot in Figure 6 denotes the parameter space empirically ruled out by non-detection of a WIMP DM signal in the CMB Anisotropies [7]. Therefore, at a Confidence Level of 95 %, the Planck non-detection results eliminate WIMP models with $m_\psi \leq 44 GeV$ for Annihilation via the e^-/e^+ channel [7]. This is evident from the intersection between the upper red line, for the e^-/e^+ channel Thermal Relic limit, and the dark blue line on the border of the shaded area denoting the parameter space excluded by Planck, since $\langle\sigma v\rangle_\psi$ for WIMPs at lower masses than 44 GeV produce cross section bounds which cannot account for the relic density of Dark Matter.

Similarly, using the efficiency factors quoted above, WIMPs with $m_\psi \leq 16\,$GeV are excluded for the μ^-/μ^+ Annihilation channel and WIMPs with $m_\psi \leq 11\,$GeV are excluded for the τ^-/τ^+ Annihilation channel [7]. Therefore, for the purposes of the Leptohilic WIMP hypothesis under consideration, we know that our hypothetical WIMPs must be on the order 10 GeV or greater.

iii The LEP Collider Constraints on Z', the Mediator Particle

The authors of [12] fit the LEP experimental data to models involving a additional neutral, heavy boson Z', utilising both the Leptonic forward-backward asymmetries and the combined cross-sections in the hadronic and leptonic cases, as presented in Figure 7.

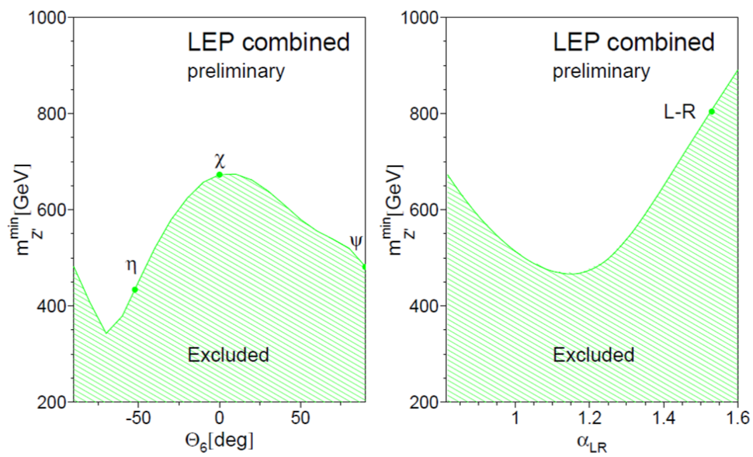

Figure 7: *Lower limits imposed upon $m_{Z'}$ by the LEP fit, at a confidence level of 95% [12]*

In deriving the constraints, they set the mixing angle between the ordinary Z boson and Z′ as $\Theta_{ZZ'} = 0$, based on the results of a single experiment, fit to LEP-I data [12]. In the left panel of Figure 7, the ν , χ and ψ variables denote particular Grand Unified Theory models featuring the additional Z′ boson, as further laid out in [12]. The right panel displays the constraints imposed in the case of Left-Right models, with the mass of Z′ plotted as a function of the dimensionless model parameter, α_{LR} [12]. As can be seen in both panels of Figure 7, across the respective domains of all models concerned, $m_{Z'}$ must exceed 300 GeV at the very least. Thus, the TeV WIMP models considered in this work, with $m_{Z'} > m_\psi$, are consistent with the calculated LEP lower bounds on the mass of the Z′ mediator particle [45].

iv The Dark Matter Direct Detection Constraints

In the parameter space derived from the Wukong fit in [20] and presented in Figure 12, the only DM Direct detection constraints considered are those imposed as a consequence of the reported non-detection by LUX in 2017 [15][38], which are more stringent than those imposed by by the prior PandaX-II experiment. Like the PandaX-II detector detailed in [17], LUX utilises a dual-phase Xenon TPC, with the active detector volume containing 250 kg of ulltrapure liquid Xenon [15]. In order to reduce background noise, the LUX detector is located around one kilometer beneath the surface of the earth [15]. With a total of exposure of 33.5 tonnes $\times$ day [15], LUX gathered data from 2012, when the Davis Campus was opened, to 2016, when the experiment was decommissioned [38].

At a 90% confidence level, the LUX non-detection results impose strong upper limits, on the order of 10^{-46}cm^2 for 50 GeV WIMPs [38]. The upper bounds upon the spin-independent WIMP-Nucleon scattering cross-section, across a mass-energy range which spans more than four orders of magnitude, are presented in Figure 8.

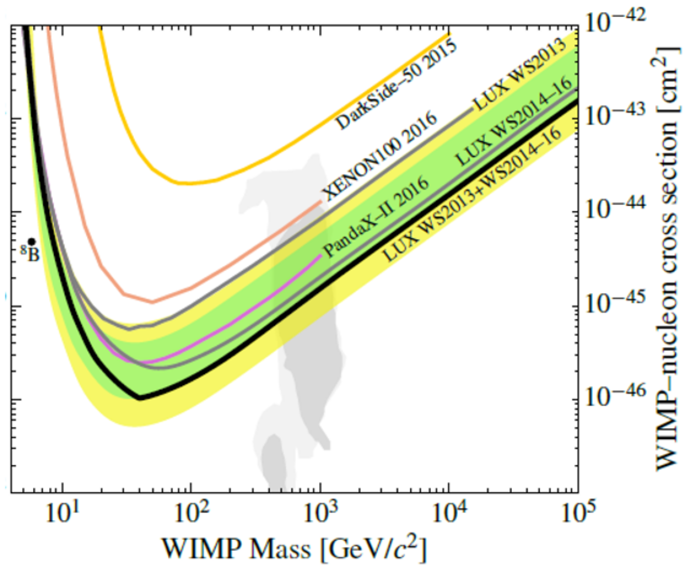

Figure 8: *Non-detection constraints upon the (spin-independent) WIMP-Nucleon scattering cross-section imposed by the LUX experiment across a mass-energy range spanning 5 orders of magnitude, extending up until 100 TeV [15], in comparison to weaker bounds imposed by earlier Direct detection experiments, including the 2016 PandaX-II search [17].*

In August of 2017, a study was published in Physics Letters B on Hadronic probes of hypothetical WIMPs, which couple exclusively to SM leptons via a heavy Z' boson mediator particle [46]. Utilising both the LUX data and projections for the LUX-ZEPLIN experiment, set to replace the now-decommissioned LUX experiment, the authors derive novel constraints upon the Annihilation Cross-section of the Leptophilic WIMPS, which are more relaxed than the constraints placed on Hadronic DM by non-detection by direct detection experiments [46]. This Leptophilic species of WIMP is the subject of study in this work.

It's noteworthy that the lower bounds imposed by non-detection in the case of the Xenon1T experiment [16], as presented in Figure 3, are more stringent than those imposed by both PandaX-II [17] and LUX [15] [38]. However, at the time of the detection of the Wukong flux [21] and the subsequent publication of the Leptophilic WIMP model, fit to the DAMPE flux presented in [20], the Xenon1T non-detection result in [16] had yet to be announced.

6. Existing Multi-messenger Dark Matter Indirect Detection Constraints

i ATCA Indirect Radio Search in Reticulum II

In 2017, Regis et. al. presented an Indirect radio search using ATCA, searching for synchrotron emission resulting from WIMP Annihilation or Decay in the Reticulum II dwarf spheroidal [23]. The deep search in [23] finds no evidence for diffuse radio emission from Reticulum II and thus imposes constraints upon the WIMP parameters, particularly the Annihilation cross section, as presented in Figure 9.

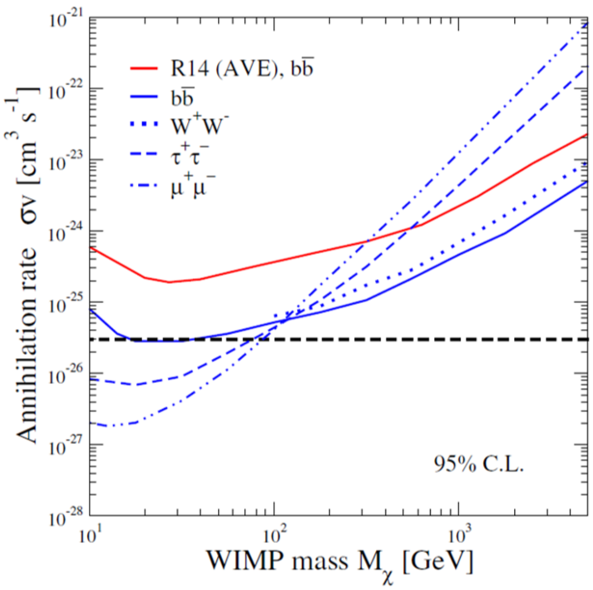

Figure 9: *Non-detection upper bounds imposed upon a number of WIMP Annihilation channels by the ATCA Indirect radio search in Reticulum II, across a mass-energy range from 10 GeV to 10 TeV, with the DM Relic Density limit represented by the dashed black line [23].*

Given that we are dealing with a Leptophilic WIMP model, we consider only the $\langle \sigma v \rangle_\psi$ constraints imposed by the Indirect Search for the μ^+/μ^- Annihilation Channel [23]. The upper limits on $\langle \sigma v \rangle_\psi$ are at a confidence level of 95% [23].

ii Super-Kamiokande Indirect Neutrino Search in MW Halo and Centre

The aforementioned Super-Kamiokande (SK) Indirect neutrino search produced 20 years (1996-2016) of data from Super-Kamiokande-I -II -III and -IV [24]. The SK detector is a 50 kiloton detector, 22.5 kilotons of which comprise the fiducial mass housed within the Inner Detector, relying upon the detection by photo-multipliers of Cherenkov radiation, resulting from charged particles (largely leptons arising from neutrino interactions) moving through the (water) medium faster than light [24].

The observations made of the MW Centre and Halo accounted for any background due to neutrino interactions in the atmosphere [24]. Non-detection of an excess flux places novel constraints upon the Annihilation cross-section [24], presented in the bottom panel of Figure 10.

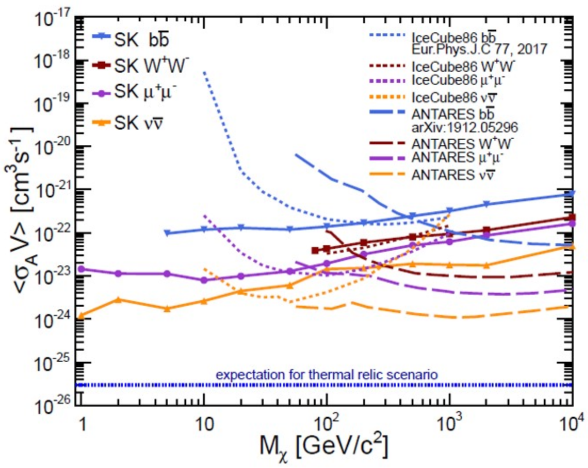

Figure 10: *Non-detection upper bounds imposed upon a range of DM Annihilation channels by the SK Indirect neutrino search, across a mass-energy range from 1 GeV to 10 TeV [24]*

In Figure 10, the non-detection constraints imposed by the SK Indirect search are compared to those imposed by the Antares and IceCube neutrino experiments [24]. As in the case of the Reticulum II radio search, we consider only the μ^+/μ^- Annihilation channel constraints imposed on $\langle \sigma v \rangle_\psi$ by the Indirect neutrino search in [24].

iii ASKAP/EMU Indirect Radio Search in the Large Magellanic Cloud

The 2021 Indirect radio search in [35] utilises a deep image of the LMC obtained from ASKAP observations at 888 MHz (with a bandwidth of 288 MHz) and a total observation time of 12 hours and 40 minutes [35]. Utilising a J-factor of $\sim 10^{20}\,\mathrm{GeV}^2\ \mathrm{cm}^{-5}$ for the LMC, strong non-detection upper bounds are placed on the velocity-averaged Annihilation cross-section, as seen in Figure 11.

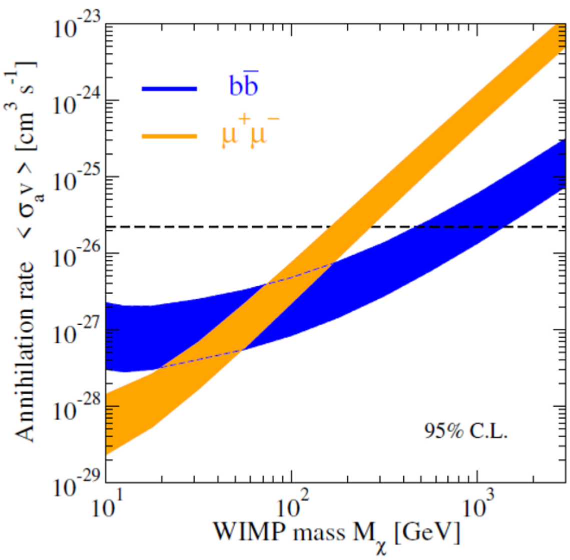

Figure 11: *Non-detection upper bounds imposed upon $\langle \sigma v \rangle_\psi$ by the ASKAP/EMU radio search in the LMC for the $\mu^-\mu^+$ and $b\bar{b}$ Annihilation channels, across a mass-energy range from 10 GeV to 10 TeV, with the DM Relic Density limit shown as the black dashed line [35].*

While the ASKAP/EMU non-detection constraints upon the $b\bar{b}$ Annihilation channel are the most stringent, we are concerned with the constraints imposed upon the $\mu^-\mu^+$, since we dealing with a Leptophilic WIMP model in this work.

iv The DAMPE Excess Flux

When the aforementioned constraints (excluding the Indirect radio and searches in [23] and [35] and the Indirect neutrino search in [24]) are taken into consideration and fit to the DAMPE excess flux at approximately 1.4 TeV reported in [21], the $\langle \sigma v \rangle_{\psi}$ constraint contours in Figure 12 are produced.

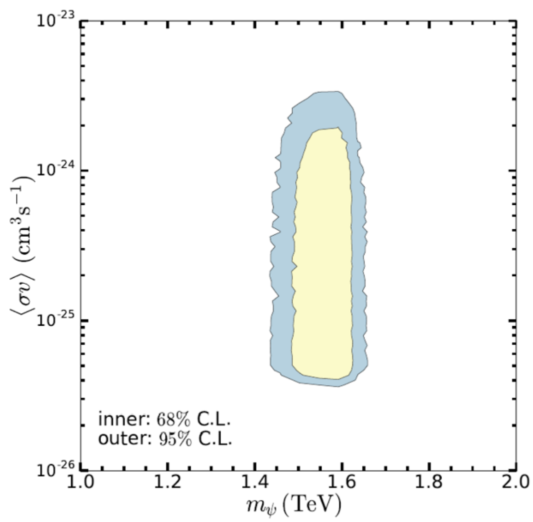

Figure 12: *$\langle \sigma v \rangle_{\psi}$ parameter space presented in [20], produced by fitting the excess e^-/e^+ flux detected by Wukong [21] to:*
i) *The DM Relic Density constraints [42].*
ii) *The 2015 Planck CMB constraints [7].*
iii) *The 2006 LEP Collider constraints on Z' [12].*
iv) *The 2017 LUX Direct detection constraints[15].*

In Figure 12, the inner contour represents the constraints in [20] at a Confidence Level of 68%, while the outer contour represents constraints at a Confidence Level of 95%.

7. Established Constraints upon the Decay Rate

i Isotropic Gamma Ray Background Indirect Search

We account for the constraints placed upon the Decay Rate through utilising the Isotropic Gamma-Ray Background (GRB) observations by Fermi, presented in a 2019 paper published by Blanco and Hooper [25]. When considered alongside the ATCA Reticulum II radio search in [23] and the Milky Way halo neutrino search by Super-Kamiokande in [24], the Fermi Isotropic GRB constraints in [25] offers a multi-messenger benchmark, in the case of both Annihilation and Decay, for DM Indirect detection using existing telescopes.

For a wide range of DM particle masses and annihilation channels, the authors calculate a mean life-time of the decaying DM generally in the range of $\tau_\psi \sim (1-5) \times 10^{28} s$, which is approximately 10-11 orders of magnitude greater than the age of the universe [25]. These constraints are made more stringent by consideration of multi-messenger analyses of the astrophysical contributions to the Isotropic GRB [25]. The immense magnitude of the mean life-time, in relation to the Hubble time, is an illustration of the severe extent to which the Decay channel is constrained.

We focus on DM decay into SM Leptons as in Figure 13, accounting for the fact that the DM Decay Rate, Γ_ψ is simply the inverse of the mean life-time calculated in [25]:

$$\Gamma_\psi - = \frac{1}{\tau_\psi} \tag{3}$$

Hence, the lower limits calculated in [25], as displayed in Figure 13, translate to upper limits upon the Decay Rate, Γ_ψ .

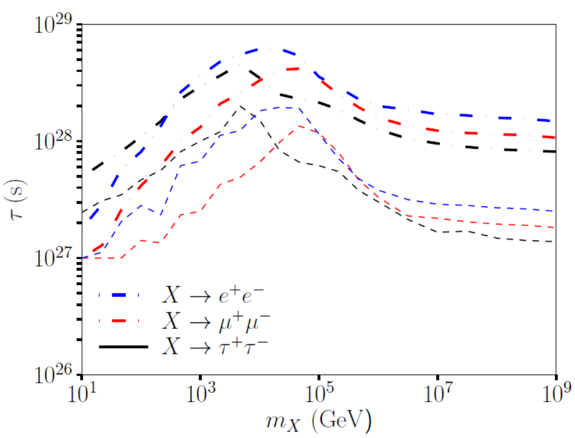

Figure 13: *Lower limits placed upon the DM lifetime, τ_ψ , by observations of the Isotropic GRB by Fermi, for DM Decay across a broad range of masses into SM leptons [25].*

In Figure 13, the solid curves (the upper 3 curves), which treat the systematic errors as entirely independent and uncorrelated, are taken to be the primary results [25]. The constraints are lower limits at a 95% Confidence Level [25].

8. Dwarf Spheroidal Galaxies as Target Objects for DM Indirect Detection

Dwarf spheroidal galaxies, particularly the Ultrafaints, lie at one extreme of the luminosity distribution, at the least luminous and massive end [22]. Alongside galaxy clusters, which lie at the other extreme (most luminous and massive) of the luminosity distribution, dwarf spheroidals are some of the most Dark Matter dominated systems in the Cosmos [22]. These DM-dominated target galaxies have high observed ratios of DM to Baryons, corresponding to high mass-to-luminosity ratios [47].

Dwarf spheroidals also have very old stellar populations (with a typical age of $\sim$ 10 Gyr) and those used as target environments for Indirect detection have virtually no gas associated with them, are relatively close to the Milky Way and have extremely low background in (high energy) photons, due to the absence of observable, Baryonic astrophysical processes [22]. Consequently, the DM Annihilation signals from dwarf spheroidals will be uncontaminated by Baryonic backgrounds in Gamma, Radio and Neutrinos, which make them ideal candidates for a multi-messenger Indirect search for Particle DM [48].

The dwarf spheroidal galaxies in the Local Group considered in this work (including both the Ultrafaint and 'Classical' dwarfs) lie within the virial radius of the Milky Way Galaxy ($\sim$ 300 kpc) and therefore orbit our galaxy as Milky Way satellites [22]. In order to ascertain the DM distributions of these MW Satellites, which are crucial for DM Indirect detection experiments, the kinematics of the luminous stars and gas is studied and analyzed [22]. It is assumed that the identified member stars of a dwarf spheroidal are unaffected by the Milky Way's DM Halo, so that they function as 'tracers' of the dwarf spheroidal's local potential [22]

While the MW Satellites in this work are referred to throughout as dwarf 'spheroidal' galaxies, in actuality the Halos are generally ellipsoids that are not perfectly spherical, which may be problematic when studying the stellar and gas kinematics to determine the respective DM distribution utilising a Jeans method, since these methods operate upon the assumption of spherical symmetry [22]. However, spherically symmetric modeling remains standard practice, since these models tend to provide accurate potential estimates, particularly when dealing with the central regions of the system in the limit of isotropic orbits [22]

Several other systematic issues arise as well when calculating these DM distributions for dwarf spheroidals, including the possibility that the MW Satellites evolve over time as they orbit the Milky Way, along with the prospect of their member stars being stripped away by tidal forces [22]. Moreover, given that the velocity dispersions for dwarf spheroidals are extremely low and so are generally just above the detection threshhold for instruments that measure the velocities of member stars and their (intrinsic) dispersions, another challenge is faced in effectively identifying member stars and conducting a thorough kinematic analysis [22].

Nonetheless, continuing observations of dwarf galaxies, utilising a range of astrophysical techniques, have afforded us better stellar kinematic data sets, so as to refine our physical description of the dwarf spheroidal Halo environments. We can thus reduce our error margins when conducting Indirect DM searches within the Halo of the dwarf galaxy under consideration. In general, the J- (and D-) factors of the more-recently discovered Ultrafaints are larger, but have broader error margins than those of their Classical counterparts, which have been imaged over many decades and are generally more luminous than the Ultrafaints [22].

9. Unprecedented Detection Capabilities of Next-Generation Telescopes

Powerful upcoming telescopes like the Cherenkov Telescope Array (CTA), the Cubic Kilometer Neutrino Telescope (KM3NeT) and MeerKAT boast unprecedented sensitivities in their respective domains and thus allow for a strong multi-messenger astrophysical test of the MLMP models. We compare these sensitivites to the sensitivities of prior telescopes like the Large High Altitude Air Shower Observatory (LHAASO) and compare the constraints imposed by the different telescopes.

i CTA and LHAASO

CTA is an array of ground-based, Imaging Atmospheric Cherenkov Telescope (IACT) which detect Very High Energy (VHE, with $E \geq 200\,\mathrm{GeV}$) gamma rays [49]. It consists of one IACT array in the Canary Islands in the Northern hemisphere and one array in Chile in the Southern hemisphere, with full coverage of the sky [49].

The CTA nodes detect the Cherenkov light from air showers that result from the collision of gamma rays with atmospheric particles [22]. Cherenkov telescopes like CTA are instruments that can integrate for long periods of time on individual observational targets [22]. CTA extends the mass-energy range that can be probed by Indirect searches, encompassing and extending beyond the TeV range considered in this work, with a better angular resolution than the Fermi Large Area Telescope (LAT) [22].

LHAASO is a ground-based cosmic ray and gamma ray telescope located in China [50]. Unlike CTA, which detects the Cherenkov light resulting from the primary atmospheric interaction with the incident gamma rays, LHAASO observes the effects of the secondary cosmic rays that are produced by the primary atmospheric interaction [51]. In estimating the LHAASO sensitivity, the authors of [50] utilise as a point of reference the sensitivity calculated through analysis of Fermi Bubble observations by the High Altitude Water Cherenkov (HAWC) telescope [50], as seen in Figure 14.

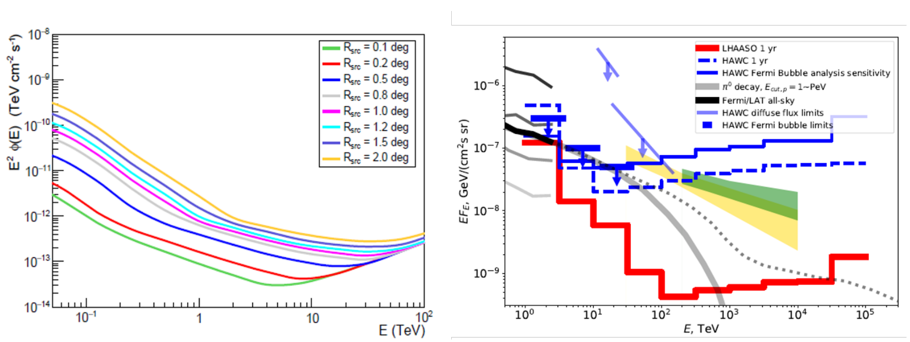

Figure 14: *Left: Sensitivity curves for CTA for a number of opening angles, from the analysis conducted in [49] Right: Sensitivity curve for LHAASO, from the analysis conducted in [50], with one year of exposure time.*

In in the left panel of Figure 14, the conservative sensitivity data for CTA is taken from the analysis in [49], at a minimum confidence level of 5σ and an observation time of 50 hours. We utilize the sensitivity data at an opening angle of 0.5 degrees, in line with the opening angle used in the calculation of the J- (and -D) factors. In comparison to its predecessors (H.E.S.S, MAGIC and VERITAS), CTA has a flux sensitivity that is one order of magnitude larger, with an angular resolution of 1-2 arcminutes [49].

In the right panel of Figure 14, we see that the LHAASO sensitivity is significantly greater than that of the HAWC telescope, across a mass-energy range spanning more than 4 orders of magnitude, with a maximum mass/energy of approximately 10^5 TeV. It is also seen in Figure 14 that the LHAASO sensitivity notably improves with increasing energy, with the minimum sensitivity at the lower end of the mass/energy range, in the TeV region, which is the energy region of focus in this work.

Therefore, the sensitivity improvement over HAWC is minimal in our mass/energy range of 1 TeV - 2 TeV and so we utilise the projected LHAASO non-detection constraints as a benchmark for the projected non-detection constraints imposed by the next-generation telescopes: the aforementioned CTA, along with KM3NeT and MeerKAT. Existing constraints imposed by the Super-Kamiokande indirect neutrino search in the MW Halo and centre [24] and the Indirect radio search in [23] are also used as points of comparison.

ii KM3NeT

Located deep beneath the Mediterranean sea, the upcoming KM3NeT infrastructure, like other high energy neutrino telescopes, functions through the detection of Cherenkov radiation (produced by the interaction of the high energy neutrinos with the surrounding medium, which is primarily sea water in the case of KM3NeT) by a large three-dimensional array of photo-multiplier tubes (PMTs) [49]. The KM3NeT PMTs observe the position, time and charge deposits to infer the direction of the incoming neutrinos, along with their energies [49].

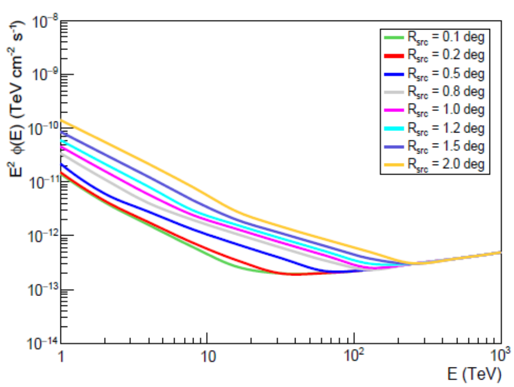

Figure 15: *Sensitivity curves for Km3NeT, from the analysis conducted in [49].*

As was the case with CTA, the conservative sensitivity data for KM3NeT in Figure 15 is taken from the analysis in [49], at a minimum confidence level of 3σ, with an opening angle of 0.5° and a total exposure time of 10 years [49]. The angular resolution of KM3NeT is higher than it is for CTA, with the former reaching an angular resolution of 0.2 degrees at 10 TeV [49].

iii MeerKAT

The MeerKAT radio interferometry telescope infrastructure is the first phase of the Square Kilometer Array (SKA), located in the Karoo desert in South Africa's Northern Cape province [52]. The

MeerKAT array currently consists of 64 radio dishes, operating within the sensitivity range of 580 - 1670 MHz [53]. The existing MeerKAT antennae will be integrated into the future SKA-1 mid telescope infrastructure, which will also be located in the Karoo and will comprise a total of 197 radio dishes [53].

The MeerKAT sensitivity plot in Figure 16 is derived using the MeerKAT Continuum Calculator [2]. By accounting for the beam size, the confusion noise, scaled noise and tapered thermal noise are calculated.

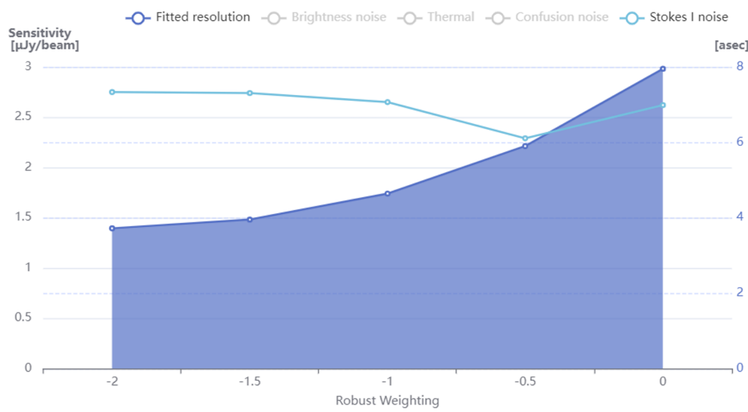

Figure 16: *Sensitivity curves for MeerKAT (in μJy) at observation time of 20 hours respectively, at an opening angle of* $0.5°$

The calculator assumes 58 radio dishes, since this is the minimum requirement for a science array. The calculator requires both the declination of the observational target, which we set to $-30°$, along with the observation time, as input parameters [3]. Following [54] for the L-band sensitivity, we assume a beam size of 19.8″ $\times$ 16.5″, with a total synthesis time of 20 hours.

In a 2020 analysis of the SKA phase 1 sensitivity, projected constraints were calculated for the Draco dwarf, with the SKA 1-MID infrastructure demonstrating great capabilities in constraining the Annihilation parameters of WIMPs, up to mass/energy values of 10 TeV [55].

[2]https://apps.sarao.ac.za/calculators/continuum

[3]https://skaafrica.atlassian.net/wiki/spaces/ESDKB/pages/1486750321/Sensitivity+calculators#Quick-look-tables-of-sensitivities

III. Theoretical Basis for Research

1. Dwarf Spheroidal Galaxy Density Profiles

We consider different density profiles because there exists in the literature an uncertainty considering the structure of dwarf spheroidal galaxies [56]. We consider the three density profiles in [57].

Einasto Density Profile

In 1965, Jaan Einasto put forward a density profile which would explain the kinematic features of the Milky Way galaxy [58]. Equation 4 is a special case of the one originally put forward by Einasto, with the logarithmic density gradient set to 2 in our case [58]:

$$\rho_E(r) = \rho_s \, \exp\left(-\frac{2}{\alpha}\left(\left(\frac{r}{r_s}\right)^{\alpha} - 1\right)\right) \tag{4}$$

where:

- ρ_s is the scale density, normalising the density profile to the virial mass of the Halo, M_{vir}.
- r_s is the scale radius.
- α is the free Einasto parameter.

The Einasto profile is cored, since the mass density converges as the radius tends to 0:

$$As\, r \to 0,\ \rho_E \to \rho_s \, \exp\left(\frac{2}{\alpha}\right) \tag{5}$$

It's noteworthy that for the Einasto profile, with the scale density held constant, the density in the core region increases exponentially as the free Einasto parameter is decreased.

The scale radius, where $\rho_E = \rho_s$ for the Einasto profile, is related to the virial radius by [56]:

$$r_{\text{vir}} = r_s C_{\text{vir}} \tag{6}$$

where C_{vir} is the dimensionless virial concentration parameter. This relation between the scale radius and the virial radius applies to all of the density profiles under consideration in this work.

Burkert Density Profile

In a 1995 paper, Burkert proposes the following Halo mass density profile [59]:

$$\rho_B(r) = \frac{\rho_s}{\left(1 + \frac{r}{r_s}\right)\left(1 + \left(\frac{r}{r_s}\right)^2\right)} \tag{7}$$

The Burkert density profile, like the Einasto profile, is cored and the Burkert density tends the to scale density as the radius tends to 0.

At the scale radius, the Burkert density is simply one quarter of the scale density:

$$\rho_B(r_s) = \frac{\rho_s}{4} \tag{8}$$

NFW Density Profile

A year after the publication of the cored Berkert density profile, Navarro, Frenk and White (NFW) formulated a Halo density model, based on their earlier work with x-ray clusters, which assumed a cuspy density profile [60].

$$\rho_{\mathrm{NFW}}(r) = \frac{\rho_s}{\frac{r}{r_s}\left(1 + \frac{r}{r_s}\right)^2} \tag{9}$$

$\rho_{\mathrm{NFW}}(r)$ does not converge as the radius tends to 0, since as $r \to 0$, $\rho_{\mathrm{NFW}} \to \infty$, illustrating the cuspy nature of the NFW Halo density profile [60]. Like the Burkert density profile given by Equation 7, the NFW density given by Equation 9 is one quarter of the scale density, ρ_s, when the radius is set to the scale radius, $r = r_s$.

Shortly following the publication of the NFW paper, Zhao generalised the density profile analysis as follows [61]:

$$\rho_{\mathrm{NFW}_z}(r) = \frac{\rho_s}{\left(\frac{r}{r_s}\right)^{\beta}\left(1 + \frac{r}{r_s}\right)^{3-\beta}} \tag{10}$$

where β is a dimensionless parameter, related to the (arbitrary) power law density profile of the core region by $\rho(r) \sim r^{-\beta}$ with the outer regions falling off with $\rho(r) \propto r^{-3}$ [62]. We retrieve the original NFW profile in Equation 9 when $\beta = 1$.

DM Halo Mass at the Half-light Radius

The approximate mass at the half-light radius of the Halo is given by Equation 11, as presented in the review in [22].

$$M_h \approx 4\frac{\sigma_{\mathrm{los}}^2 r_h}{G} \tag{11}$$

where:

- σ_{los} is the line-of-sight velocity dispersion
- r_h is the half-light radius
- G is Newton's Gravitational constant

Equation 11 follows from a Jeans analysis, as is utilised in [26] for the calculation of the Astrophysical J- and D-factors discussed in the following chapter, which assumes a spherically symmetric Halo with a velocity dispersion that is constant with respect to the Halo radius [22].

2. The Astrophysical J- and D-factors

There are two metrics which are considered when determining the suitability of a dwarf spheroidal galaxy as a suitable target object for DM Indirect detection: the astrophysical J- and D- factors, corresponding to DM Annihilation and Decay respectively. Both are dependent on the choice of an appropriate DM mass density profile, along with the availability of kinematic data for the member stars of the dwarf spheroidals, which determine the form and accuracy of the density profiles. They are defined as follows:

The astrophysical J-factor is defined as the WIMP mass density squared, integrated over a solid angle $\Delta\Omega = 2\pi[1 - \cos\theta]$, where θ is the opening angle, and along the line of sight l [63]:

$$J = J(\theta) = \iint [\rho_\psi(l, \Omega)]^2 dl \; d\Omega \tag{12}$$

Assuming a spherical DM halo, the integral of the density squared over the solid angle subtended by the halo and along the line of sight is similar to the integral of the density squared over the volume of the halo, distributed over a sphere with radius D_L, where D_L is the luminosity distance between the earth and the Halo under consideration. The J-factor is dependent on the density distribution of the dwarf spheroidal galaxy and is hence a feature intrinsic to the Dark Matter Halo under consideration. We can thus write the J-Factor as:

$$J = \int_{V_{\text{Halo}}} \frac{[\rho_\psi(r)]^2}{4\pi D_L^2} d^3r \tag{13}$$

The astrophysical D-factor, which is empirically determined by kinematic observation of the motion of stars, as in [64], is similar in form to the J-factor and is given by:

$$D = D(\theta) = \iint \rho_\psi(l, \Omega) dl \; d\Omega \tag{14}$$

As with the J-factor, the D-factor is intrinsic to the Halo and can be written as the integral of the DM density over the volume of the halo, distributed over a sphere with radius D_L:

$$D = \int_{V_{\text{Halo}}} \frac{\rho_\psi(r)}{4\pi D_L^2} d^3r \tag{15}$$

The suitability of a given DM Halo as a target in the search for DM self-annihilation is quantified by the Astrophysical J-factor [47], and similarly with regard to DM decay and the Astrophysical D-factor. Both the J- and D- factors account for observational factors (like D_L), as well as features intrinsic to the Halo like the density distribution.

For the purposes of this work, we will take the J- and D-factors at an opening angle of $\theta = 0.5^\circ$.

3. WIMP Velocity-Averaged Annihilation Cross-Section

We suppose that the Dark Matter Halos for the dwarf spheroidal galaxies are comprised of MLMPs. The source function for the annihilation of MLMPs into final state SM particles i with energy E at position r in the Halo is given by a generalisation of the source function in [65], accounting for anti-particles:

$$Q_i(E, r) = \frac{1}{2} \langle \sigma v \rangle_\psi \left(\frac{\rho_\psi(r)}{m_\psi} \right)^2 \sum_l B_l \frac{dN_i^l}{dE} \tag{16}$$

where:

- $\langle \sigma v \rangle_\psi$ is the velocity-averaged cross-section at 0 K.
- B_l is the branching function for the intermediate state, l - which signifies the Annihilation channel.

- $\frac{dN_i^l}{dE}$ is the differential yield of particle species i from WIMP Annihilation via the l channel.
- $\frac{\rho_\psi(r)}{m_\psi}$ is the number density, $N_\psi(r)$, of the MLMP, ψ.

The temperature is set to 0 K due to limits from quantum field theory. Since we are working with velocity-independent parameters, the Annihilation cross-section is p-wave suppressed. When each channel is studied independently, the summation in 16 is dropped and the branching function is set to unity.

The flux of particles i from WIMP Annihilation in the DM halo under consideration is given by:

$$S_i(E) = \int_{V_{\text{Halo}}} \frac{Q_i(E,r)}{4\pi D_L^2} d^3r = \frac{J}{2} \frac{\langle \sigma v \rangle_\psi}{m_\psi^2} \sum_l B_l \frac{dN_i^l}{dE} \tag{17}$$

where we have applied the definition of the Astrophysical J-factor in 13. Re-arranging Equation 17 and equating the flux of particles i to the minimum flux detectable by telescopes on earth yields the following equation for the upper limits on the velocity-averaged Annihilation cross-section of the WIMPs:

$$\langle \sigma v \rangle_\psi = 2 \frac{m_\psi^2}{J} S_i^{\text{min}}(E) \left(\sum_l B_l \frac{dN_i^l}{dE} \right)^{-1} \tag{18}$$

When each channel is considered in isolation, Equation 18 can be equivalently stated in terms of the Annihilation parameter p_{ann}^l in Equation 2, defined by the Planck collaboration in [7].

$$p_{\text{ann}}^l = f_{\text{eff}}^l \frac{m_\psi}{J} S_i^{\text{min}}(E) \left(\frac{dN_i^l}{dE} \right)^{-1} \tag{19}$$

where the dimensionless efficiency factor f_{eff}^l is set to a constant for each leptonic channel l, as further discussed in the prior chapter of this work.

i Derivation of 3l Democratic Annihilation Constraints

We compute the 3l democratic constraints from the constraints from each individual channel by manipulating Equation 18, setting $B_l = \frac{1}{3}$, as follows:

$$\langle \sigma v \rangle_\psi^{3l} = 2 \frac{m_\psi^2}{J} S_i^{\text{min}}(E) \left(\frac{1}{3} \left(\frac{dN_i^e}{dE} + \frac{dN_i^\mu}{dE} + \frac{dN_i^\tau}{dE} \right) \right)^{-1} \tag{20}$$

We now work with the inverse of the equation for $\langle \sigma v \rangle_\psi$ in 20:

$$\frac{1}{\langle \sigma v \rangle_\psi^{3l}} = \frac{J}{6m_\psi^2} \left(\frac{dN_i^e}{dE} + \frac{dN_i^\mu}{dE} + \frac{dN_i^\tau}{dE} \right) S_i^{\text{min}}(E)^{-1} \tag{21}$$

For any single Leptonic channel f treated independently, with $B_f = 1$, the inverse of $\langle \sigma v \rangle_\psi$ is given by:

$$\frac{1}{\langle \sigma v \rangle_\psi^l} = \frac{J}{2m_\psi^2} \frac{dN_i^l}{dE} S_i^{\text{min}}(E)^{-1} \tag{22}$$

Thus, the inverse of the 3l democratic velocity-averaged Annihilation cross-section in Equation 21 can be written as:

$$\frac{1}{\langle\sigma v\rangle_{\psi}^{3l}} = \frac{1}{3}\left(\frac{1}{\langle\sigma v\rangle_{\psi}^{e}} + \frac{1}{\langle\sigma v\rangle_{\psi}^{\mu}} + \frac{1}{\langle\sigma v\rangle_{\psi}^{\tau}}\right) \tag{23}$$

The explicit expression for $\langle\sigma v\rangle_{\psi}$ in the 3l democratic case can be found from simple algebraic manipulation of Equation 23.

4. WIMP Decay Rate

The source function for DM Decay is given in [56]:

$$Q_i(E,r) = \Gamma_{\psi}\frac{\rho_{\psi}(r)}{m_{\psi}}\sum_f B_f \frac{dN_i{}^f}{dE} \tag{24}$$

where [56]:

- Γ_{ψ} is the WIMP decay rate, our free parameter.
- $\frac{dN_i{}^f}{dE}$ is differential yield of particle species i on account of WIMP Decay via the f channel.

As before, the minimum observable flux at energy E is given by:

$$S_i^{\text{mun}}(E) = \int_{V_{Halo}} \frac{Q_i(r,E)}{4\pi D_L^2} d^3r = D\frac{\Gamma_{\psi}}{m_{\psi}}\sum_f B_f \frac{dN_i{}^f}{dE} \tag{25}$$

where we have employed the definition of the astrophysical D-factor in 15. Rearranging Equation 25, we have the upper limit on the WIMP Decay rate:

$$\Gamma_{\psi} = \frac{m_{\psi}}{D}\left(\sum_f B_f \frac{dN_i^f}{dE}\right)^{-1} S_i^{\text{min}}(E) \tag{26}$$

i Derivation of 3l Democratic Decay Rate Constraints

Similarly to the case for $\langle\sigma v\rangle_{\psi}$, we compute the 3l democratic Γ_{ψ} constraints from those provided in Figure 13 by first manipulating Equation 26, setting $B_f = \frac{1}{3}$, as follows:

$$\frac{1}{\Gamma_{\psi}^{3l}} = \frac{1}{3}\frac{D}{m_{\psi}}\left(\frac{dN_i^e}{dE} + \frac{dN_i^{\mu}}{dE} + \frac{dN_i^{\tau}}{dE}\right) S_i^{\text{obs}}(E)^{-1} = \frac{1}{3}\left(\frac{1}{\Gamma_{\psi}^{e}} + \frac{1}{\Gamma_{\psi}^{\mu}} + \frac{1}{\Gamma_{\psi}^{\tau}}\right) \tag{27}$$

This is equivalent to stating that the 3l democratic mean lifetime $\left(\tau_{\psi}^{3l} = \frac{1}{\Gamma_{\psi}^{3l}}\right)$ is simply the average of the mean lifetimes when each Leptonic channel is considered independently.

5. Accounting for Neutrino Oscillations

The analysis of the KM3NeT sensitivity in [49] accounts only for muon neutrinos. However, the phenomenon of neutrino oscillations requires us to account for production of both electron neutrinos and tauon neutrinos.
When we consider the e^-/e^+ Annihilation/Decay channel independently (where $f = e$ and $B_e = 1$) and we require the muon neutrino flux ($i = \nu_{\mu}$), the differential ν_{μ} yield is given by:

$$\frac{dN^e_{\nu_\mu}}{dE} = B_\mu \frac{dN^e_{\nu_\mu}}{dE} + B_e \frac{dN^e_{\nu_e}}{dE} + B_\tau \frac{dN^e_{\nu_\tau}}{dE} = \sum_l B_l \frac{dN^e_{\nu_l}}{dE} \tag{28}$$

where l is the respective lepton and B_l is the respective lepton flavour fraction. Since our observational targets are at large distances, on the kpc scale, we are in the limit of fully averaged (vacuum) oscillations, where the oscillation probabilities can be assumed to be symmetric [66]. We therefore set $B_e = B_\mu = B_\tau = \frac{1}{3}$ and the Annihilation Cross-Section is then given by:

$$\langle \sigma v \rangle_\psi = \frac{6m_\psi^2}{J} S^{\text{obs}}_{\nu_\mu}(E) \left(\sum_l \frac{dN^e_{\nu_l}}{dE} \right)^{-1} \tag{29}$$

Similarly, the Decay Rate, Γ_ψ, is given by:

$$\Gamma_\psi = 3\frac{m_\psi}{D} \left(\sum_l \frac{dN^e_{\nu_l}}{dE} \right)^{-1} S^{\text{obs}}_{\nu_\mu}(E) \tag{30}$$

The ν_μ yield, along with the $\langle \sigma v \rangle_\psi$, Γ_ψ results for the μ^- / μ^+ channel are identical to the those in 28, 29 and 30, but with $f = \mu$ and $B_\mu = 1$.

In the 3l democratic case, the differential ν_μ yield is given by:

$$\frac{dN^{3l}_{\nu_\mu}}{dE} = \sum_l B_l \frac{dN^{3l}_{\nu_l}}{dE} \tag{31}$$

Now, the 3l democratic yield is given by:

$$\frac{dN^{3l}_{\nu_l}}{dE} = \sum_f B_f \frac{dN^f_{\nu_l}}{dE} \tag{32}$$

Employing the Einstein summation convention, we can thus write the differential yield in 33 as:

$$\frac{dN^{3l}_{\nu_\mu}}{dE} = B_l B_f \frac{dN^f_{\nu_l}}{dE} \tag{33}$$

Now, if we set $B_f = \frac{1}{3}$ and $B_l = \frac{1}{3}$, necessarily re-introducing the summation symbols, the Annihilation Cross-Section and Decay Rate are given by:

$$\langle \sigma v \rangle_\psi = 18\frac{m_\psi^2}{J} S^{\text{obs}}_{\nu_\mu}(E) \left(\sum_l \sum_f \frac{dN^f_{\nu_l}}{dE} \right)^{-1} \tag{34}$$

$$\Gamma_\psi = 9\frac{m_\psi}{D} \left(\sum_l \sum_f \frac{dN^f_{\nu_l}}{dE} \right)^{-1} S_{\nu_\mu^{\text{obs}}}(E) \tag{35}$$

6. Radio Wave Production from Synchrotron Emission

As in [65], the average power of synchrotron radiation at observed frequency ν, emitted by an electron with energy E at position r in the Halo is given by:

$$P_{\mathrm{syn}}(\nu, E, r, B, z) = \int_0^{\pi} d\theta \frac{\sin\theta}{2} 2\pi\sqrt{3 r_e} m_e c \nu_g F_{\mathrm{syn}}\left(\frac{\kappa}{\sin\theta}\right) \tag{36}$$

where B is the amplitude of its magnetic field and z is the redshift of the Halo. Synchrotron emission is produced by a charged particle that is relativistic, accelerated under the influence of the Lorentz force resulting from the magnetic field of the Halo. Therefore, we needn't consider synchrotron emission from the muon and tauon populations, given that the significantly larger masses of the other charged leptons push their velocities down into the non-relativistic domain, despite the fact that they are produced by the Annihilation of TeV WIMPs.

The κ term in Equation 36 is defined as follows [65]:

$$\kappa = \frac{2\nu(1+z)}{3\nu_g \gamma^2} \left(1 + \left(\frac{\gamma \nu_p}{\nu(1+z)}\right)^2\right)^{\frac{3}{2}} \tag{37}$$

where γ is the electron Lorentz factor and ν_p is the plasma frequency. The plasma frequency ν_p of the local thermal electron population is directly proportional to $\sqrt{n_e}$, where n_e is the density of the local thermal electron population [65].

Now, the classical electron radius in 36, r_e, is given by [65]:

$$r_e = \frac{1}{4\pi\epsilon_0} \frac{e^2}{m_e c^2} \tag{38}$$

where m_e is the electron mass, e is the electron charge and c is the speed of light.

The non-relativistic gyro-frequency of the electron, ν_g in 36, is given by [65]:

$$\nu_g = \frac{eB}{2\pi m_e c} \tag{39}$$

By substituting the definitions of r_e and ν_g, followed by simple algebra, we derive the following expression for the average power of the synchrotron radiation, this time explicitly as a function of the magnetic field B:

$$P_{\mathrm{syn}}(\nu, E, r, B, z) = \sqrt{\frac{3}{4 m_e}} \frac{e^2 B}{c} \int_0^{\pi} d\theta \sin\theta F_{\mathrm{syn}}\left(\frac{\kappa}{\sin\theta}\right) \tag{40}$$

The Bessel function $F_{syn}(x)$ is defined as in [65]:

$$F_{\mathrm{syn}}(x) = x \int_x^{\infty} dy K_{\frac{5}{3}}(y) \approx 1.25 x^{\frac{1}{3}} e^{-x} \left(648 + x^2\right)^{\frac{1}{12}} \tag{41}$$

where $K_{\frac{5}{3}}(y)$ is a modified Bessel function of the second kind.

Now, given the average power of the synchrotron radiation, P_{syn}, the local emissivity for synchrotron emission, j_{syn} can be written as in [65]:

$$j_{syn}(\nu, E, r, B, z) = \int_{m_e}^{m_\psi} dE \left(\frac{dn_{e^-}}{dE} + \frac{dn_{e^+}}{dE} \right) P_{syn}(\nu, E, r, z, B) \tag{42}$$

where $\frac{dn_{e-}}{dE}$ and $\frac{dn_{e+}}{dE}$ are the equilibrium electron and positron distributions respectively, resulting from DM Annihilation or Decay [65]. As in [65], the equilibrium electron distribution (and similarly with the equilibrium positron distribution) is found as a stationary solution to the following equation:

$$\frac{\partial}{\partial t}\left(\frac{dn_e}{dE}\right) = \nabla \cdot \left[D(E,r)\nabla\left(\frac{dn_e}{dE}\right)\right] + \frac{\partial}{\partial E}\left(b(E,r)\frac{dn_e}{dE}\right) + Q_e(E,r) \tag{43}$$

where [65]:

- D(E,r) is the diffusion function.
- b(E,r) is the energy loss function.
- $Q_e(E,r)$ is the electron source function for DM Annihilation and Decay.

Following [67], we define the energy loss function for electrons at energy E and at a distance r from the centre of the halo as:

$$b(E,r) = b_{\text{IC}}E^2 + b_{\text{syn}}E^2\overline{B}^2 + b_{\text{Coul}}\overline{n}\left(1 + \frac{1}{75}\log\left(\frac{\gamma^*}{\overline{n}}\right)\right) + b_{\text{Brem}}\overline{n}E \tag{44}$$

where $\gamma^* = \frac{E}{m_e c^2}$ and:

- $\overline{n}$ is the Halo's average gas density.
- $\overline{B}$ is the average magnetic field.
- b_{syn} is the synchrotron energy loss factor.
- b_{IC}, b_{Coul} and b_{Brem} are the Inverse Compton, Coulomb and Bremsstrahlung energy loss factors respectively.

In solving Equation 43, two approaches can be taken. The first involves the use of a Greens function method. First consider the solution to Equation 43 for the equilibrium electron (/positron) distributions, when diffusion is negligible, as given in [68]:

$$\frac{dn_e}{dE} = \frac{1}{b(E)}\int_E^{m_\psi} dE' Q_e(E', r) \tag{45}$$

However, in dwarf spheroidal galaxies such as those under consideration in this work, diffusion is not negligible and so the solution to Equation 43 takes the form in [56]:

$$\frac{dn_e}{dE} = \frac{1}{b(E)}\int_E^{m_\psi} dE' Q_e(E', r) G(r, E, E') \tag{46}$$

where $G(r, E, E')$ is a Greens function. Through implementation of the Greens function method, as detailed in [56], we find the equilibrium electron/positron distribution.

The second approach involves the use of an *Alternating Direction Implicit* (ADI) method, which solves Equation 43 numerically, in contrast to the semi-analytical approach taken by Green's function methods [69]. This is implemented through the discretisation of Equation 43 followed by an iterative solution for the equilibrium electron distribution, as detailed in [69]. For ADI methods, the diffusion function and the energy loss function retain their full spatial dependence [67]. Further detail on the implementation of this *operator splitting* method can be found in [70].

Given the equilibrium electron (and positron) distributions, we can now solve the integral in 42 for the local emissivity for synchrotron emission, j_{syn} . Now, given this local emissivity, we can find the flux density spectrum S_{syn} within a radius r by integrating the local emissivity over the volume of a sphere with radius r and then distributing it across the surface area of a sphere with radius D_L , the luminosity distance to the dwarf spheroidal:

$$S_\nu(\nu, r, z) = \int_0^r d^3r' \frac{j_{syn}(\nu, r', z)}{4\pi D_L^2} \tag{47}$$

7. WIMP Mean Free Path and Mean Annihilation Period

Both $\langle \sigma v \rangle_\psi$ and Γ_ψ , along with the WIMP mass, m_ψ , are physical quantities which describe intrinsic qualities of the WIMP, characterising it independently of the global Halo environment. The Decay Rate can be related to another intrinsic physical quantity, the WIMP mean lifetime, τ_ψ , by a simple inverse relation. The severe extent to which the Decay channel has been suppressed is evident from the comparison between τ_ψ and t_H , the Hubble time.

Within our chosen Halo environment, a set of dwarf spheroidal galaxies orbiting the Milky Way, we can relate the constraints upon the Annihilation channel to physical quantities which describe the behaviour of the WIMP in the dwarf spheroidal galaxy under consideration. Given the velocity-averaged Annihilation Cross-section, we calculate further physical quantities which describe the kinematic behaviour of the WIMP in the Halo, like WIMP Mean Free Path (MFP, $\langle \lambda \rangle_\psi$).

We consider the trajectory of a single WIMP in the Halo. It is noteworthy that the Mean Free Path (MFP) of the WIMP - the distance, on average, it travels inside the Halo before it meets an identical WIMP and self-Annihilates - is not a vector describing the WIMP's trajectory, but instead a scalar quantifying the distance it traverses, following any highly irregular trajectory inside of the N-body system of the Halo.

We assume that $\langle \lambda \rangle_\psi$ is a function of $\langle \sigma v \rangle_\psi$, as given by Equation 18, the WIMP number density, $\langle N \rangle_\psi$ and the average WIMP velocity, $\langle v \rangle_\psi$. The line-of-sight velocity dispersion, σ_{los} , characterises the bulk properties of the Halo, quantifying the spread of velocities along the line-of-sight. Assuming that the of the gravitationally-bound WIMP distribution in the Halo is isotropic, we take it as a fair approximation of the total velocity dispersion (σ). Following convention, we take σ as an approximation for the mean velocity of the WIMP, which we know to be highly non-relativistic in the Cold DM scenario . We therefore have: $\langle v \rangle_\psi \approx \sigma_{\text{los}} = \beta c$ where $\beta << 1$.

We further make the reasonable assumption that the $\langle \lambda \rangle_\psi$ is inversely proportional to $\langle N \rangle_\psi$. From simple dimensional analysis, with the implicit assumption that the cosmological scale factor $a(t)$ is set to unity $(a(t_0) = 1)$, we have the following equation for the Mean Free Path.

$$\langle \lambda \rangle_\psi = \frac{\sigma_{\text{los}}}{\langle \sigma v \rangle_\psi \langle N \rangle_\psi} \tag{48}$$

As expected, $\langle \lambda \rangle_{\psi}$ is also inversely proportional to $\langle \sigma v \rangle_{\psi}$. Now the WIMP number density is related to the mass density, $\langle \rho \rangle_{\psi}$ by:

$$\langle N \rangle_{\psi} = \frac{\langle \rho \rangle_{\psi}}{m_{\psi}} \tag{49}$$

For any arbitrary Halo boundary radius r , the average mass density is given by:

$$\langle \rho \rangle_{\psi} = \frac{\int \rho_{\psi}(r) d^3 r}{V_{Halo}} = \frac{4\pi D_L^2}{V_{\text{Halo}}} \int \frac{\rho_{\psi}(r)}{4\pi D_L^2} d^3 r \tag{50}$$

By employing the definition of the astrophysical D-factor in Equation 15 and some basic algebra, we derive the following expression for the average mass density.

$$\langle \rho \rangle_{\psi} = 3D \frac{D_L^2}{r^3} \tag{51}$$

Therefore, with the boundary of the Halo set to an arbitrary radius r, the Mean Free Path is given by:

$$\langle \lambda \rangle_{\psi} = \frac{\sigma_{\text{los}} m_{\psi} r^3}{3 \langle \sigma v \rangle_{\psi} D D_L^2} \tag{52}$$

The mean free path acts as an illustrative metric of the extent to which the Annihilation channel is suppressed, but it is equally physical quantity: a scalar proper length - traversed by a WIMP with mean velocity $\langle v \rangle_{\psi} = \beta c$ (where $\beta << 1$) - upon a highly irregular, unpredictable trajectory (s) in infinitesimal increments.

This distance can therefore be easily related to the time taken, on average, for a WIMP pair to 'meet' and self-Annihilate, by dividing by the WIMP Mean velocity, which we approximate again as σ_{los} . Given the infinite sum of length increments to calculate the scalar distance upon the irregular trajectory of the WIMP, the relation between the Mean Free Path and this average time is best expressed in integral form:

$$\int_0^{\langle T \rangle_{\psi}} dt = \frac{1}{\sigma_{\text{los}}} \int_0^{\langle \lambda \rangle_{\psi}} ds \tag{53}$$

where $\langle T \rangle_{\psi}$ is the *Mean Annihilation Period* (MAP). We have taken the time to be the proper time given that the WIMPs are non-relativistic.

Setting the Halo boundary to the scale radius and solving the trivial bound integrals in Equation 53, $\langle T \rangle_{\psi}$ at $r = r_s$ is:

$$\langle T \rangle_{\psi,s} = \frac{m_{\psi} r_s^3}{3 \langle \sigma v \rangle_{\psi} D D_L^2} \tag{54}$$

Halo Boundary at the Virial Radius

At the virial radius Halo boundary, we have the following relation for the average mass density, as presented in [71]:

$$\langle \rho \rangle_{\psi} = 18\pi^2 \rho_c \tag{55}$$

where ρ_c is the critical density, in flat space ($\kappa = 0$). Substituting Equation 55 into Equations 49 and 48, the Mean Free Path of the WIMP in the Halo, with $r = r_{\mathrm{vir}}$ is given by:

$$\langle \lambda \rangle_\psi = \frac{\sigma_{\mathrm{los}} m_\psi}{\langle \sigma v \rangle_\psi 18\pi^2 \rho_c} \tag{56}$$

Solving the trivial integral in 53 for the MFP at the Virial Halo boundary in Equation 56 yields the following formula for the Mean Annihilation Period at $r = r_{\mathrm{vir}}$:

$$\langle T \rangle_{\psi,v} = \frac{m_\psi}{\langle \sigma v \rangle_\psi 18\pi^2 \rho_c} \tag{57}$$

The critical density is related to the Hubble constant at present time $H(t_0) = H_0$ by Alexander Friedmann's solutions to the Einstein field equations, presented in [72] and [73]. With $\kappa = 0$, this relation is given by [72]:

$$\rho_c = \frac{3H_0^2}{8\pi G} \tag{58}$$

where G is Newton's gravitational constant.

We note that the equation for the WIMP MAP at the virial radius Halo boundary in 57 is independent of all other Halo features, reliant only upon the WIMP mass m_ψ and its corresponding Annihilation cross-section $\langle \sigma v \rangle_\psi$. Therefore, Equation 57 states that for any DM Halo, when the Halo boundary is set to its virial radius, the Mean Annihilation Period of WIMPs ψ (characterised by m_ψ and $\langle \sigma v \rangle_\psi$) inside the Halo will be constant.

We further note that at the virial radius, Equation 52 for $\langle \lambda \rangle_\psi$, when $r = r_{\mathrm{vir}}$, must be equivalent to Equation 56 for $\langle \lambda \rangle_\psi$. Solving simultaneously we find a relation for the astrophysical D-factor an angle θ which corresponds to the Virial Halo boundary. This will be discussed in further detail in Appendix C.

IV. Implementation of Theory

1. Choice of Target Dwarf Galaxies

We choose the target dwarf spheroidals based on a number of metrics:

- The position of the dwarf spheroidal galaxy in the sky (its declination angle) and whether it is within the field of view of at least 3 of the 4 telescopes under consideration
- The astrophysical J- and D- factors of the dwarf spheroidals
- The (line-of-sight) velocity dispersion, σ_{los}, of the dwarf spheroidals
- The absolute magnitude, M_V, of the dwarf spheroidals
- The spatial extent of the Halo (quantified by both the half-light radius, r_h and the scale radius r_s)
- The luminosity distance, D_L, to the target dwarf spheroidals.

in addition to the relative errors associated with these quantities for the various dwarf galaxies.

In light of these criteria, we choose the following six dwarf spheroidal galaxies as potential observational target environments for multi-messenger Indirect DM searches:
Two Classical dwarfs (Sculptor and Sextans) along with four Ultrafaint dwarfs (Segue 1, Tucana II, Reticulum II and Triangulum II). Each of these dwarf galaxies will be discussed in more detail below.

i Sculptor

In a March 1938 bulletin of the Harvard Observatory, Harlow Shapley, announced the discovery of a *"stellar system of a new type"* in photographic observations in the Sculptor constellation[74]. While preliminary observations suggested that the system may be an extended galaxy cluster, follow-up observations confirmed that the individual members are stars, not spheroidal galaxies [74]. Shapley notes that the most *"outstanding feature"* of the newly-discovered system is that the brightest member stars are extremely faint and that the surface brightness is *"remarkably low"* [74].

Shapley reports that the Sculptor cluster exhibits no sharp nucleus [74], thus favoring a cuspy density profile, and the observed half-light radius quoted in [26] is approximately 220 pc. It also evidently lacks conspicuous nuclear stars, irregular nebulae or sub-clusters [74]. Assuming that the brightest member stars have an absolute magnitude of $M_V = -1.5$, mirroring the maximum luminosity of stars in globular clusters, Shapley calculates a luminosity distance to Sculptor of approximately 80 kpc [74], which is consistent with the observed distance to Sculptor from [26], presented in Table 3. Employing the same assumption, Shapley calculates the linear radius of Sculptor as approximately 1 kpc, more than 10 times that of an average globular cluster [74]. The absolute magnitude of the Sculptor dwarf galaxy as a totality, as quoted in [26] is $M_V \approx -11$, the lowest absolute magnitude value amongst all of our target dwarf spheroidals, corresponding to the highest intrinsic brightness in our sample.

In October of that year, Shapley published a paper in Nature following the discovery of a similar stellar system in the Fornax constellation [75]. These systems are both satellites of the Milky Way and became the first two of the *Classical* dwarf elliptical galaxies [76].

ii Sextans

In 1990, another *'Sculptor-type'* Milky Way satellite, by then the eighth Classical dwarf galaxy of its kind, was discovered in the Sextans constellation in UKST sky survey plates and was announced in the Monthly Notices of the Royal Astronomical Society [76]. The Sextans dwarf galaxy was initially reported to have an absolute magnitude of $M_V \approx -8$ [76]. Since then, it has been established that the absolute magnitude of Sextans is lower, quoted in [26] as $M_V = -9.1 \pm 0.1$ The resultant colour-magnitude diagram (CMD) exhibits a well-defined asymptotic giant branch, along with a pronounced red horizontal branch possessing an extended blue tail, which has been found to be a characteristic feature of dwarf spheroidal galaxies [76].

Sextans is found to have a major-axis diameter of 2 kpc [76] and the Sextans half-light radius of approximately 0.5 kpc quoted in [26] is the largest among our six target dwarf spheroidals, as can be seen in Table 3. The luminosity distance to Sextans was initially calculated as approximately 85 kpc [76], but more observations have allowed for a more accurate value of $D_L = 92.5 \pm 2.2\,kpc$, making the Sextans dwarf the most distant among our chosen dwarf spheroidals, followed by the other Classical dwarf, Sculptor, as quoted in [26].

iii Segue I

In 2007, the Segue 1 Milky Way Satellite, along with four other dwarf galaxies, was discovered in the Sloan Digital Sky Survey (SDSS) data and announced by Belokurov et. al. [77]. In [77], the heliocentric distance to Segue 1 is given as 23 ± 2 kpc and its absolute magnitude is given as $M_V = -3.0 \pm 0.6$. The half-light radius of Segue 1, quoted in [77] as approximately 30 pc, is relatively small in comparison to those of the other dwarf spheroidals and is noted to be around the same size as the largest globular clusters orbiting the Milky Way [77]. Moreover, the Segue 1 CMD, unlike those for the other dwarf galaxies, exhibits no pronounced horizontal branch and its sub-giant branch is poorly populated [77]. Therefore, the discoverers of Segue 1 tentatively classify it as an extended globular cluster , rather than a dwarf galaxy, pending a kinematic analysis of the system [77].

In the year following the discovery of Segue I, a maximum likelihood analysis of the structural properties of faint MW Satellites was conducted in [78], resulting in a half-light radius consistent with that in [77], although the authors calculate a greater ellipticity than was reported in [77]. In a 2009 follow up study on the origins of the newly discovered Milky Way satellite, the authors employ an optimal filter technique to argue that Segue 1 is a star cluster, which originated in the Sagittarius galaxy [79]. They conclude that, with the evidence at hand, tidal distortion from the Sagittarius stream is artificially increasing the velocity dispersion of Segue 1, leading to an overstated mass-to-luminosity ratio and hence a mischaracterisation of the MW Satellite as an Ultrafaint dwarf [79].

In 2011, a comprehensive spectroscopic Keck/DEIMOS survey of Segue 1 led to the identification of 71 stars which are likely members of the Segue 1 Milky Way Satellite [80]. Velocity measurements were taken for 98.2% of the stars within 67 pc of the Segue 1 centre (which is approximately 2.3 times greater than the Segue 1 half-light radius) [80]. The stellar kinematics necessitate a high mass-to-luminosity ratio of Segue 1 in the visible waveband, calculated as $3400\,M_\odot/L_\odot$ [80]. The total luminosity of Segue 1 is less than that of a single bright red giant star, making it the darkest galaxy known at the time of the survey's publication[80]. Reinforcing the classification of the Milky Way satellite as a dwarf galaxy is the finding that Segue 1 has a large metallicity spread amongst its member stars, with two members studied having extremely low metallicities [80].

Of our six target dwarf spheroidal galaxies, Segue 1 has the highest empirical J-factor, as calculated in [26], with $\log\left(J(0.5^{\circ})\right) = 19.12^{+0.49}_{-0.58}$. Within the error bounds, this value for the Segue 1 J-factor is consistent with the Segue 1 J-factor of $\log\left(J(0.5^{\circ})\right) = 19.41^{+0.39}_{-0.40}$ calculated analytically in [64].

iv Tucana II

In a paper that appeared in the Astrophysical Journal in June 2015, a group of Cambridge researchers, using publicly released data from the Dark Energy Survey (DES), announced the discovery of nine Ultrafaint Milky Way Satellites in the vicinity of the Large Magellanic Cloud [81]. In July 2015, the DES Collaboration published its own paper, independently announcing the discovery of eight new Milky Way satellites [82]. Tucana II was independently discovered in the DES data by both collaborations and so we use the term 'Tucana II K' (Koposov et. al.) to denote the parameters derived from the first work in [81] and 'Tucana II B' (Bechtol et. al.) to denote the parameters derived from the latter work by DES in [82].

Tucana II B was tentatively classified as a dwarf galaxy by the DES collaboration on the basis that it is sufficiently large (with a calculated half-light radius of 120^{+30}_{-30} pc) to do so entirely on the basis of multi-band photometry [82]. The DES collaboration argues that the relative distance between Tucana II and the Large Magellanic Cloud (at ~ 19 kpc) on the one hand and the Small Magellanic Cloud (at 37 kpc) on the other places the newly discovered dwarf galaxy as a strong candidate for another member of the Magellanic group [82]. Like most dwarf galaxies orbiting the Milky Way, Tucana II is ancient, with an age on the order of 10 billion years old [83].

The authors of [81] calculate a half-light radius of $165^{+27.8}_{-18.5}$ pc, which is higher than that calculated in [82], but still within the error margin. They, too, classify Tucana II as an Ultrafaint dwarf, noting that doing so is made less ambiguous by its large spatial extent and its low absolute magnitude, which they calculate to be $M_V = -3.8 \pm 0.1$ [81]. This is consistent with the DES Collaboration's Absolute Magnitude of $M_V = -3.9 \pm 0.2$, as is the Luminosity distance to Tucana II, calculated as ~ 60 kpc in both [82] and [81].

In February 2021, a paper by Chiti et. al. [83] announced that the DM Halo around Tucana II was far larger than previously estimated. They identify members of the Tucana II dwarf up to nine half-light radii from the centre, observationally establishing, for the first time, an extended DM Halo surrounding an Ultrafaint up to a distance of 1 kpc [83]. This is found to be consistent with a generalized NFW profile, with a total predicted mass of $\sim 2 \times 10^7 M_{\odot}$ [83].

v Reticulum II

Like Tucana II, Reticulum II was also discovered independently in the 2015 DES data by the studies in [81] and [82]. Similarly to the case for Tucana II, we denote the parameters from the former work in [81] by 'Reticulum II K' and those from the latter work in [82] as 'Reticulum II B'. In choosing which parameters to utilize, we choose the more conservative result for the J-factors in the case of both dwarf spheroidals - Tucana II K and Reticulum II B, respectively.

Reticulum II is an ancient dwarf galaxy with an age on the order of 10 Gyr, which is calculated in [82], within wide error bounds, as $\tau = (12.023 \pm 5.814)\ Gyr$. Among all the dwarfs discovered in the 2015 DES data, Reticulum II is the closest, with a luminosity distance of approximately 30 kpc, as calculated in both [81] and [82].

While the authors of [81] carefully classify Reticulum II as an *"Ultrafaint satellite"*, leaving open the possibility of the system being an extended globular cluster, the DES collaboration argues that Reticulum II can be classified with near certainty as a dwarf galaxy given its radius, luminosity and ellipticity [82].

The half light radius calculated by the DES collaboraton in [82] is $r_h = 55 \pm 5$ pc, while in [81], it is calculated as $r_h = 32^{+1.9}_{-1.1}$ pc, which partially accounts for the latter group's hesitation in classifying Reticulum II as an an Ultrafaint dwarf, given the understating of its spatial extent. A disparity exists between the reported values for the absolute magnitude as well, with the DES collaboration quoting it as $M_V = -3.6 \pm 0.1$ in [82] and the Cambridge group quoting a higher value of $M_V = -2.7 \pm 0.1$ in [81]. We follow [26] in taking the (lower) DES value as the Reticulum II absolute magnitude. The classification of Reticulum II as a dwarf galaxy by the DES collaboration has since been vindicated by further observations, as is evident in the Halo parameters presented in [26], reproduced in Table 2.

vi Triangulum II

In 2015, the Panoramic Survey Telescope and Rapid Response System (PanSTARRS) discovered a faint (Absolute Magnitude: $M_V = -1.8 \pm 0.5$) Milky Way Satellite, later named Triangulum II, in the 3π imaging data and subsequently confirmed the discovery with wide-field photometry from the Large Binocular Cameras [48]. It is found to be "old and metal poor", has a half-mass radius of approximately 34 pc and is located at a distance of about 30 kpc from the sun [48].

This newly discovered dwarf spheroidal Galaxy quickly became a potential target environment for DM Indirect detection, with Genina and Fairbairn authoring a 2016 paper on the subject [47]. They assume a NFW density as in Equation 9, with the scale density $\rho_s = 6.4x10^7 M_\odot\ \text{kpc}^{-3}$ and scale radius $r_s = 1.0$ kpc, along with a constant stellar anisotropy profile [47]. Utilising a Jeans analysis, they calculated the J-factor for Triangulum II on the order of $10^{20} - 10^{22}\text{GeV}^2\text{cm}^{-5}$ - one of the highest calculated J-factors of any Classical or Ultrafaint dwarf [47]. However, the value of the J-factor at $\theta = 0.5°$ for Triangulum II $\left(\log_{10}(J) = 21.03^{+0.83}_{-0.57}\right)$ is based upon an extrapolation of the density profile beyond the angle of the furthest star, at a confidence level of 68% [47]. Moreover, only 14 stars are considered in their analysis and thus the authors stress that follow-up studies, identifying a larger number of stars and their line of sight velocities, are essential before their calculated J-factor can be used to motivate Triangulum II as a target object [47].

The 2018 study by Pace and Strigari in [26] calculates an approximate upper bound for the Triangulum II J-factor at 0.5° as $\log(J) = 19.73$, where upper limits are quoted at a 99.5% confidence interval, after applying a cut at $\log_{10}(\rho_s) > 4$ [26]. This is on account of the fact that Triangulum II remains an unresolved system, without a securely measured σ_{los} [26]. These J-factor upper limits are quoted at a higher confidence interval and despite being upper limits, are more conservative than those calculated in [47]. They are thus more apt for use in this work.

vii Overview of Selected Target Objects

In Figure 17, the red dots indicate the location, in Galactic Co-ordinates, of the Milky Way Satellites discovered by the DES collaboration in 2015 [82]. As seen in the figure, the DES MW Satellites are in the region of the Magellanic Clouds. Two of our six target dwarf galaxies, the Ultrafaints Reticulum II and Tucana II, were discovered in the DES data [81] [82]. The Ultrafaint Segue 1, discovered 8 years prior [77], is also visible, in proximity to the Classical Sextans, both of which we consider as observational targets. Sculptor, the first dwarf spheroidal Galaxy to be discovered [74] is visible in the proximity of the newly-discovered DES MW Satellites.

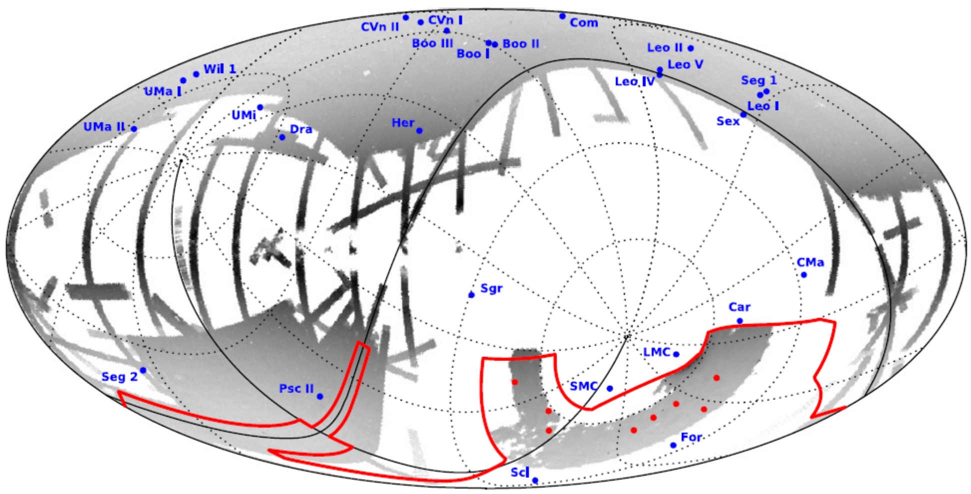

Figure 17: *Mollweide Projection of the Milky Way Satellites discovered by the DES collaboration in 2015 [82]. Five of our target dwarf spheroidals are visible in the projection, with the dwarf spheroidals discovered prior to the DES discovery indicated by blue dots.*

Our sixth observational target, the Ultrafaint Triangulum II, is not visible on the DES Mollweide projection as it was also discovered in 2015 [48].

In selecting the values for the most important observational metric for DM Indirect detection - the empirical J- and D-factors of the target dwarfs - we utilize the 2018 analysis in [26], wherein Pace and Strigari use a generalised NFW Halo density profile to parameterize the DM density distribution. They employ a spherical Jeans-based like analysis to calculate the J- and D-factors for a number of dwarf spheroidals, including our observational targets [26].

The J-factors and D-factors calculated in [26] are presented in Table 2, along with the multi-messenger telescopes that are able to observe the target dwarfs within their respective fields of view. The J- and D-factors are quoted in $\mathrm{GeV^2cm^{-5}}$ and $\mathrm{GeVcm^{-2}}$ respectively [26]. All relevant observational results are taken at a telescope opening angle of $\theta = 0.5^\circ = 30$ arcmin.

Dwarf Spheroidal	**Classification**	$\log\left(\frac{J}{\mathrm{GeV^2cm^{-5}}}\right)$	$\log\left(\frac{D}{\mathrm{GeVcm^{-2}}}\right)$	**Telescopes**
Segue I	Ultrafaint	$19.12^{+0.49}_{-0.58}$	$18.08^{+0.53}_{-0.49}$	(a), (b) (c)
Reticulum II B	Ultrafaint	$18.88^{+0.39}_{-0.37}$	$18.30^{+0.33}_{-0.50}$	(a),(d) (c)
Tucana II K	Ultrafaint	$18.84^{+0.55}_{-0.50}$	$18.41^{+0.32}_{-0.33}$	(a), (c)
Sculptor	Classical	$18.58^{+0.05}_{-0.05}$	$18.20^{+0.09}_{-0.08}$	(a), (d) (c)
Sextans	Classical	$17.73^{+0.13}_{-0.12}$	$17.90^{+0.11}_{-0.09}$	(a), (d) (c)
Triangulum II	Ultrafaint	< 19.73	< 18.72	(a), (b) (c)

Table 2: *J-factors and D-factors of target dwarf spheroidals in the field of view of multi-messenger telescopes, taken from [26].*
The letters (a), (b), (c) and (d) represent CTA, LHAASO, KM3NeT and MeerKAT respectively.

In Table 2, we see that all six dwarf spheroidals in our sample are within the field of view of both CTA (a) and KM3NeT (c). For LHAASO projections (b), we consider only the Ultrafaints Segue 1 and Triangulum II as observational target environments, while for MeerKAT projections (d), we consider observations of Tucana II K, Sculptor and Sextans.

The J- and D-factors in Table 2 for the Ultrafaints are generally greater than those of the Classicals, illustrating the suitability of the Ultrafaints as observational target objects. However, the relative errors on both the J- and D-factors in the case of the Classical dwarfs are significantly smaller than those for the Ultrafaints, reflecting the lack of kinematic data on these newly discovered systems [26]. Of the two Classical dwarfs, Sculptor has significantly higher J- and D-factors than Sextans, with the Sculptor J- and D-factor values comparable to those of the Ultrafaints, with the added advantage that the error margins in the case of this Classical dwarf are far smaller than those for the Ultrafaints, allowing for a more accurate set of results.

For the purposes of the multi-messenger analysis, we shall select the Ultrafaints Segue 1 and Reticulum II, as well as the Classical dwarf Sculptor as fixed observational targets so that comparisons can be made between the bounds imposed by non-detection in the gamma ray, neutrino and radio domains, utilizing the telescopes denoted in Table 2. Thus, for Segue 1, we compare non-detection constraints by KM3NeT in the neutrino domain, alongside CTA and LHAASO in the gamma ray domain. In the case of both Reticulum II and Sculptor, KM3NeT and CTA projected non-detection bounds are compared to those imposed upon the e^-/e^+ channel by the non-detection of synchrotron emission by MeerKAT in the radio domain.

We omit LHAASO non-detection constraints from the analysis of the latter two dwarf spheroidals, since they primarily serve as a point of comparison for the CTA non-detection constraints in the gamma ray domain. Instead, we focus on the inclusion of the MeerKAT non-detection bounds to allow for a more comprehensive multi-messenger analysis, since it allows for direct comparison between the projected non-detection bounds set by observations with next generation telescopes in the gamma ray, neutrino and radio domains respectively.

In order to calculate the constraints in the radio domain, as well as the Mean Free Path, Mean Annihilation Period and mass at the half-light radius of the Halo under consideration, we require the physical parameters describing the Halo features. The relevant parameters characterising the Halo are taken from [26] and presented in Table 3. The approximate Halo mass at the half light radius, M_h calculated from Equation 11, is also presented in the table.

Dwarf Galaxy	$\sigma_{\mathbf{los}}$ (km/s)	D_L**(kpc)**	r_h (pc)	M_V	M_h $(10^6 M_\odot)$
Sextans	$7.1^{+0.3}_{-0.3}$	$92.5^{+2.2}_{-2.2}$	523^{+23}_{-23}	$-9.1^{+0.1}_{-0.1}$	$24.52^{+3.15}_{-3.15}$
Sculptor	$8.8^{+0.2}_{-0.2}$	$83.9^{+1.5}_{-1.5}$	223^{+5}_{-5}	$-11.04^{+0.5}_{-0.5}$	$16.06^{+1.09}_{-1.09}$
Tucana II K	$7.3^{+2.6}_{-1.7}$	$57.5^{+5.3}_{-5.3}$	162^{+35}_{-35}	$-3.8^{+0.1}_{-0.1}$	$8.03^{+7.45}_{-5.47}$
Reticulum II B	$3.4^{+0.7}_{-0.6}$	$32.0^{+2.0}_{-2.0}$	34^{+8}_{-8}	$-3.6^{+0.1}_{-0.1}$	$0.37^{+0.24}_{-0.21}$
Triangulum II	< 6.36	$30.0^{+2.0}_{-2.0}$	28^{+8}_{-8}	$-1.8^{+0.5}_{-0.5}$	$1.04^{+0.30}_{-0.30}$
Segue I	$3.1^{+0.9}_{-0.8}$	$23.0^{+2.0}_{-2.0}$	21^{+5}_{-5}	$-1.5^{+0.7}_{-0.7}$	$0.19^{+0.15}_{-0.14}$

Table 3: *Halo parameters: the line-of-sight velocity dispersion (σ_{los}), luminosity distance (D_L) the azimuthally-averaged half-light radius (r_h), the absolute magnitude (M_V) [26] and the calculated Halo mass at the half-light radius (M_h)*

In general, the Classical dwarfs are at a greater distance and are more spatially extended than the Ultrafaints, with the exception of Tucana II. Even our most distant dwarf spheroidal, Sextans, is well within the MW virial radius of $\sim$ 300 kpc [22] and thus all of our observational targets are satellites that are gravitationally bound to the Milky Way galaxy. The least spatially extended dwarf in our sample, the Ultrafaint Segue I, with an approximate scale radius of 21 pc, is also the closest, with a luminosity distance of approximately 23 kpc [26]. In Table 2, we see that Segue I is also the dwarf spheroidal with the highest empirical J-factor. We can also see that the lowest values for both the empirical J- and D-factors belong to the Classical Sextans, which is also the most spatially-extended and distant MW satellite, as seen in Table 3.

In Table 3 we also see that the Classicals are far more massive than the Ultrafaints, with the former category having masses at their half-light radii that are at least one order of magnitude greater than those for the Ultrafaints, with the exception of Tucana II, although the significantly larger error bounds for this Ultrafaint must be taken into consideration. The line-of-sight velocity dispersions for the Ultrafaints are also generally lower, which poses challenges for the kinematic analysis since it is more likely for these velocity dispersion values to fall below the detection threshold of current instruments [22]. This results in weaker data sets and manifests in the relatively large error margins for the Ultrafaints in the calculations for the J- and D-factors. Again Tucana II seems to break this trend, but this can be accounted for by considering once again its large error margin.

In assessing the intrinsic brightness of the dwarf spheroidals, we consider the absolute magnitude in the visible waveband, M_V. For the Classicals in the sample, the values for M_V are far lower than those for the Ultrafaints, where even at the lower error bound, $M_V > -4$. The Ultrafaints in Table 3 can be roughly divided into two groups, with Segue 1 and Triangulum II exhibiting the largest values for M_V, consistent within their respective error margins. While Reticulum II and Tucana II have lower Absolute Magnitude values than the other Ultrafaints, they nonetheless have M_V values which are significantly larger than those of the Classicals Sculptor and Sextans, as presented in Table 3. We further note that the M_V for Sculptor is significantly lower than that for Sextans, the other Classical dwarf.

This analysis of the dwarf spheroidals' Absolute Magnitude values illustrates the greater intrinsic brightness of the Classicals, in comparison to the lower intrinsic brightness of the Ultrafaints. The relatively high values for M_V in the case of the Ultrafaints, compared to the significantly lower M_V values for the Classicals, illustrates the extent to which ordinary astrophysical processes are absent in the Ultrafaints, allowing for the analysis of the results without having to account for Baryonic background signals from within the Ultrafaint dwarfs.

2. Annihilation and Decay Spectra

The Annihilation spectra for the respective channels are produced by event generators, as presented in [84], which calculate Annihilation spectra across a wide mass-energy range. In determining the Decay spectra, we simply take the Annihilation spectra at half the mass/energy. For observations in gamma and neutrinos, we use the spectra generated in [85], while the radio observations in the case of synchrotron emission require a different approach.

We have adopted a model-independent approach, over an MLMP mass range of 1 TeV to 2 TeV. The MLMP mass serves as a fixed parameter in all of our calculations, while $\langle \sigma v \rangle_\psi$, Γ_ψ, along with $\langle \lambda \rangle_\psi$ and $\langle T \rangle_\psi$ are our respective free parameters.
We consider the following Annihilation and Decay Spectra:

- The e^-/e^+ channel independently ($B_f = B_e = 1$)
- The μ^-/μ^+ channel independently ($B_f = B_\mu = 1$)
- The $3l$ democratic case, where the MLMP Annihilates or Decays along each leptonic channel with equal frequency ($B_e = B_\mu = B_\tau = \frac{1}{3}$)

3. Importing Established Constraints

The DAMPE constraints from [20], along with the respective constraints from the Indirect searches using ATCA in [23] and Kamiokande in [24], are all extracted using the WebPlotDigitizer software and plotted as points of reference. This is done for all $\langle\sigma v\rangle_{\psi}$ results, across the gamma, radio and neutrino domains. Similarly, the Isotropic Gamma-Ray Background constraints in [25] are extracted and plotted as points of reference for the Γ_{ψ} upper bounds in all three domains.

4. Imposing Constraints in the Gamma Ray Domain: CTA and LHAASO

In the Gamma ray domain, we begin by setting the observed flux spectrum in 18 to the minimum flux detectable by the gamma ray telescope under consideration:

$$S_{\gamma}^{\text{obs}}(E) = S_{\gamma}^{\text{tel,min}}(E) \tag{59}$$

In our case, we are considering CTA and LHAASO in the gamma ray domain and we obtain the minimum detectable flux from the sensitivity curves in [49] and [50]. We use the open-source WebPlotDigitizer software to extract the raw data from the curves, at an opening angle of $\theta = 0.5°$.

In the case of CTA, we calculate the parameter constraints for all six dwarf spheroidals, contrasting the Classical dwarfs with the Ultrafaints. In the case of LHAASO, we calculate the constraints for only Segue I and Tucana II, both of which are Ultrafaints. We then compare the non-detection constraints imposed by CTA and LHAASO observations for both Ultrafaints.

For each mass value, the sensitivity functions constructed from the data in [49] and [50] are evaluated, with the resultant values being used to solve Equation 18 for $\langle\sigma v\rangle_{\psi}$. For a given leptonic Annihilation channel, the smallest results obtained from this set of calculations are then the respective upper bounds on the value of $\langle\sigma v\rangle_{\psi}$. This is then repeated for each target dwarf spheroidal considered by the gamma ray telescope under consideration. In the case of the Decay rate we employ the same methodology when solving Equation 26, selecting the smallest values for Γ_{ψ} as the upper bounds on the WIMP Decay rate.

Given the upper bounds on $\langle\sigma v\rangle_{\psi}$,we can calculate the lower bounds on the Mean Free Path and Mean Annihilation Period, solving equations 52 and 54 for the Halo boundary at the scale radius and equations 56 and 57 for the Halo boundary at the virial radius.

All calculations and plots generated are implemented using Python, utilizing the extracted data from the sensitivity curves and the spectra for each channel from [84]. In the Decay case, we utilise the same spectra from [84], taking the data at half the mass-energy value under consideration.

5. Imposing Constraints in the Neutrino Domain: KM3NeT

In the neutrino domain, the approach is similar and we use the WebPlotDigitizer software to extract the $\theta = 0.5^\circ$ data from the KM3NeT sensitivity plot in [49], allowing us to construct the function for $S_{\nu_\mu}^{\text{KM3,min}}(E)$, the minimum flux detectable by the KM3NeT telescope. We note that we focus primarily on muon neutrinos for KM3NeT, owing to the fact that only muon neutrinos were relevant to KM3NeT in 2018, when the analysis in [49] was conducted. However, the phenomenon of neutrino oscillations requires us to consider production of neutrinos for all three Leptonic channels. We once again obtain these spectra from [84].

In solving the equations for the relevant WIMP parameters, for each mass in the 1 TeV to 2 TeV range, we set the observed flux to the sensitivity function defining the minimum flux detectable by KM3NeT.

$$S_{\nu_\mu}^{\text{obs}}(E) = S_{\nu_\mu}^{\text{KM3,min}}(E) \tag{60}$$

This yields the respective upper limits for the Annihilation/Decay channel under consideration, along with the lower limits on the MLMP MFP and MAP. The process is repeated for each target dwarf spheroidal to obtain the full set of results. All calculations, along with the plots generated, are implemented using Python, utilising the extracted sensitivity data and the differential neutrino yield spectra from [84].

6. Imposing Constraints in the Radio Domain: MeerKAT

For the radio domain, we consider three dwarf spheroidals within the MeerKAT field of view. Of these, Reticulum II B is an Ultrafaint and the other two (Sculptor and Sextans) are Classicals.

For synchrotron emission in the radio domain, we first set the observed flux to the minimum detectable flux by MeerKAT (in Jy arcmin^2) obtained by the MeerKAT continuum sensitivity calculator in Figure 16.

$$S_\nu^{\text{obs}} = S_\nu^{MK,min} \tag{61}$$

We take the ratio of the $S_\nu^{\text{MK,min}}$ to I_ν^{Halo} the calculated surface brightness of the dwarf spheroidal (also in Jy arcmin^2). With the ADI solver assuming $\langle\sigma v\rangle_\psi^{\text{ADI}} = 10^{-26}\text{cm}^3\,\text{s}^{-1}$. We determine the upper bounds on the velocity-averaged Annihilation cross-section using Equation 62:

$$\langle\sigma v\rangle_\psi^{\text{MK}} = \frac{S_\nu^{\text{MK,min}}}{I_\nu^{\text{Halo}}} \langle\sigma v\rangle_\psi^{\text{ADI}} \tag{62}$$

As in the case for Annihilation constraints, we obtain the Decay rate upper bounds as given in Equation 63 by multiplying the dimensionless ratio of the minimum detectable flux by MeerKAT to the calculated surface brightness of the dwarf spheroidal, by the Decay rate assumed by the ADI solver, $\Gamma_\psi^{\text{ADI}} = 10^{-26}\,\text{s}^{-1}$.

$$\Gamma_\psi^{\text{MK}} = \frac{S_\nu^{\text{MK,min}}}{I_\nu^{\text{Halo}}} \Gamma_\psi^{\text{ADI}} \tag{63}$$

We store all of the Halo parameters - specifying its mass density profile, the density profile of the electron gas resulting from MLMP Annihilation (or Decay) and the magnetic field spatial profile - in YAML files. The particle physics parameters specifying the WIMP model, along with the diffusion parameters and the cosmological parameters are also stored in YAML files. The parameters characterising the implementation of the calculation for the electron/positron annihilation channel are also stored in a YAML file. The files are retrieved and the calculations are performed utilising an ADI solver, implemented in Python.

i Halo Density Profile Parameters

In modeling the Halo density profile for the purposes of the radio analysis, Pace and Strigari utilise a generalised NFW profile, which produces J- and D-factors consistent with those referenced before in this work [26]. The scale densities, scale radii and values for β for each of the three dwarf spheroidals are taken from the fits in [26] and are presented in Table 4.

Dwarf Spheroidal	r_s (kpc)	ρ_s $\left(10^6 M_\odot/\text{kpc}^3\right)$	β
Sextans	1.413	10.47	0.661
Sculptor	0.741	61.66	0.562
Reticulum II B	0.200	65.00	1.950

Table 4: *Generalised NFW Halo parameters: The scale density (ρ_s), scale radius (r_s) and the dimensionless β parameter [26]*

ii Electron Gas Density Profile

We follow an exponential density profile for the electron gas, following [23]:

$$n_e(r) = n_0 e^{\frac{r}{r_e}} \tag{64}$$

where r_e, the electron gas scale radius, is set to r_h, the half-light radius for the dwarf spheroidal under consideration. We set the normalisation electron number density to $n_0 = 10^{-6}$ cm^{-3}, as in [23].

iii Magnetic Field Spatial Profile

We follow the argument in [23], accounting for the fact that polarisation measurements are made difficult due to the low content of gas and dust. The authors deploy two physical arguments, the first of which relies upon an extrapolated empirical scaling relation between the star formation rate (assuming a typical star formation rate in Ultrafaints) and the magnetic field strength which is found to hold in the Local Group [23]. The second physical argument considers the magnetisation of the region surrounding galaxies (due to processes like Galactic outflows) yielding the following spatial shape for the magnetic field profile [23]:

$$B(r) = B_0 \exp\left(\frac{-r}{r_*}\right) \tag{65}$$

where $B_0 = 1\mu$G as in [23] and r_* is set to r_h, the half-light radius of the dwarf spheroidal under consideration.

iv Diffusion Environment

Following [23], we first consider the following for the diffusion coefficient $D(E,r)$:

$$D(E,r) = 3 \times 10^{27} \left(\frac{E}{GeV}\right)^{0.3} \exp\left(\frac{r}{r_*}\right) \text{ cm}^2 \text{ s}^{-1} \tag{66}$$

where we once again take $r_* = r_h$. Defining the spectrum and normalisation of the diffusion coefficient in this way produces a MW-like diffusion in the stellar region, which then increases exponentially at larger radii in the outskirts [23].

Alternatively, we can define a diffusion constant as in [86], where there the radial dependence is implicit, on account of the radially dependent magnetic field $B = B(r)$:

$$D(E,B) \approx 10^{27} \left(\frac{E}{GeV}\right)^{\frac{1}{3}} \left(\frac{B(r)}{\mu G}\right)^{-\frac{1}{3}} \text{ cm}^2 \text{ s}^{-1} \tag{67}$$

With the magnetic field spatial profile defined in Equation 65, employing as before the assumption that $B_0 = 1\,\mu\text{G}$, we can write the diffusion function in Equation 67 explicitly in terms of the radial distance from the Halo centre.

$$D(E,r) \approx 10^{27} \left(\frac{E}{GeV}\right)^{\frac{1}{3}} \left(\exp\left(\frac{r}{r_*}\right)\right)^{\frac{1}{3}} \text{ cm}^2 \text{ s}^{-1} \tag{68}$$

We utilise the latter approach, using Equation 68, to model the Diffusion environment when performing our calculations for the MeerKAT non-detection constraints.

7. Interpreting the Mean Free Path and Mean Annihilation Period Limits

In conducting the analysis on the lower limits for $\langle\lambda\rangle_\psi$ and $\langle T\rangle_\psi$, we note that these kinematic quantities are generally dependent on the features of the Halo, in addition to the WIMP parameters, m_ψ and $\langle\sigma v\rangle_\psi$. We set the Annihilation cross-section to the DM Relic density limit calculated in [42], $\langle\sigma v\rangle_\psi = 2.2\times10^{-26}\,\mathrm{cm^3s^{-1}}$, with our WIMP mass remaining the free parameter.

We then consider the Ultrafaint Reticulum II and the Classical dwarfs Sculptor and Sextans, solving equations 52 and 54 for the Mean Free Path and Mean Annihilation Period of WIMPs (with identical values of $\langle\sigma v\rangle_\psi$) within the respective dwarf galaxy, with the Halo boundary at the scale radius. We also solve equations 56 and 57 for the case where the Halo boundary is set to the virial radius. We can thus compare the kinematic behaviour of identical WIMPs within the different Halos, allowing us to compare the limits from the respective dwarf galaxies, along with the cosmological Hubble parameters.

WIMP Mean Free Path

The solutions to the equations for the WIMP Mean Free Path, $\langle\lambda\rangle_\psi$, can usefully be compared to the Hubble distance d_H. We thus define and constrain the dimensionless parameter $\lambda_{\psi,H}$, which quantitatively compares the Mean Free Path of TeV WIMPs in the the Halo to the Hubble distance, d_H.

$$\lambda_{\psi,H} = \frac{\langle\lambda\rangle_\psi}{d_H} \tag{69}$$

The Hubble distance in Equation 70 is calculated from the Hubble constant presented by Planck in [87].

$$d_H = (4.448 \pm 0.033)\,\mathrm{Gpc} \tag{70}$$

WIMP Mean Annihilation Period

As a point of comparison for the Mean Annihilation Period, $T_{\psi,H}$ we consider the age of the universe: The Hubble time, t_H ,which is the inverse of the Hubble constant.

$$T_{\psi,H} = \frac{\langle T\rangle_\psi}{t_H} \tag{71}$$

Using again the Hubble constant presented by the Planck collaboration in [87] yields the following value for the Hubble time:

$$t_H = (14.519 \pm 0.108)\,\mathrm{Gyr} \tag{72}$$

MFP and MAP at the Virial Limit

When $r = r_{\mathrm{vir}}$, $\langle T\rangle_{\psi,\mathrm{vir}}$ given by Equation 57 (which we term the *Virial Annihilation Period*) is generally a Halo-independent parameter which can be equivalently constrained to describe the extent to which the WIMP Annihilation channel has been suppressed, given any set of constraints upon $\langle\sigma v\rangle_\psi$ across a given mass-energy range. The Virial Annihilation Period is, in this way, similar to the annihilation parameter defined in Equation 2 and constrained by Planck in [7].

This is also similar to the manner in which upper bounds on Γ_ψ can be translated to lower bounds on τ_ψ by the simple inverse relation, in order to describe the extent to which the Decay channel is suppressed.

8. The Potential of Multi-Messenger Astronomy

The dawn of multi-messenger astronomy has placed more and more observational targets within the field-of-view of a growing number of telescopes and observatories around the world. Observations are conducted by different telescopes, which utilise a range of astrophysical messengers - from gamma rays to radio waves and neutrinos. If a particular observational target is within the field of view of two or more telescopes, then a comparative multi-messenger analysis can be conducted to determine which telescope infrastructure, in which observational domain, would be best suited for conducting the observation.

We choose two Ultrafaints, Reticulum II and Segue 1, in addition to the Classical Sculptor as fixed observational targets for our multi-messenger analysis. For this analysis, we will only consider the intrinsic WIMP features: The Annihilation Cross-section and Decay Rate, with the WIMP mass as a free parameter. The kinematic analysis of the Mean Free Path and Mean Annihilation Period of the WIMP in the Halo is thus omitted from this section of our analysis.

Segue 1 is within the field-of-view of KM3NeT, CTA and LHAASO, which serves as a point of comparison. Both the Ultrafaint Reticulum II and the Classical dwarf Sculptor are within the field of view of CTA, KM3NeT and the MeerKAT radio telescope array. This will allow for comparison between the projected non-detection constraints imposed upon the parameter space by different telescopes, operating in different observational domains, as well as for a comparison between the potential of Ultrafaint and Classical dwarfs as potential target environments for Dark Matter Indirect detection.

V. Results and Discussion

We consider only the upper error on the $\langle \sigma v \rangle_\psi$ and Γ_ψ non-detection constraints, as these are the only errors relevant to the conservative determination of the upper bounds. Similarly, we consider only the lower error on the $\langle \lambda \rangle_\psi$ and $\langle T \rangle_\psi$ constraints, since we are working with lower bounds in that case. For the analysis of the Mean Free Path and Mean Annihilation Period bounds, we need to consider the relative difference between the bounds imposed at the canonical cross-section and the non-detection bounds in the case of the Milky Way satellite under consideration.

1. LHAASO and CTA

In the gamma ray domain, we consider all six dwarf spheroidals in the case of CTA and the Ultrafaints Segue 1 and Triangulum II in the case of LHAASO.

i Annihilation Cross-Section

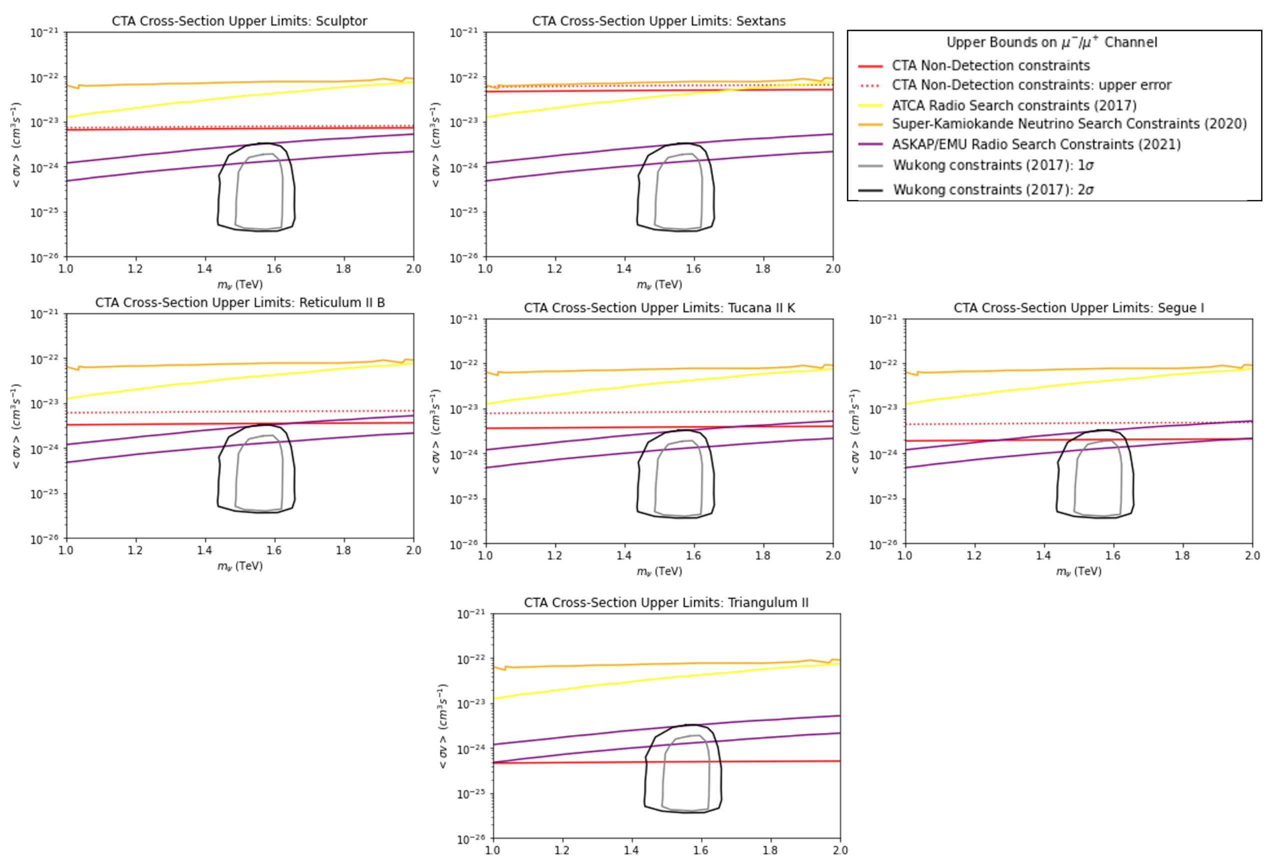

Figure 18: *Projected non-detection $\langle \sigma v \rangle_\psi$ constraints imposed upon the μ^- / μ^+ channel by gamma ray observations of all target dwarf spheroidals using CTA, in comparison to constraints imposed by prior Indirect searches in the radio and neutrino domains [23] [24] [35].*

For CTA, we begin with the comparison presented in Figure 18 between the upper bounds on the muon/anti-muon Annihilation channel imposed by CTA non-detection and constraints placed upon the $\mu^-/\mu+$ channel by prior DM Indirect detection experiments. These are the 2017 ATCA Radio search [23], the 2020 Super-Kamiokande Neutrino search [24] and the 2021 ASKAP/EMU Radio search [35], in addition to the fit to the Wukong flux [21], with the additional constraints as detailed in [20].

Observations of the Classical Sextans yield the least stringent non-detection constraints upon $\langle\sigma v\rangle_\psi$ for the μ^-/μ^+ channel, although the error margins for both Classicals are significantly smaller than the associated errors in the case of the Ultrafaints. In the case of Sextans, the CTA non-detection bounds are similar to those imposed by the 2020 Super-Kamiokande neutrino search [24] and weaker than those imposed by the 2017 ATCA radio search [23] at the lower end of our mass-energy range. For Sculptor observations, CTA non-detection imposes more stringent upper bounds upon the μ^-/μ^+ channel than those imposed by both the ATCA [23] and Super-Kamiokande [24] searches. These bounds are also approximately 10 times stronger than those imposed in the case of Sextans observations. Nonetheless, non-detection in the case of CTA observations of both Classicals yield no novel constraints upon the Wukong parameter space in [20]. The upper bounds imposed by the 2021 ASKAP/EMU search in the LMC [35] are the most stringent of all constraints imposed by the prior Indirect searches considered in this work and the bounds are also stronger than the CTA non-detection bounds for both Classicals across the 1 TeV - 2 TeV mass-energy range.

For all Ultrafaints, CTA non-detection imposes more stringent constraints that those imposed by the ATCA radio search [23] and the Super-Kamiokande neutrino search [24]. Non-detection in the case of Reticulum II B observations impose marginally stronger constraints than is the case with Tucana II K, with the latter case also having a larger associated margin of error. The non-detection constraints imposed by CTA observations of Segue 1 are significantly tighter than those imposed by observations of Reticulum II B and Tucana II K, with constraints being imposed upon the Wukong parameter space in [20] for the $\mu^-/\mu+$ channel, although the relatively large error margin is a factor which must be taken into consideration for this Ultrafaint.

As seen in all plots in Figure 18, the ASKAP/EMU radio search upper bounds [35] impose novel constraints upon the Wukong parameter space in [20]. This is at least in part due to the large J-factor used for the LMC in the ASKAP/EMU search [35]. In comparing these Segue 1 constraints to the bounds imposed by the ASKAP/EMU search [35], we see in Figure 18 that, at the lower end of our mass-energy range, the ASKAP/EMU bounds are significantly tighter than the those imposed by CTA non-detection in the case of Segue 1. At the upper end of our 1 TeV - 2 TeV mass-energy range however, the CTA non-detection bounds begin to converge with those from [35], with both yielding near identical bounds at the 2 TeV boundary.

For Tucana II K and Reticulum II B, we observe a similar trend of the bounds beginning to converge with the ASKAP/EMU constraints, but the ASKAP/EMU bounds in [35] are definitively tighter across more than half of the mass-energy range in comparison to the respective CTA non-detection constraints for these Ultrafaints. Like the case with Segue 1, the disparity between the ASKAP/EMU bounds and the non-detection bounds decreases with increasing-mass energy, but in the case of Reticulum II B and Tucana II K, the constraint curves fail to completely converge and so even at the 2 TeV limit, the bounds in [35] remain more stringent than the non-detection bounds resulting from observations of these two Ultrafaints.

In the special case of the Triangulum II upper bounds, for the μ^-/μ^+ Annihilation channel, we find that CTA non-detection results in more stringent upper bounds upon $\langle \sigma v \rangle_\psi$ than the ASKAP/EMU Indirect radio search in [35], across the mass energy range of 1 TeV - 2 TeV. However, these bounds must be treated with caution, given the lack of good kinematic data sets in the case of Triangulum II [47].

For the purposes of comparing the relative strength of the bounds imposed upon the three Annihilation channels under consideration, we omit the bounds imposed upon the μ^-/μ^+ channel by prior Indirect detection searches in Figure 18 and simply present the CTA non-detection constraints for each of the three leptonic channels, in comparison to the Wukong fit in [20].

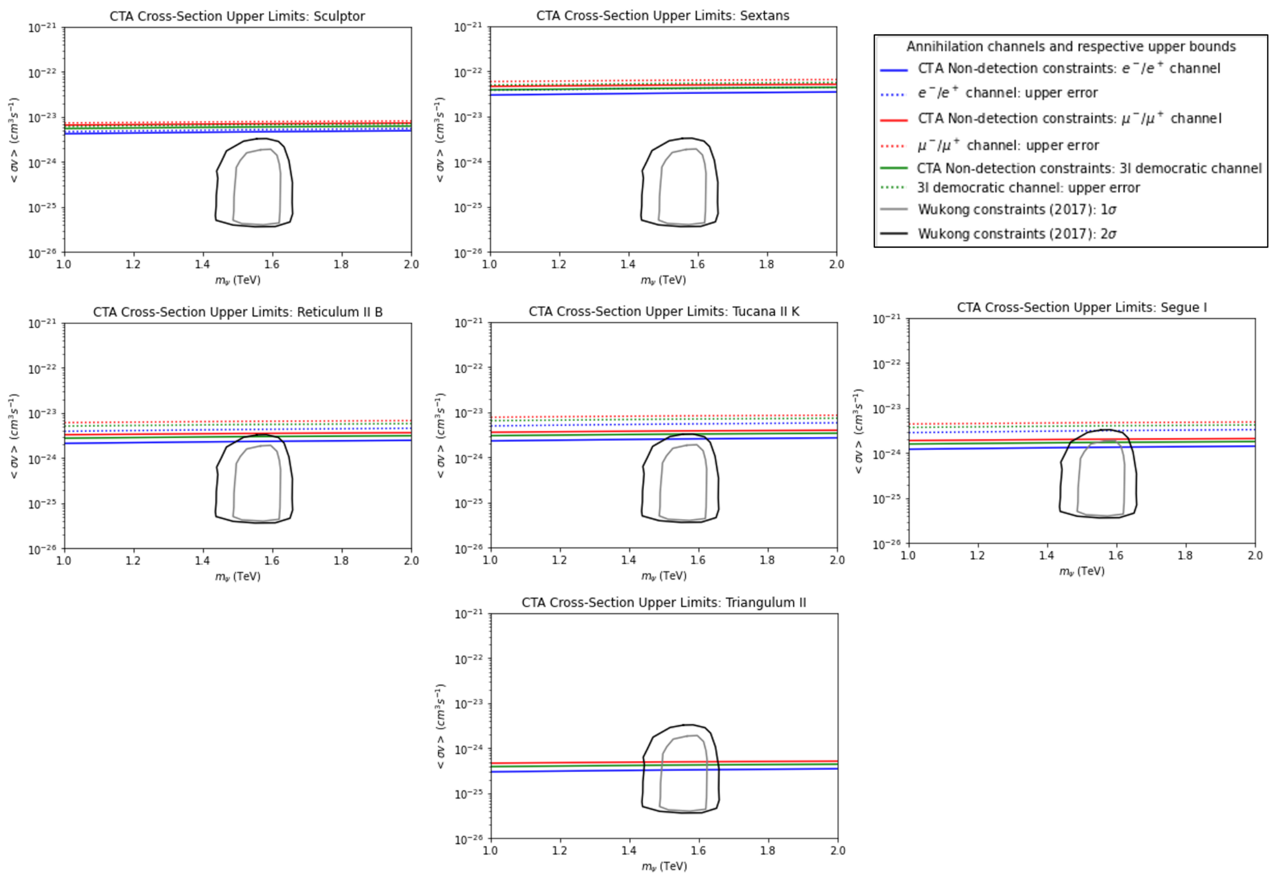

Figure 19: *Projected non-detection $\langle \sigma v \rangle_\psi$ constraints imposed upon all three Leptonic channels by gamma ray observations of all target dwarf spheroidals using CTA.*

For each target dwarf spheroidal, the e^-/e^+ channel is the most tightly constrained, followed by the 3l democratic channel and the μ^-/μ^+ channel in the case of all dwarfs.

Among the target dwarf spheroidals, we see that the weakest $\langle \sigma v \rangle_\psi$ constraints are imposed by gamma ray observations of the Classical dwarf Sextans. For all channels, observations of Sculptor impose significantly more stringent constraints than those imposed in the case of the other Classical dwarf spheroidal. However, across the board, these constraints are still weaker than those imposed in the case of all the Ultrafaint dwarf spheroidals. It nonetheless must be noted that the error margin in the case of the Classical dwarf Sculptor is far smaller than the upper error on the Ultrafaints Reticulum II, Tucana II and Segue 1.

In the case of Tucana II, the constraints imposed are marginally stronger than those imposed by Reticulum II observations, although the error margin is greater as well, with the Tucana II upper error roughly coinciding with the upper limit imposed by Sculptor observations. With the exception of the Triangulum II upper limit constraints, which are generally the tightest but are nonetheless based upon data from an unresolved system [26], the $\langle \sigma v \rangle_{\psi}$ non-detection constraints imposed by observations of the Segue I Ultrafaint are the strongest and thus Segue I is the optimal candidate within our sample as a target object for gamma ray observations using CTA.

Both target dwarf spheroidals within the LHAASO field of view, Segue I and Triangulum II, produced the most stringent non-detection constraints in the case of CTA, although the Triangulum II constraints must be treated with caution on account of the fact that we are working with the upper bound from [26]. In Figure 20, we have LHAASO non-detection constraints upon the μ^-/μ^+ channel in comparison to the established constraints in [23], [24] and [35] in the upper panel and LHAASO non-detection constraints for all channels in the bottom panel.

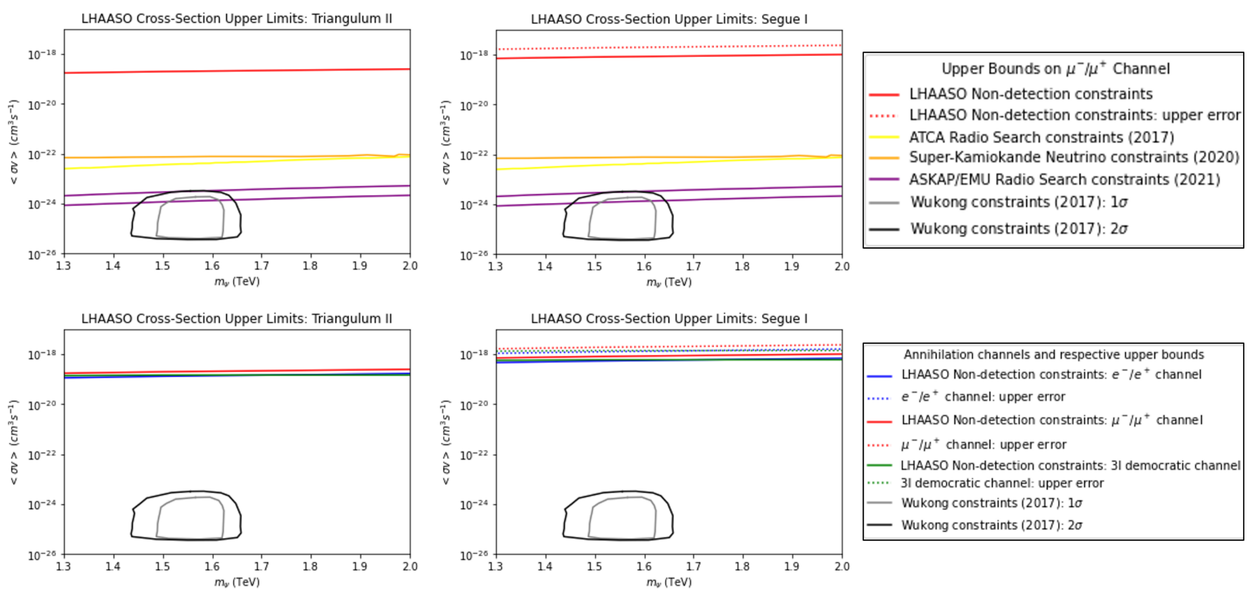

Figure 20: *Projected non-detection $\langle \sigma v \rangle_{\psi}$ non-detection upper bounds imposed by gamma ray observations of Segue I and Triangulum II using LHAASO.*

In the top panel of Figure 20 for Segue 1, the non-detection upper bounds upon the μ^-/μ^+ channel are approximately 2 orders of magnitude weaker than those imposed by the Indirect radio search in Reticulum II [23] and the Indirect neutrino search in the MW Halo and centre [24]. These bounds are also approximately 3 orders of magnitude weaker than those imposed by the ASKAP/EMU radio search in the LMC [35]. While the upper bounds imposed by non-detection in the case of Triangulum II observations are more stringent, they are nonetheless far weaker than the established constraints in [23], [24] and [35].

In the bottom panel of Figure 20, we see that the bounds upon the constraints for the respective channels are tightly clustered in the case of both Ultrafaints, with bounds upon the μ^-/μ^+ channel marginally weaker than those for the e^-/e^+ and 3l democratic channels, where there is significant overlap. For both Ultrafaints, no new constraints are placed upon the Wukong fit in [20] for all Annihilation channels.

ii Decay Rate

In Figure 21, we have the CTA non-detection upper bounds upon the Decay rate for all dwarf spheroidals, in comparison to the non-detection bounds set upon the Leptonic Decay channels by the Fermi IGRB gamma ray search [25].

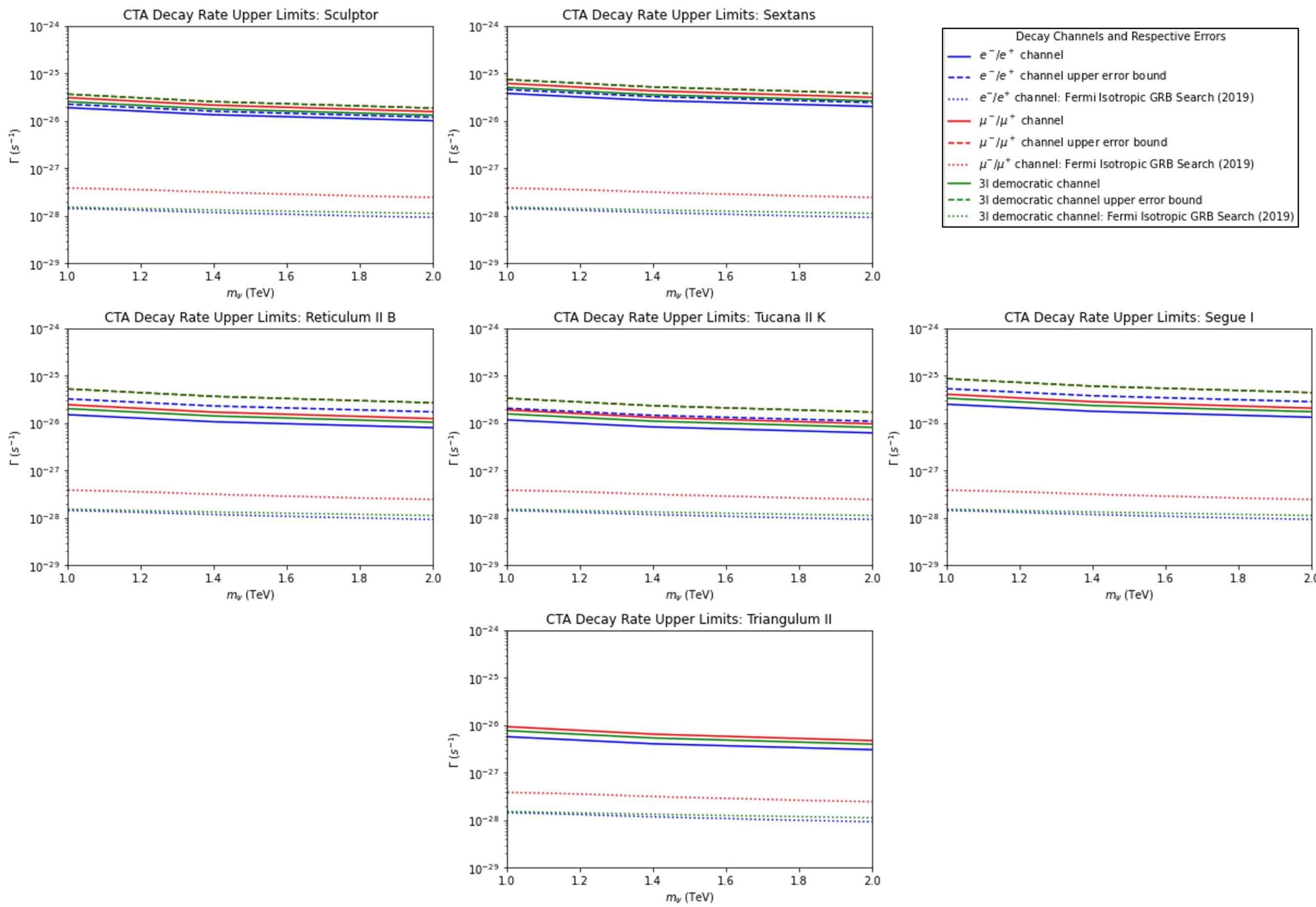

Figure 21: *Non-detection constraints placed upon $\langle\Gamma\rangle_\psi$ by gamma ray observations of all six target dwarf spheroidals using CTA.*

In Figure 21, for all Milky Way satellites, the constraints upon the e^-/e^+ channel are the strongest, followed by the 3l democratic channel and then the $\mu^-/\mu+$ channel, although the differences between the upper bounds placed upon the respective Decay channels are relatively small.

The weakest bounds are imposed through observations of the Classical Sextans, although when the error margin is taken into account, it is comparable to Segue 1 non-detection constraints at the upper error bound. The Ultrafaint Reticulum II B imposes stronger bounds, but the non-detection constraints for the Ultrafaint Tucana II are stronger, with a smaller margin of error. As with the Annihilation case, the most stringent non-detection constraints are yielded in the case of the Triangulum II upper limit. However, even in that special case, the non-detection constraints are one to two orders of magnitude weaker than those set by the Fermi IGRB search [25] Thus, non-detection by CTA for all dwarf galaxies impose no novel bounds upon the MLMP Decay rate, Γ_ψ .

In the case of LHAASO, no constraints can be placed upon the decay rate except at the mass/energy limit of 2 TeV, given that lower energies lie outside the LHAASO sensitivity range. The upper limits imposed upon Γ_ψ (where $m_\psi = 2$ TeV) by LHAASO observations are presented in Table 5.

Dwarf Spheroidal	**Upper limits:** $\log(\Gamma_\psi)$		
	e^-/e^+ channel	μ^-/μ^+ channel	3l democratic channel
Segue I	$-20.43^{+0.33}$	$-20.24^{+0.33}$	$-20.30^{+0.33}$
Triangulum II	-21.07	-20.88	-20.94
Isotropic GRB	-28.03	-27.61	-27.95

Table 5: *Upper limits imposed on Γ_ψ by gamma ray observations with LHAASO, in comparison to constraints imposed from the isotropic GRB in [25]*

We first note that at the upper error bound, the constraints imposed by Triangulum II observations are ~ 1 order of magnitude greater than those imposed by observations of Segue 1, for all Decay channels under consideration. In the case of both the Isotropic GRB constraints in [25] and the projected non-detection constraints for our two target dwarf galaxies, there is a marginal difference between the constraints imposed with respect to different Decay channels, with the e^-/e^+ channel producing the strongest upper limits and the μ^-/μ^+ channel producing the weakest, as was the case for CTA.

For all channels, the upper limits imposed by non-detection in the case of Triangulum II are between 6 and 7 orders of magnitude weaker than those imposed by the Isotropic GRB Search with Fermi in [25]. The LHAASO non-detection upper limits are also significantly weaker than those imposed by CTA observations (at $m_\psi = 2\,TeV$).

iii Mean Free Path and Mean Annihilation Period

1. At the scale radius: $r = r_s$

In Figure 22, we present the non-detection lower bounds are for $\langle\lambda\rangle_\psi$ and $\langle T\rangle_\psi$ upon the Classicals Sextans and Sculptor, along with the constraints in the case of the Triangulum II upper bounds in [26].

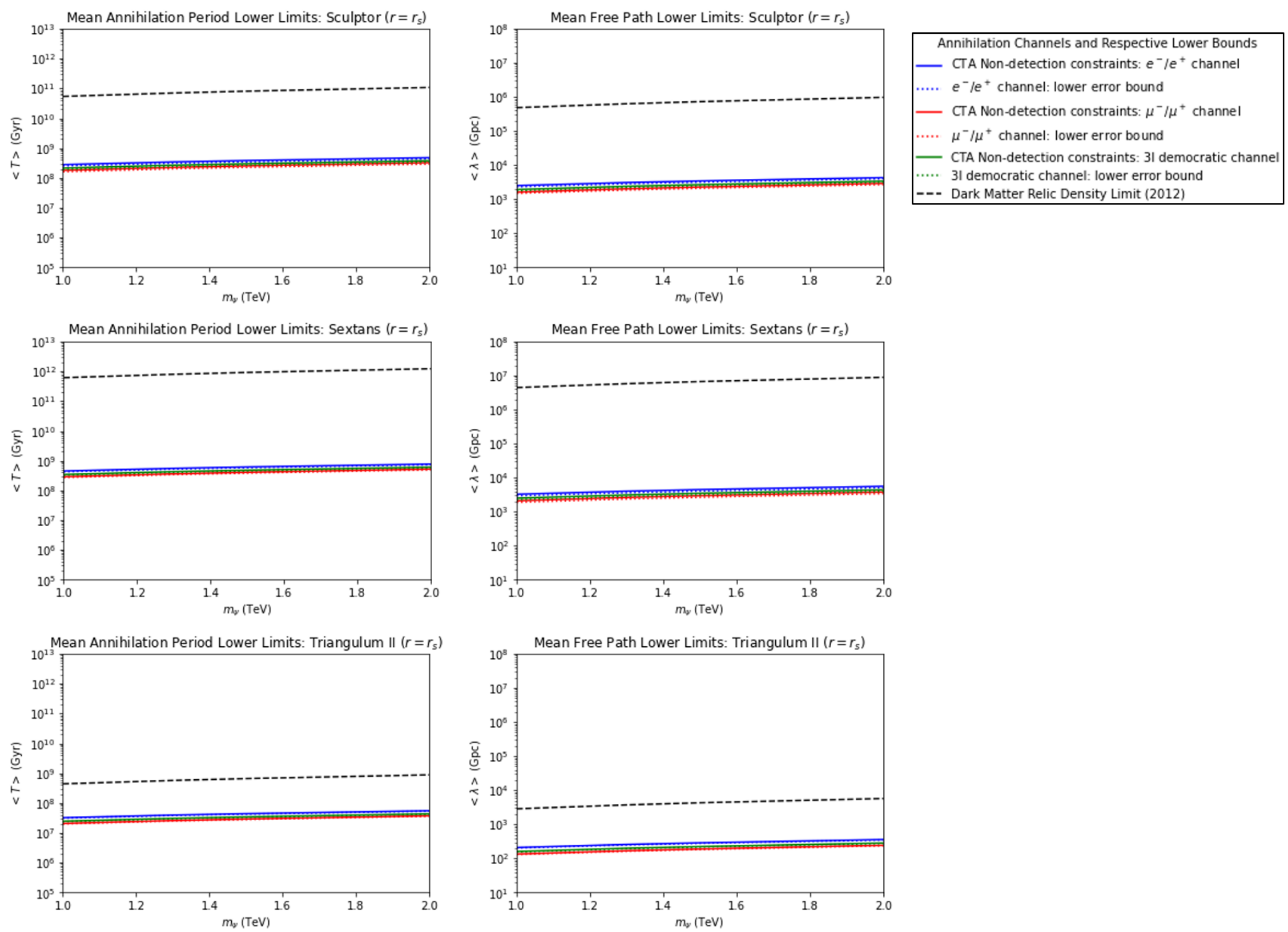

Figure 22: *Non-detection lower placed upon $\langle\lambda\rangle_\psi$ and $\langle T\rangle_\psi$ by gamma ray observations of the two Classicals and the Triangulum II upper bounds presented in [26], with $r = r_s$.*

In Figure 23, the non-detection lower bounds are presented for $\langle\lambda\rangle_\psi$ and $\langle T\rangle_\psi$ for observations of the Ultrafaints Tucana II K, Reticulum II B and Segue 1.

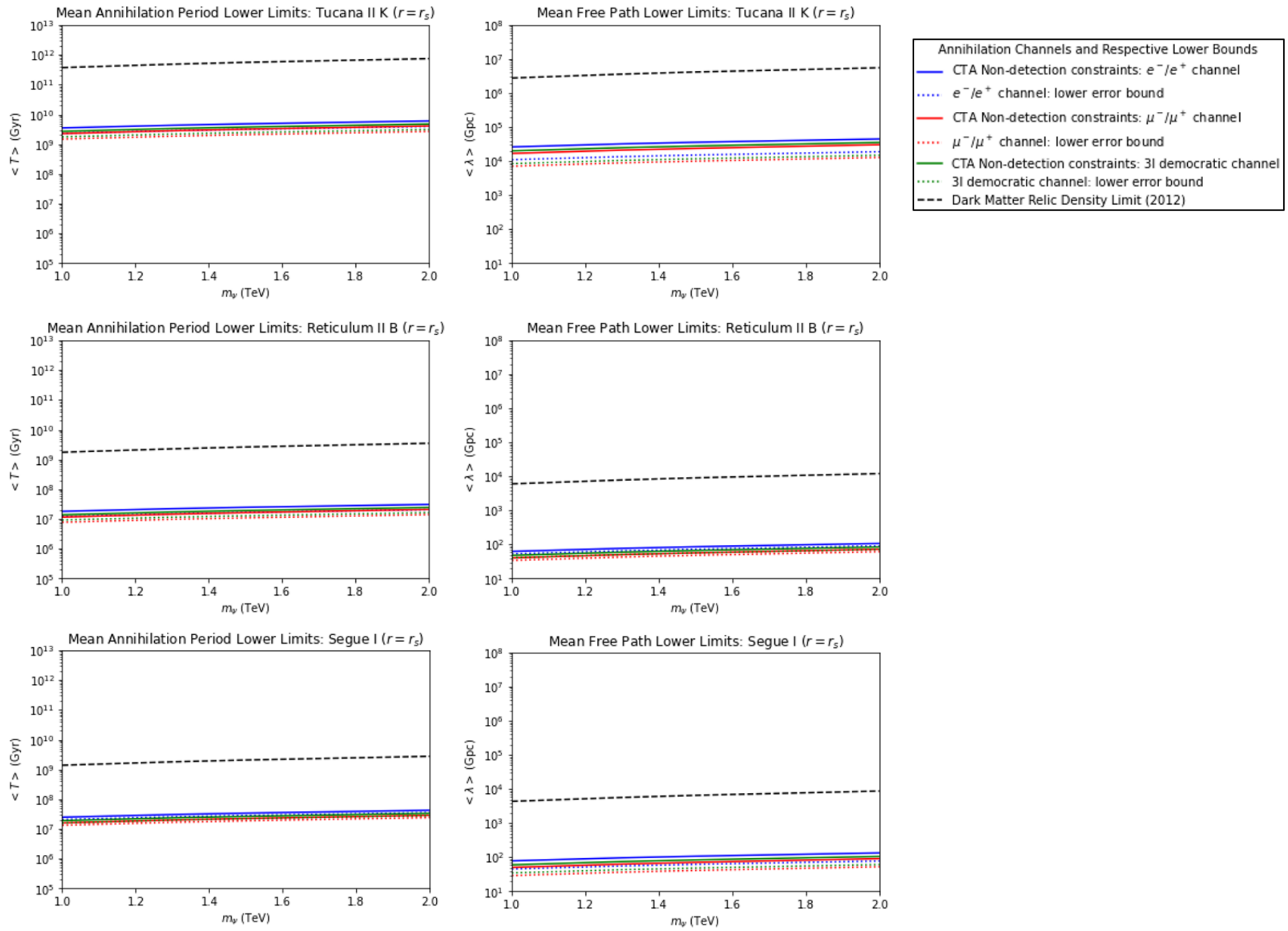

Figure 23: *Non-detection constraints placed upon $\langle\lambda\rangle_\psi$ and $\langle T\rangle_\psi$ by gamma ray observations of the Ultrafaints Tucana II, Reticulum II and Segue 1 by CTA, with $r = r_s$.*

The LHAASO constraints placed upon both $\langle\lambda\rangle_\psi$and $\langle T\rangle_\psi$ are presented in Figure 24.

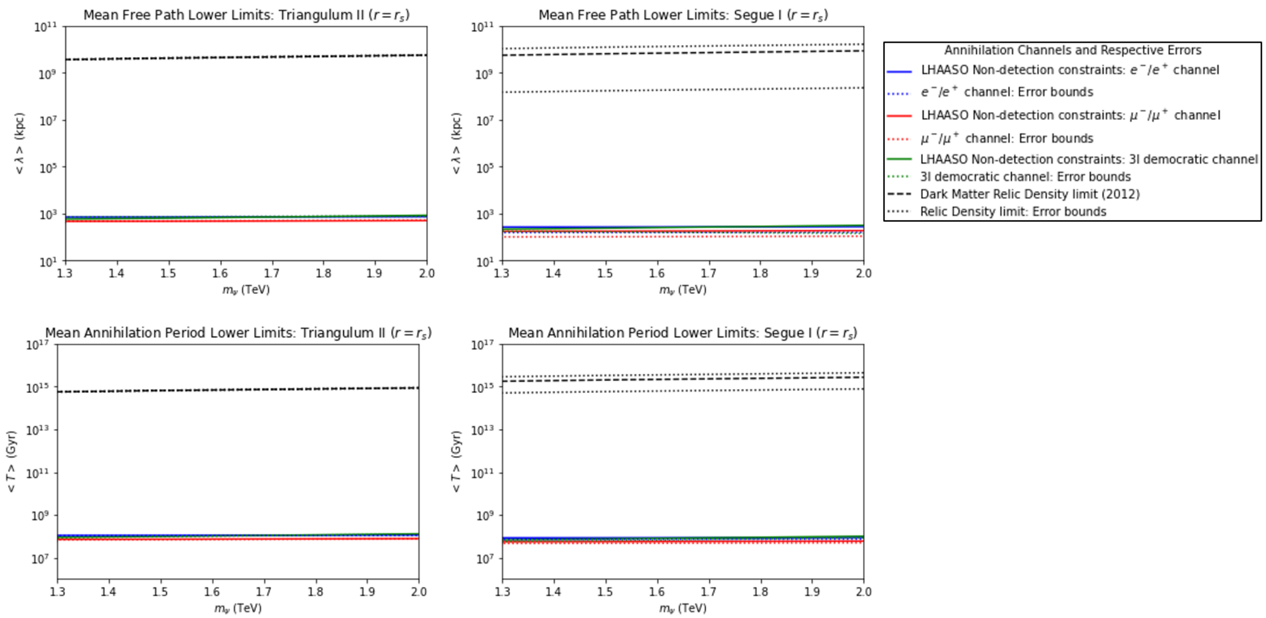

Figure 24: *Constraints placed upon the MLMP mean free path and mean annihilation period by gamma ray observations of Segue I and Triangulum II by LHAASO, $r = r_s$.*

2. At the virial radius: $r = r_{\rm vir}$

The virial boundary non-detection bounds imposed on $\langle \lambda \rangle_\psi$by CTA observations of all dwarf spheroidals are as presented in Figures 26 and 26:

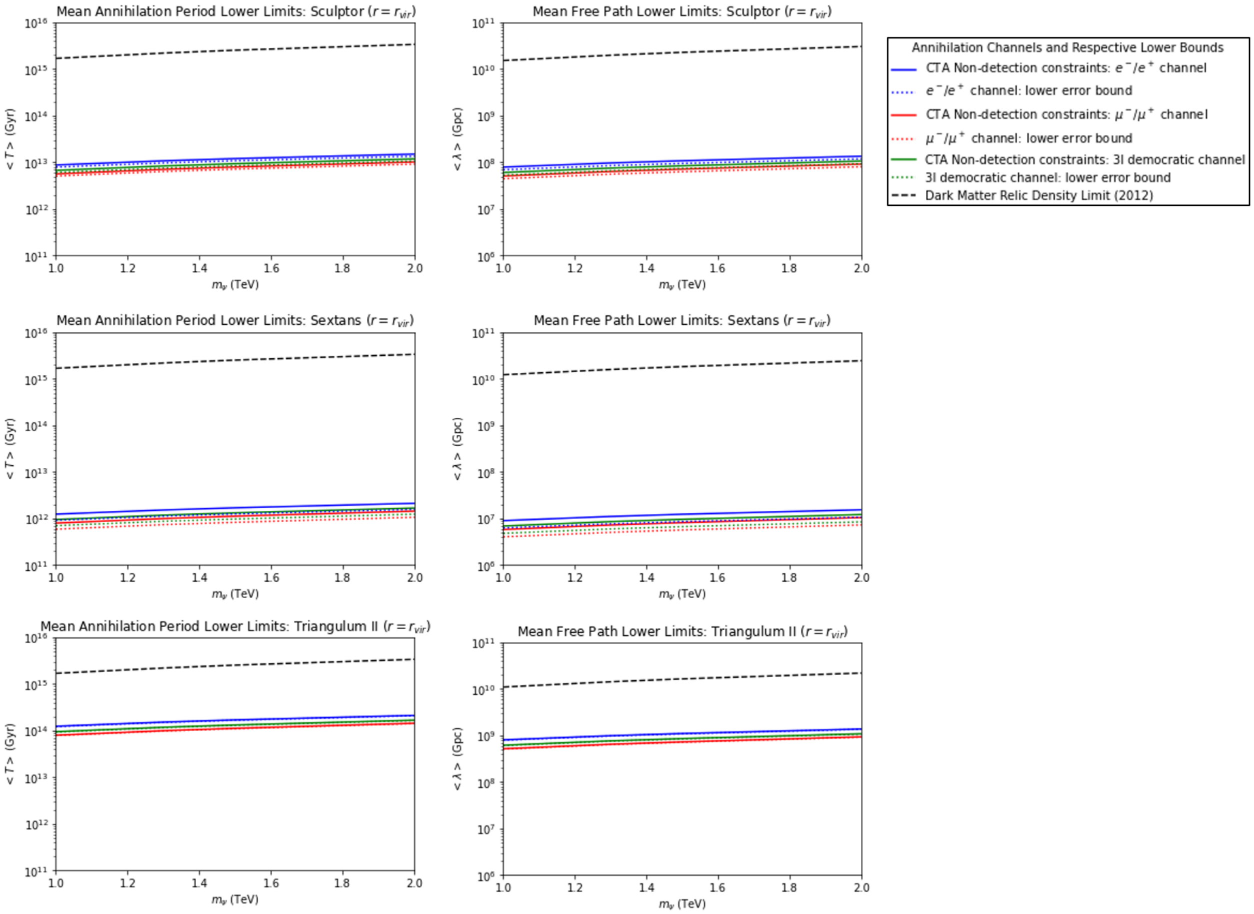

Figure 25: *Lower bounds placed upon the MLMP mean free path by gamma ray observations of all dwarf spheroidal galaxies by CTA, $r = r_{\rm vir}$.*

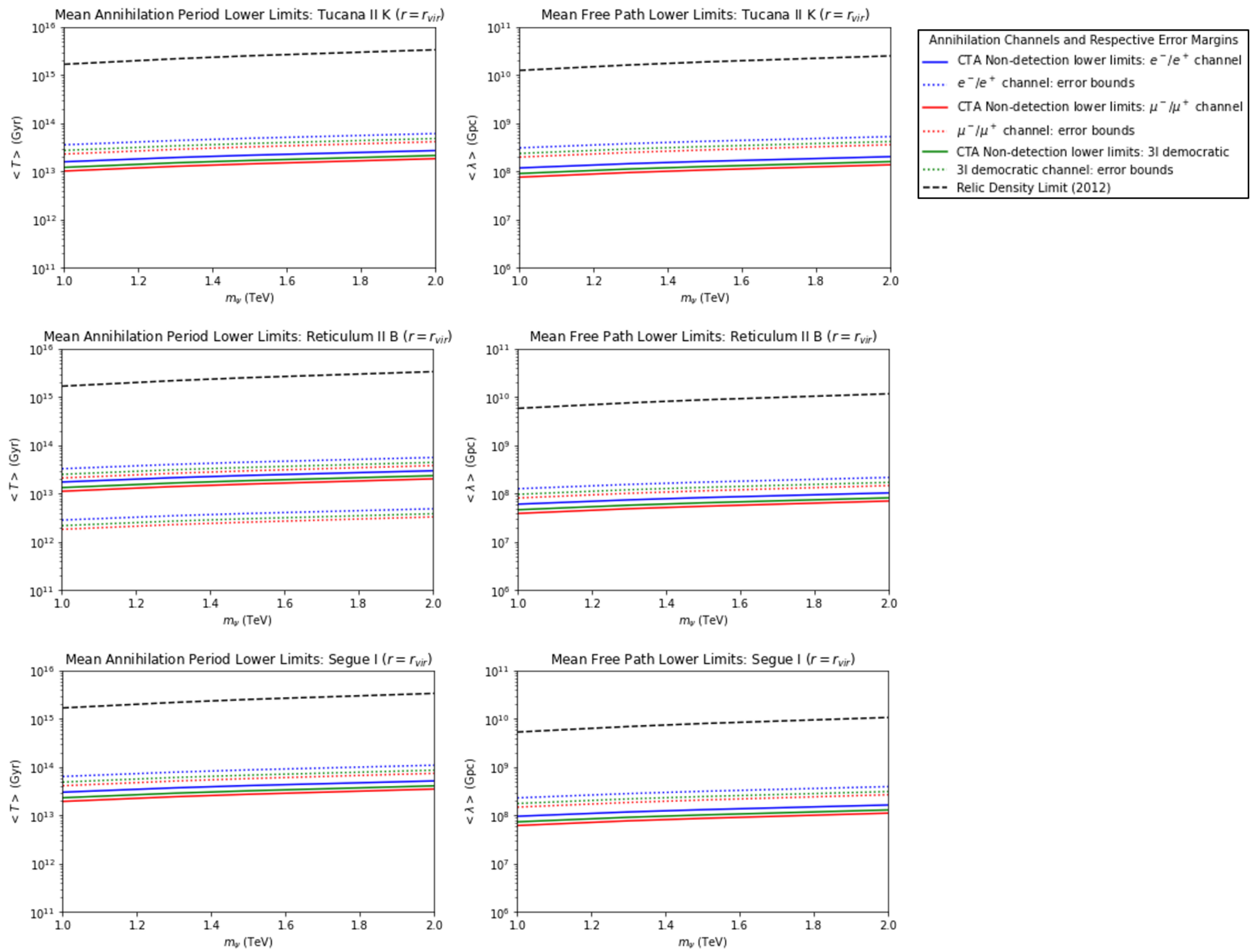

Figure 26: *Lower bounds placed upon the MLMP mean free path by gamma ray observations of all dwarf spheroidal galaxies by CTA*, $r = r_{\text{vir}}$.

Figure 27 presents the non-detection bounds on the MLMP mean free path and mean annihilation period in the case of LHAASO observations.

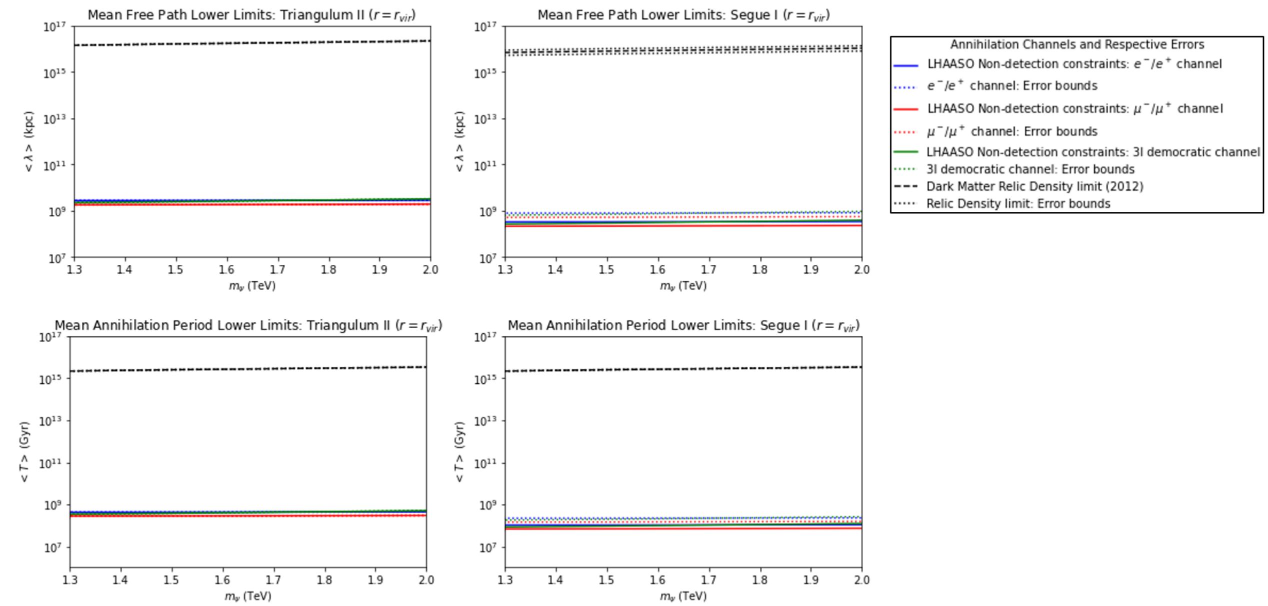

Figure 27: *Constraints placed upon the MLMP mean free path and mean annihilation period by gamma ray observations of Segue I and Triangulum II by LHAASO,* $r = r_{\text{vir}}$.

2. KM3NeT

In the case of KM3NeT, we once again consider all dwarf spheroidals, accounting for neutrino oscillations in each case. We compare the μ^-/μ^+ channel constraints to those imposed by the Super-Kamiokande neutrino search in the MW halo [24], along with those imposed by the ATCA radio search in Reticulum II [23] and the 2021 ASKAP/EMU radio search [35].

i Annihilation Cross Section

In Figure 28, we see that in the case of KM3NeT observations of the Ultrafaints Reticulum II, Tucana II and most significantly Segue I, even at the upper limit, the non-detection constraints imposed upon $\langle \sigma v \rangle_\psi$ in the case of the μ^-/μ^+ channel are more stringent than those imposed by the Kamiokande collaboration in [24]. In all these cases, however, no new constraints are placed upon the DAMPE parameter space as in [20]. In the case of the Triangulum II upper limit for the μ^-/μ^+ channel, novel constraints are placed upon the DAMPE parameter space accounted for here. Thus, for all dwarf spheroidal galaxies, the KM3NeT constraints upon the μ^+/μ^+ are more stringent than those imposed by the Super-Kamiokande search in the Milky Way halo.

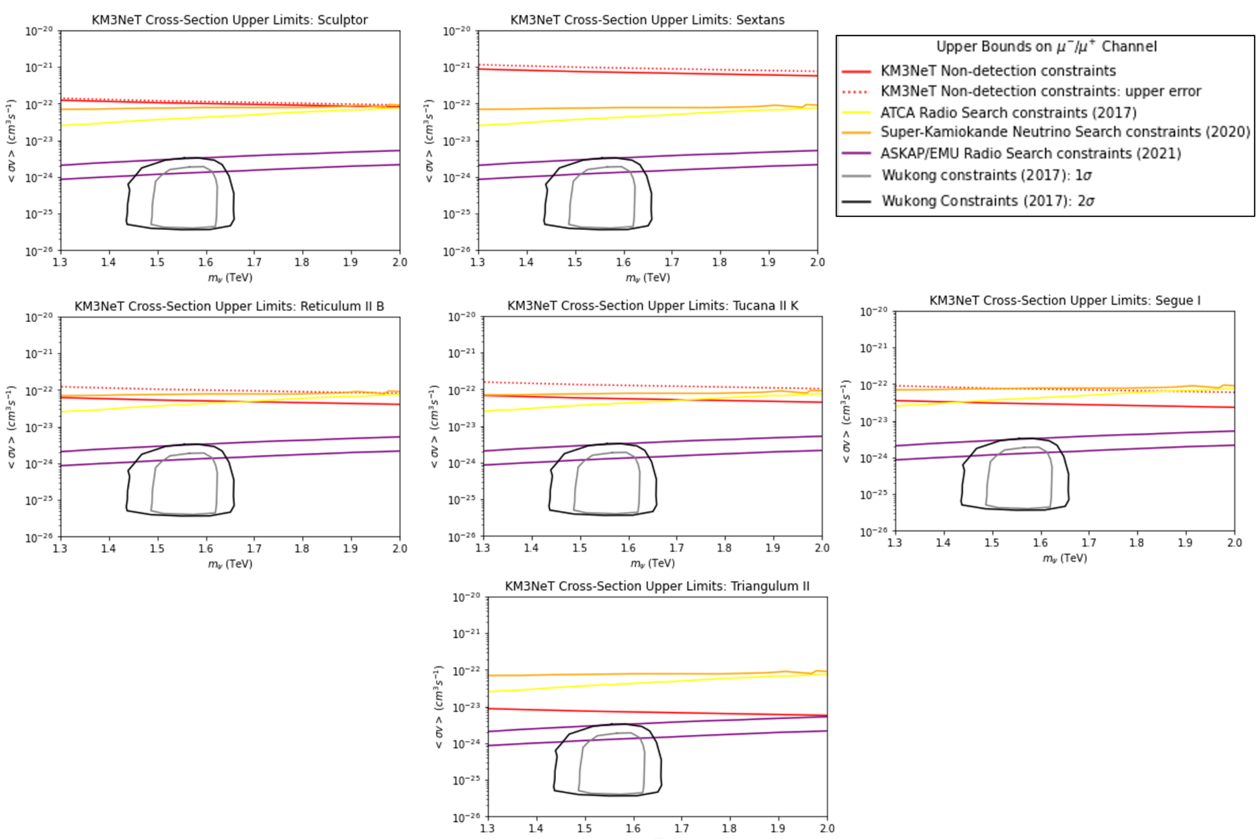

Figure 28: *Non-detection $\langle \sigma v \rangle_\psi$ constraints imposed by muon neutrino observations of all target dwarfs using KM3NeT.*

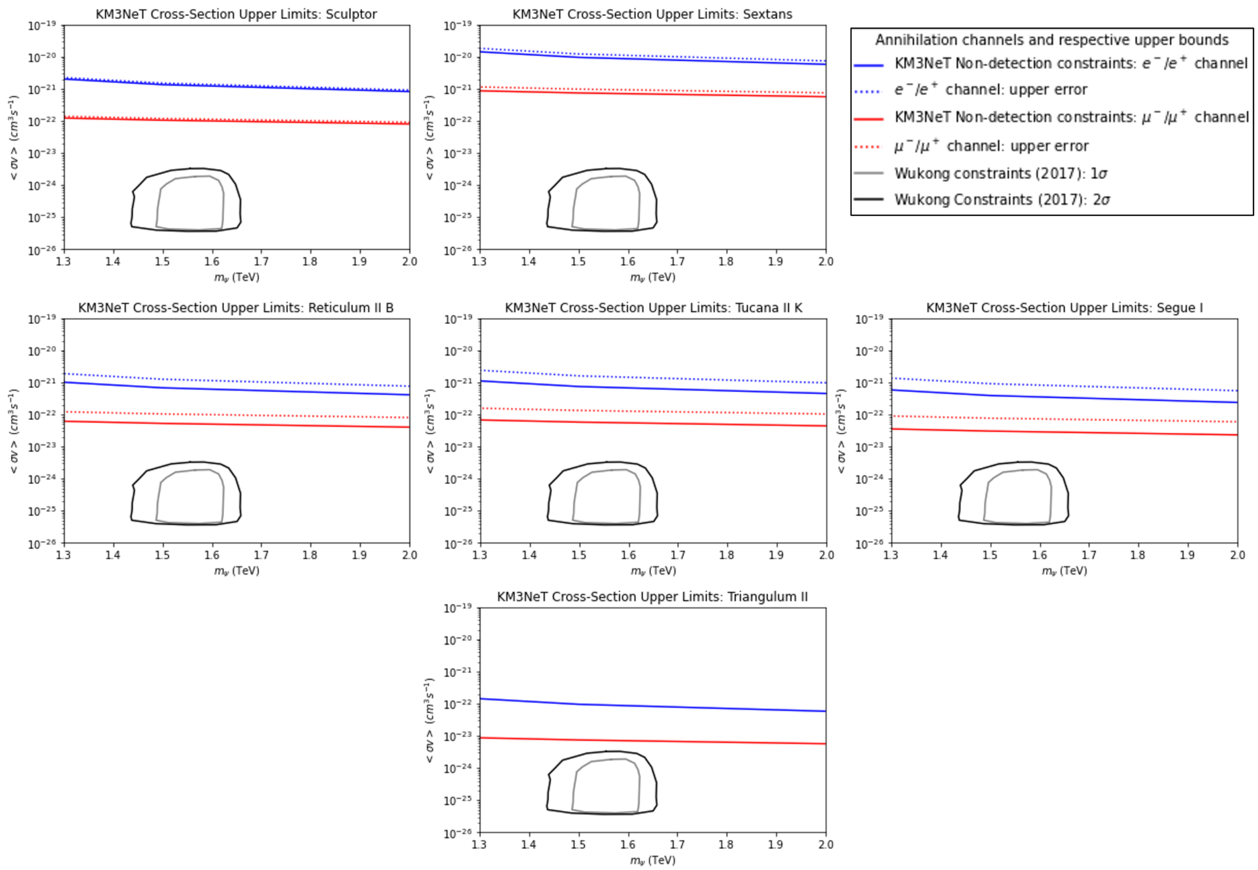

Figure 29: *Non-detection* $\langle \sigma v \rangle_\psi$ *constraints imposed by muon neutrino observations of all target dwarfs using KM3NeT.*

It's noteworthy that for the Classical dwarf Sextans, non-detection bounds in the case of μ^-/μ^+ are weaker than those imposed by the Super-Kamiokande Indirect neutrino search in [24], while the constraints imposed by observations of the Classical Sculptor are similar to those imposed at the upper error-bound in the cases of dwarf spheroidals Tucana II and Reticulum II. Thus, the results illustrated in Figure 28 demonstrate both the increased sensitivity of the KM3NeT detector in comparison to the Kamiokande apparatus, along with the potential of observations of Ultrafaints in comparison to other target environments like Classical dwarfs and the MW halo.

For the radio search in Reticulum II using the ATCA apparatus, we see that the constraints imposed are weaker than those imposed by the Kamiokande neutrino search in [24] and thus weaker than the non-detection constraints by KM3NeT observations of Ultrafaint dwarf spheroidals. In the case of the e^-/e^+ channel, we see that for all six dwarf spheroidals, no novel constraints are placed upon the DAMPE parameter space and the e^-/e^+ constraints are weaker than those imposed in the case of the μ^-/μ^+ channel.

ii Decay Rate

In the case of KM3NeT, no constraints can be placed upon MLMP Decay rate except at the mass/energy limit of 2 TeV, since smaller energies are outside of the KM3NeT sensitivity range. In the case of the e^-/e^+ channel, even at 2 TeV, there is no neutrino yield at the energies within the KM3NeT sensitivity range and so no constraints can be placed upon this decay channel by KM3NeT observations.

Dwarf Spheroidal	**Upper limits:** $\log(\Gamma_\psi)$	
	μ^-/μ^+ channel	3l democratic channel
Segue I	$-24.18^{+0.33}$	$-24.01^{+0.33}$
Tucana II K	$-24.51^{+0.25}$	$-24.34^{+0.25}$
Reticulum II B	$-24.40^{+0.33}$	$-24.23^{+0.33}$
Sculptor	$-24.30^{+0.07}$	$-24.13^{+0.07}$
Sextans	$-24.00^{+0.08}$	$-23.83^{+0.08}$
Triangulum II	-24.82	-24.65
Isotropic GRB	**-27.61**	**-27.95**

Table 6: *Upper limits imposed on Γ_ψ by muon neutrino observations with KM3NeT, in comparison to constraints imposed by the Isotropic GRB in [25]*

Of the two Classicals, both of which have notably smaller error margins than their Ultrafaint counterparts, Sculptor observations place more stringent non-detection constraints upon the MLMP Decay rate than observations of Sextans by KM3NeT. For the the Ultrafaints, excluding Triangulum II, the most stringent constraints are imposed by observations of Tucana II, in the case of both Decay Channels. Among these Ultrafaints, the weakest non-detection constraints are imposed by observations of Segue I, where the (weaker) bounds at the upper error are roughly equivalent to the bounds at the upper error for Sextans, a Classical dwarf, owing to the larger margin of error in the case of the Ultrafaints like Segue I.

It is noteworthy that when error margins are taken into consideration, the Classical dwarf Sculptor is as worthy a candidate for an observational target as Tucana II, as it would produce a more precise result. As expected, the upper limit for Triangulum II yield the most stringent constraints, but nonetheless, these constraints are more than two orders of magnitude weaker than those imposed by the IGRB search in the case of the $\mu^-/\mu+$ Decay channel and more than three orders of magnitude weaker for the 3l democratic channel.

Thus, for all Decay channels and observations of all dwarf galaxies, no novel constraints can be placed upon the Decay rate upper limit by neutrino observations with KM3NeT.

iii Mean Free Path and Mean Annihilation Period

1. At the scale radius Halo boundary: $r = r_s$

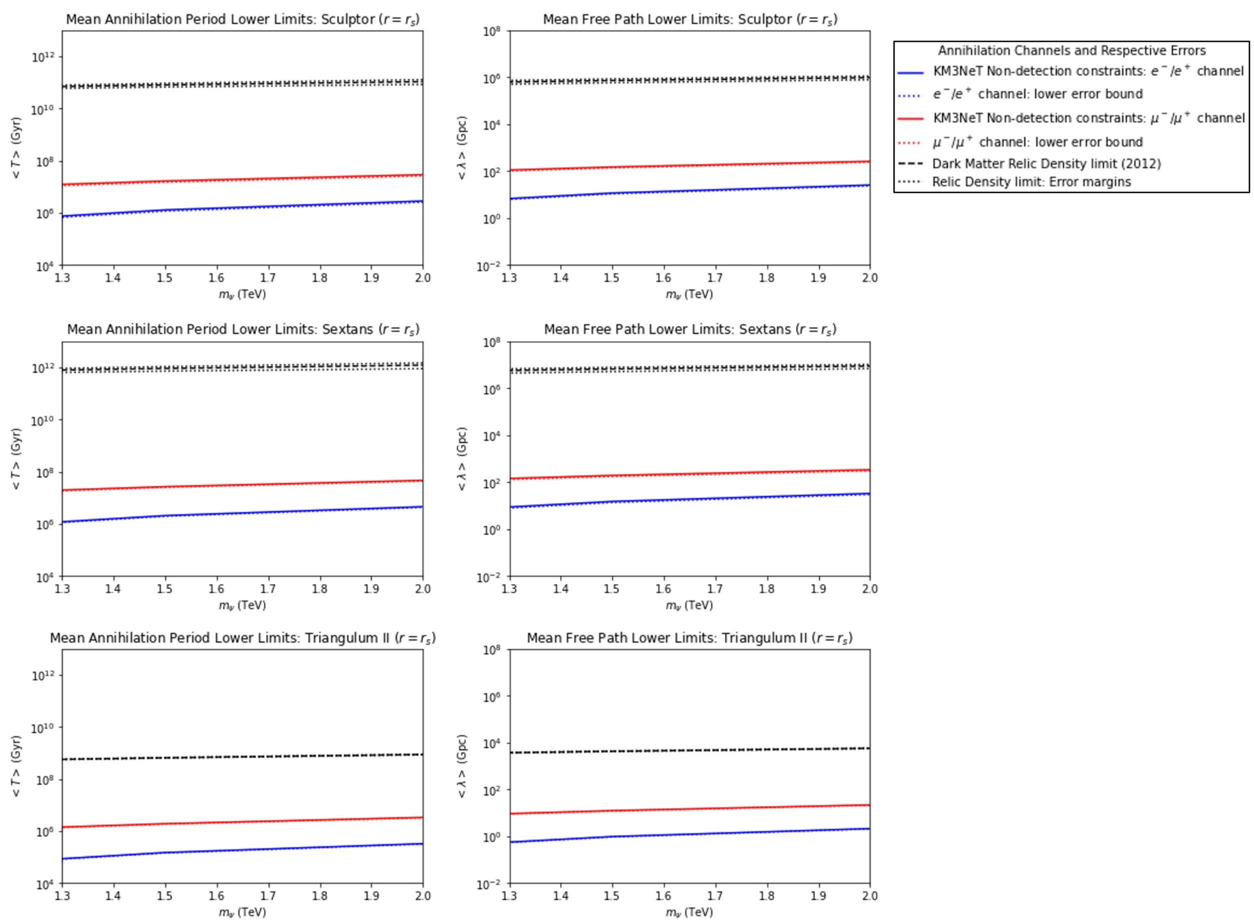

Figure 30: *Constraints placed upon* $\langle\lambda\rangle_\psi$ *by muon neutrino observations of dwarf spheroidal galaxies by KM3NeT,* $r = r_s$.

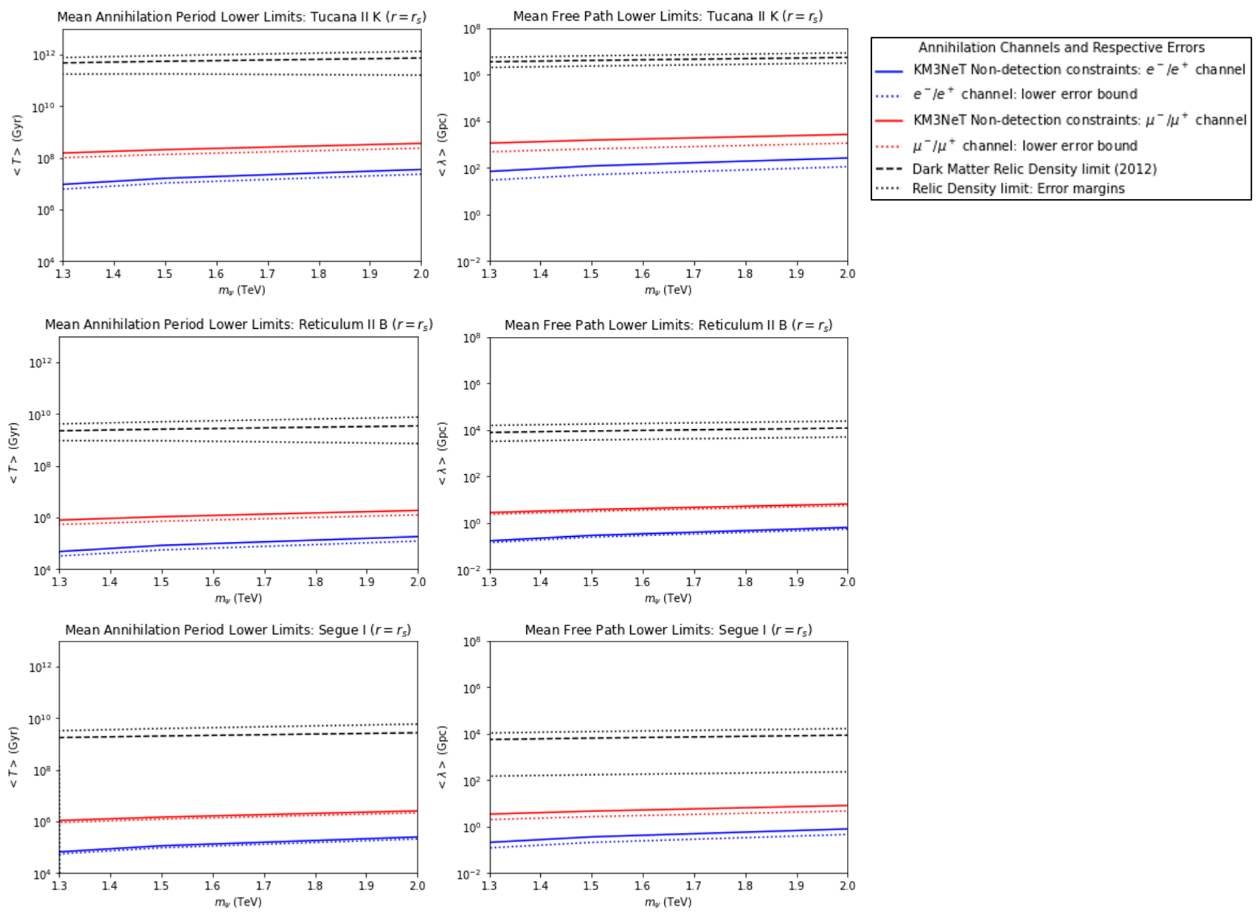

Figure 31: *Constraints placed upon $\langle\lambda\rangle_\psi$ by muon neutrino observations of dwarf spheroidal galaxies by KM3NeT, $r = r_s$.*

2. At the virial radius Halo boundary: $r = r_{\text{vir}}$

At the virial radius Halo boundary, the lower bounds on both MFP and MAP are presented in Figures 32 and 33.

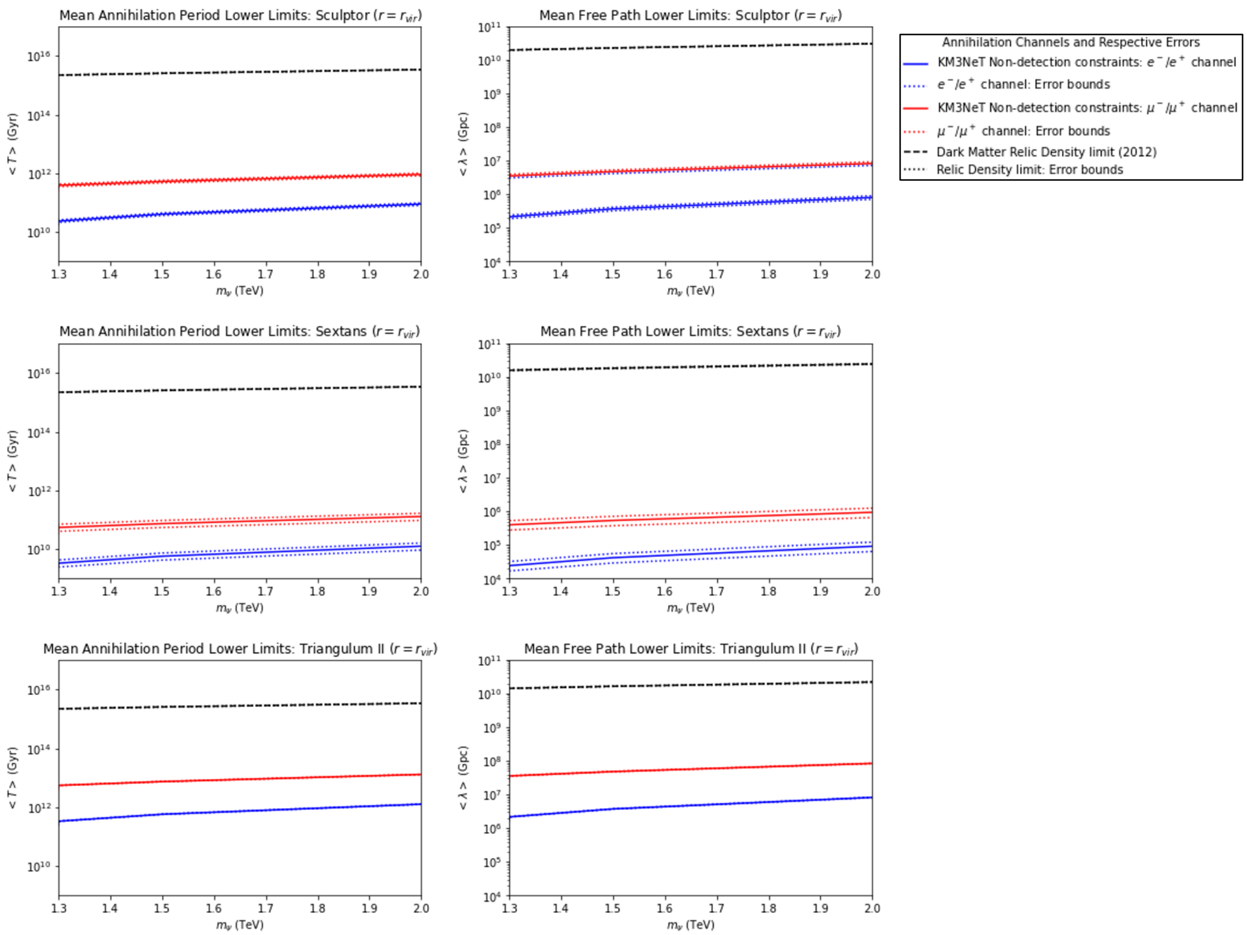

Figure 32: *Non-detection constraints placed upon $\langle\lambda\rangle_\psi$ by muon neutrino observations of dwarf spheroidal galaxies by KM3NeT, $r = r_{\rm vir}$.*

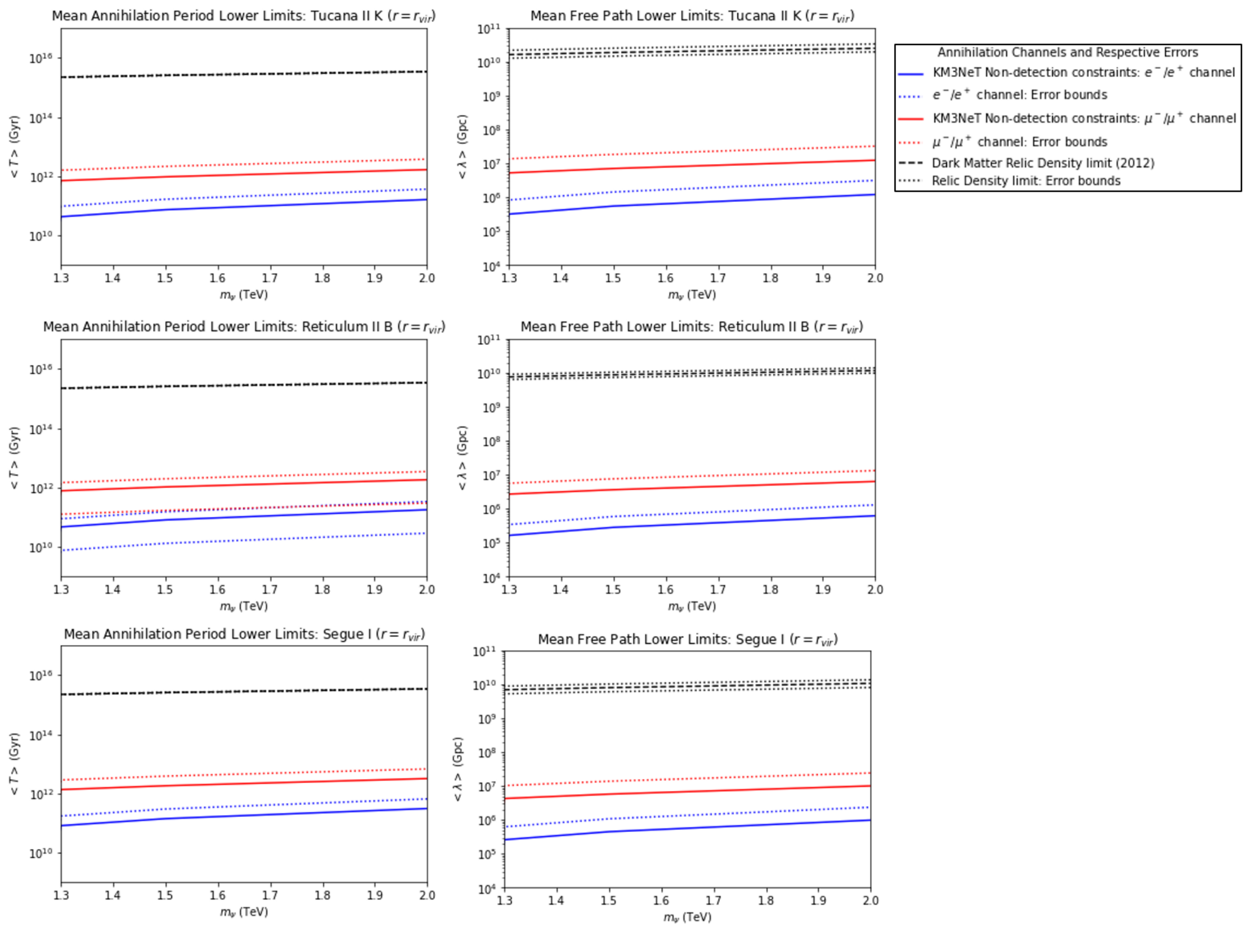

Figure 33: *Constraints placed upon $\langle \lambda \rangle_\psi$ by muon neutrino observations of dwarf spheroidal galaxies by KM3NeT, $r = r_{\text{vir}}$.*

3. MeerKAT

In the case of MeerKAT, we consider the Ultrafaint Reticulum II, along with the Classicals Sextans and Sculptor, for an observation time of 20 hours.

i Annihilation Cross Section

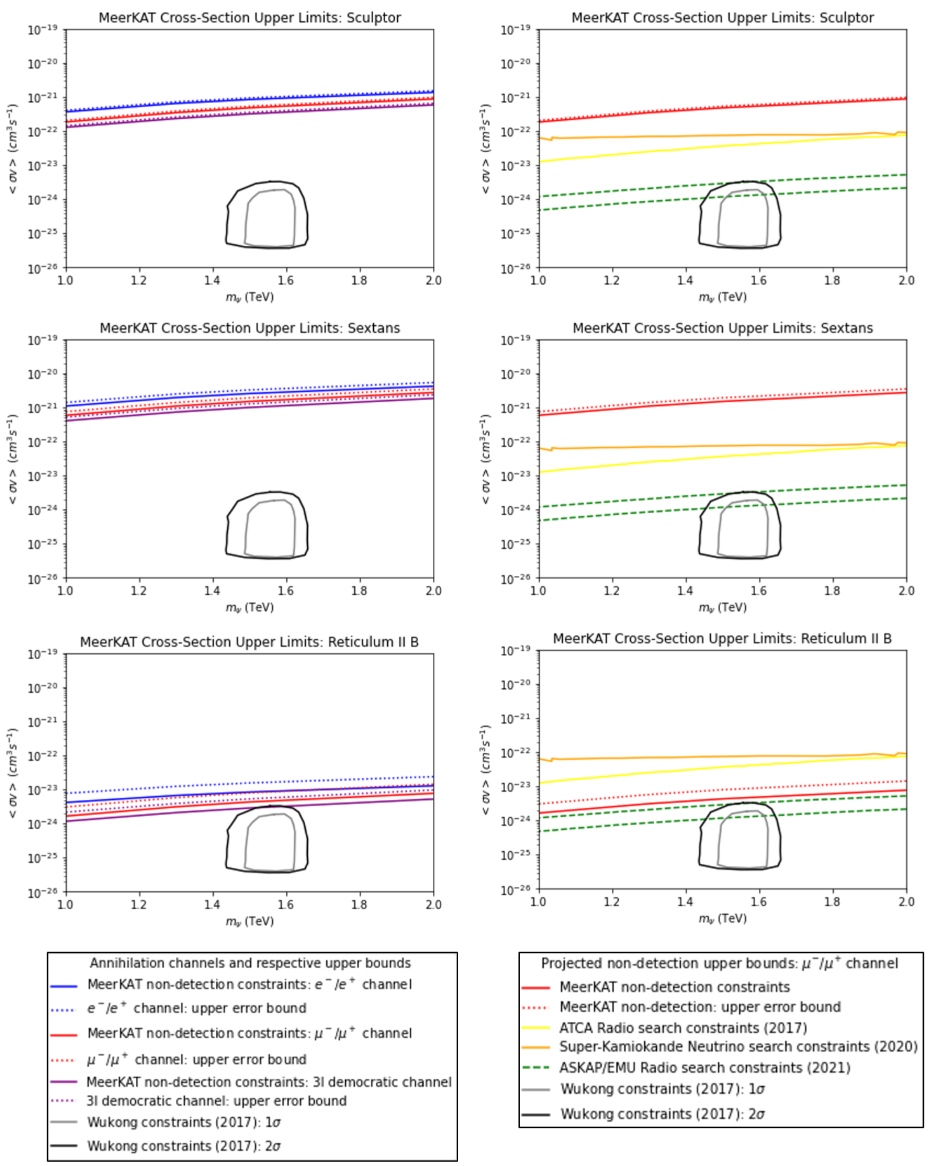

Figure 34: *Projected non-detection $\langle \sigma v \rangle_\psi$ upper bounds imposed by radio observations of Reticulum II, Sculptor and Sextans using MeerKAT, with the left panel displaying non-detection bounds for all three Leptonic channels and the right panel comparing the MeerKAT non-detection bounds upon the μ^-/μ^+ channel to the prior bounds in [23], [24] and [35].*

In the left panel of Figure 34, we see that for all three dwarf spheroidals, the most stringent upper bounds are placed upon the 3l democratic channel, followed by the μ^-/μ^+ channel and the e^-/e^+ channel.

For all Annihilation channels, the least stringent non-detection constraints are from MeerKAT observations of Sextans, followed by observations of the other Classical dwarf, Sculptor. The Reticulum II B non-detection upper bounds are the strongest, albeit with a larger margin of error.

For the μ^-/μ^+ Annihilation channel, the MeerKAT non-detection constraints are stronger than those imposed by the Super-Kamiokande neutrino search [24] and the ATCA radio search [23]. The MeerKAT non-detection upper bounds are competitive with the ASKAP/EMU constraints [35].

ii Decay Rate

The MeerKAT Decay rate upper bounds for Segue 1 and Sculptor will be discussed under the chapter on the multi-messenger analysis.

iii Mean Free Path and Mean Annihilation Period

1. At the scale radius: $r = r_s$

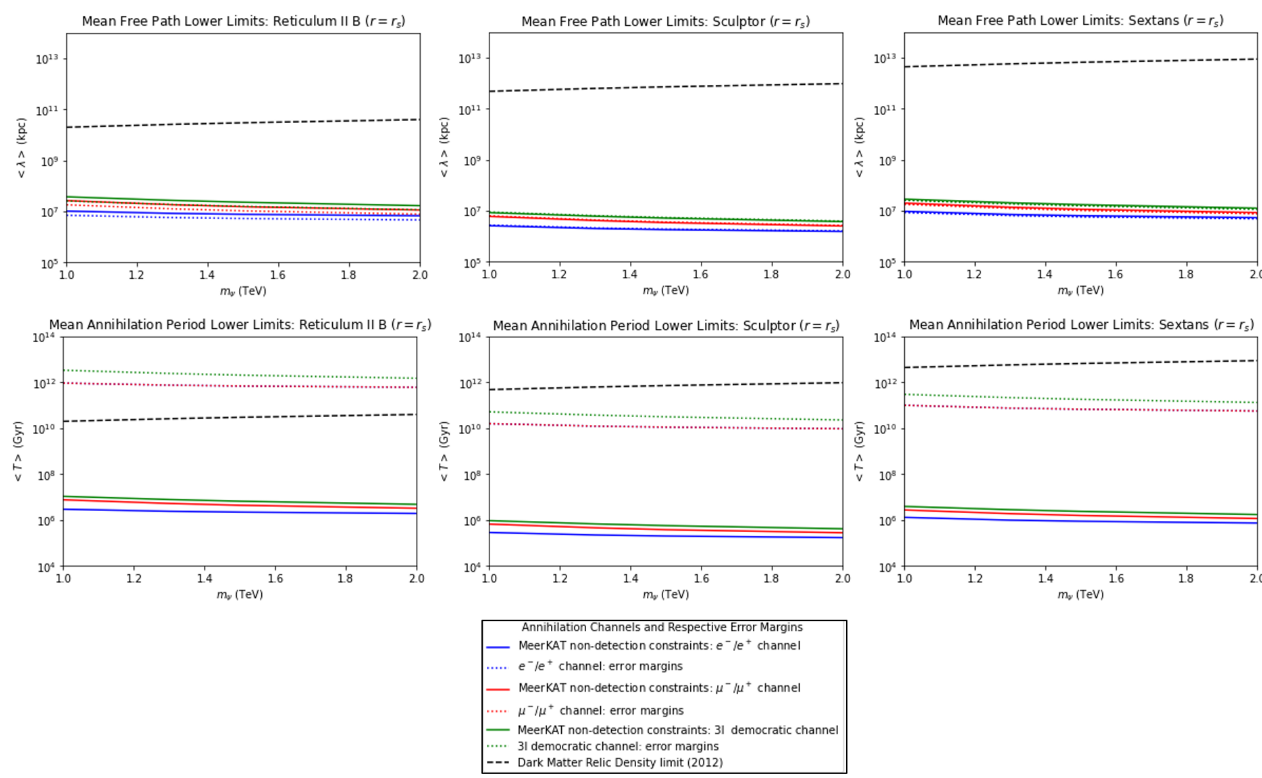

Figure 35: *Projected non-detection constraints imposed upon $\langle \lambda \rangle_\psi$ and $\langle T \rangle_\psi$ by radio observations of Reticulum II, Sculptor and Sextans using MeerKAT, where $r = r_s$.*

2. At the virial radius: $r = r_{\text{vir}}$

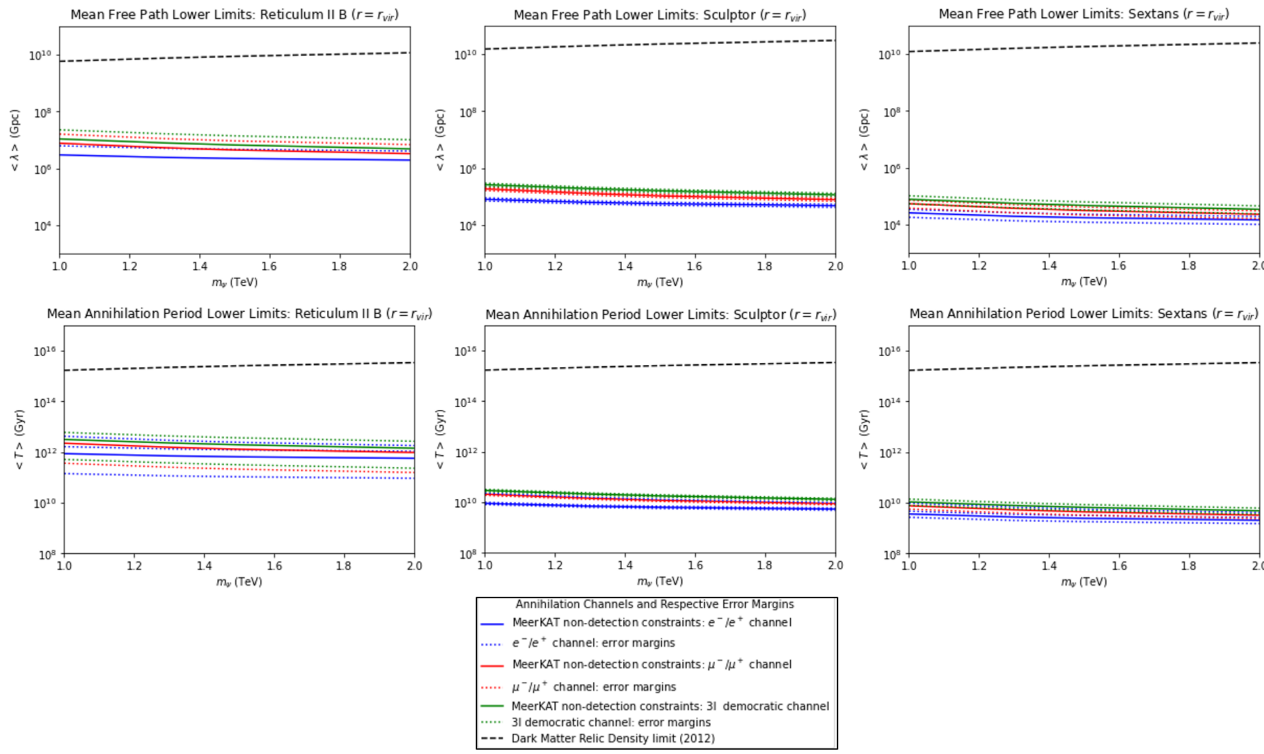

Figure 36: *Projected non-detection constraints imposed upon $\langle \lambda \rangle_\psi$ and $\langle T \rangle_\psi$ by radio observations of Reticulum II, Sculptor and Sextans using MeerKAT, where $r = r_{\text{vir}}$.*

4. Analysis of MFP and MAP Results

For this analysis, we have fixed the WIMP Annihilation cross-section to the DM Relic density limit of $\langle \sigma v \rangle_{\psi} = 2.2 \times 10^{-26} \mathrm{cm}^3 \mathrm{s}^{-1}$ calculated in [42]. In Figure 37, we present the Mean Free Path and Mean Annihilation Period lower limits for both Classicals, along with the Ultrafaint Reticulum II, at the scale radius and virial radius respectively. $\langle \lambda \rangle_{\psi}$ and $\langle T \rangle_{\psi}$ are respectively written as multiples of d_H , the Hubble distance and t_H ,the Hubble time.

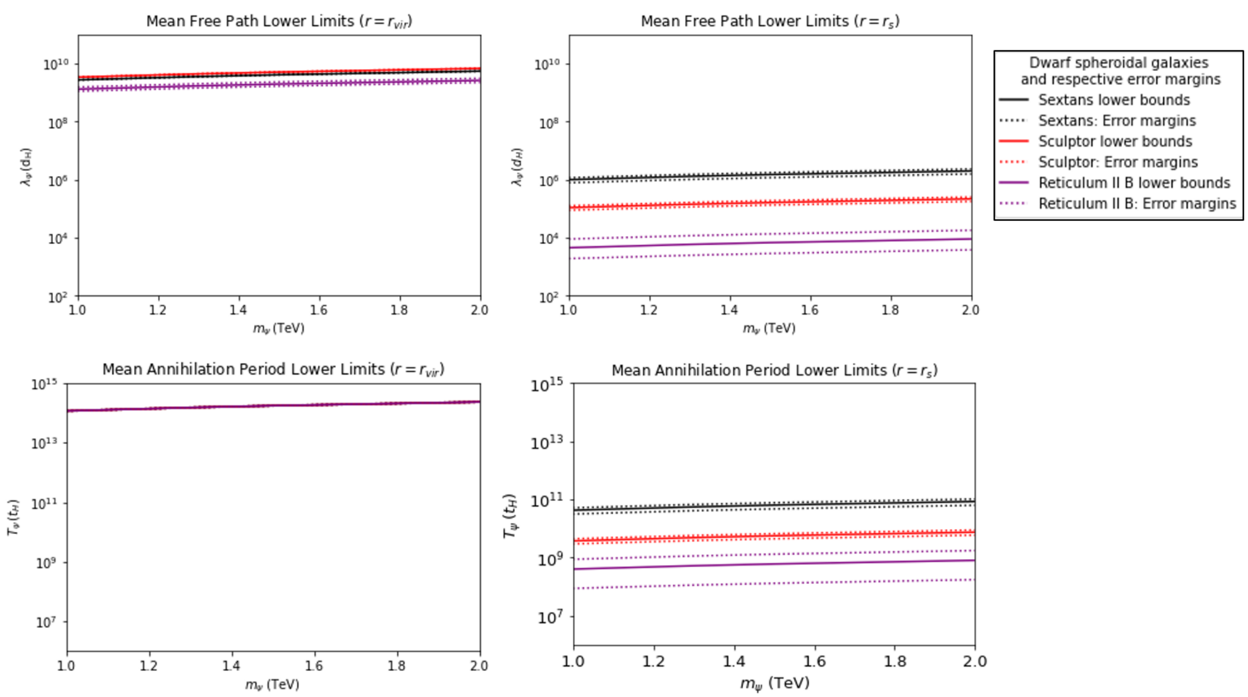

Figure 37: *The respective $\langle \lambda \rangle_{\psi}$ and $\langle T \rangle_{\psi}$ lower bounds for TeV WIMPs in Reticulum II, Sculptor and Sextans, as a multiple of d_H and t_H , for Halo boundaries at $r = r_s$ and $r = r_{\text{vir}}$ respectively.*

With the Halo boundary set to the scale radius, there are significant differences between the WIMP Mean Free Path limits in the case of the three dwarf spheroidals. In the top right panel of Figure 37, we see that the highest $\langle \lambda \rangle_{\psi}$ bounds are imposed in the case of Sextans, followed by Sculptor, the other Classical dwarf. The limits calculated in the case of the Ultrafaint Reticulum II are significantly lower than those for the Classicals, in addition to the fact that the Reticulum II limits have a broader error margin. The Mean Annihilation Period results in the bottom right panel follow a similar trend at the scale radius boundary. Consider that, at the scale radius, from Equations 52 and 54 , we have the following proportionality:

$$\langle \lambda \rangle_{\psi}, \langle T \rangle_{\psi} \propto \frac{r_s^3}{D_L^2} \tag{73}$$

While the two Classicals are at a greater luminosity distance in comparison to the Ultrafaint Reticulum II, the relative distance between their scale radii is larger. Hence, the higher limits yielded for the Classicals at the scale radius are sensible.

In the top left panel of Figure 37, we see that the lower limits for the respective dwarf spheroidals are more tightly clustered together, with the two Classical dwarfs yielding almost identical limits, which are larger than those imposed in the case of Reticulum II, but by a smaller margin than was the case at the scale radius boundary. This is sensible, since the the only variable characterising each dwarf spheroidal is the line-of-sight velocity dispersion, σ_{los} . These bounds on $\langle\lambda\rangle_{\psi}$ at the virial radius are more than 9 orders of magnitude greater than the Hubble distance, d_H.

In the bottom left panel of Figure 37, we see that the Mean Annihilation Period of the three dwarfs under consideration is constant at the virial radius Halo boundary. Thus, within our mass/energy range, bounds on $\langle T\rangle_{\psi,\text{vir}}$, the Virial Annihilation Period, are approximately 14 orders of magnitude greater than the age of the universe. With the Annihilation cross-section set to the Thermal Relic cross-section, as we have time, the Virial Annihilation Period is an absolute bound - that is, if the WIMP model under consideration produces a Mean Annihilation Period within the virial radius of any Halo which exceeds our calculated bound, then that model cannot account for the Dark Matter Relic Density.

As a point of comparison, the lower bounds imposed upon the WIMP mean liftetime, τ_{ψ} ,by the 2019 Indirect search using Fermi are approximately 10-11 orders of magnitude greater than the Hubble time [25].

5. Multi-messenger Analysis

For the multi-messenger analysis, we consider the Classical Sculptor, along with the Ultrafaints Segue 1 and Reticulum II. Each of the three are within the fields of view of at least 3 of the 4 multi-messenger telescopes under consideration in this work.

i Segue 1

We impose non-detection upper bounds on $\langle\sigma v\rangle_{\psi}$ from observations of the Ultrafaint dwarf Segue 1, utilising CTA and LHAASO in the gamma ray domain and KM3NeT in the neutrino domain. These projected multi-messenger non-detection bounds are compared to the same established non-detection bounds in [23], [35] and [24] as before, along with constraints accounted for in the parameter space fit to the detection of the Wukong excess flux in [21], as presented in [20] and reproduced in Figure 12.

In Figure 38, the non-detection upper bounds for Segue 1 are presented separately for each respective Annihilation channel.

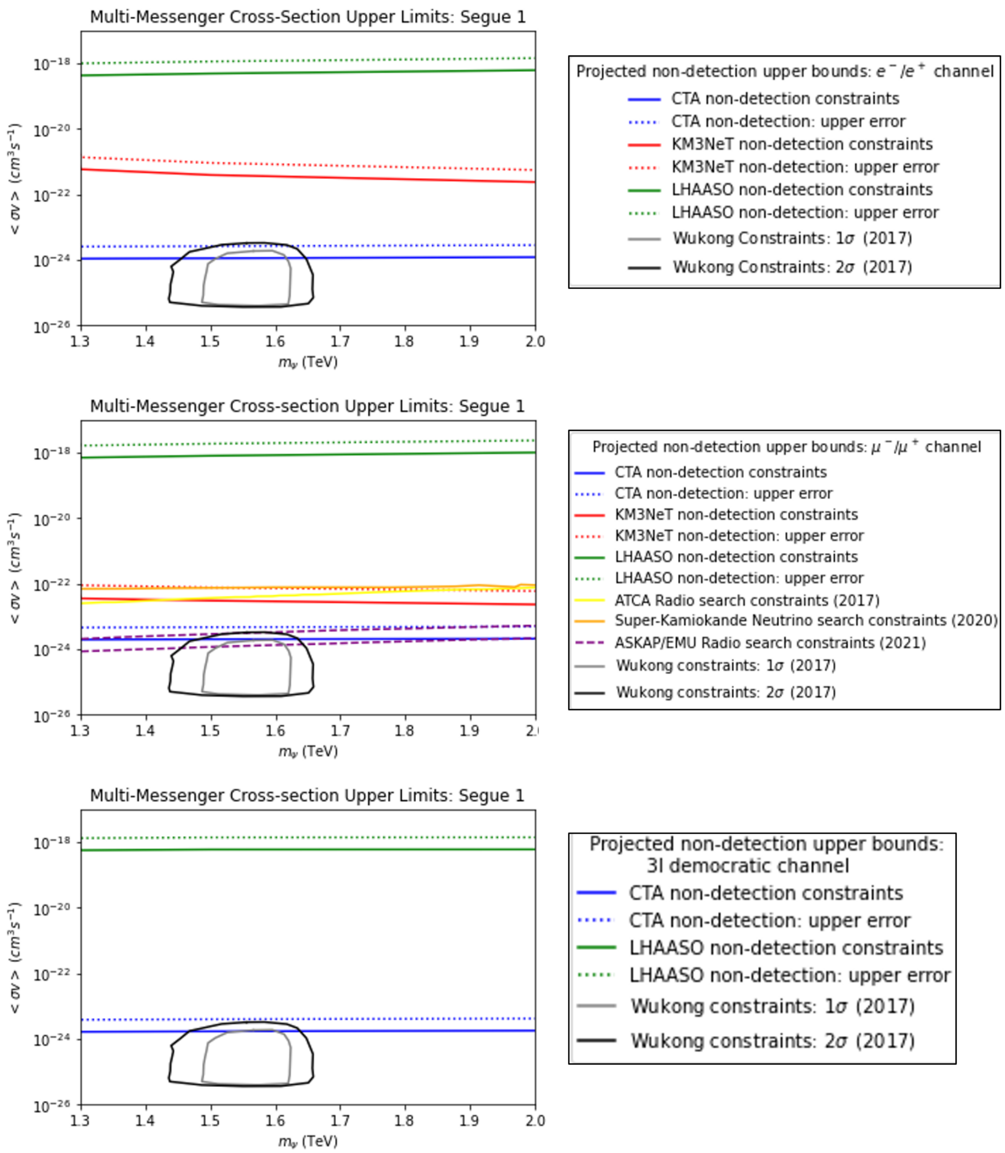

Figure 38: *Projected $\langle \sigma v \rangle_\psi$ upper bounds from non-detection by CTA, LHAASO and KM3NeT observations of the Ultrafaint Segue 1 in the gamma ray and neutrino domains respectively, with each Annihilation channel presented separately.*

For the $e^-/e+$ channel, the most stringent non-detection constraints are imposed by CTA observations of Segue 1, with novel constraints being imposed upon the Wukong fit in [20]. The KM3NeT bounds are more than 10 times weaker, while the LHAASO non-detection constraints are almost 3 orders of magnitude weaker than the CTA bounds. In the case of the μ^-/μ^+ channel, the CTA non-detection upper bounds are the strongest, imposing novel constraints upon the Wukong parameter space in Figure 12 and producing competitive bounds to those imposed by the ASKAP/EMU search in the LMC [35].

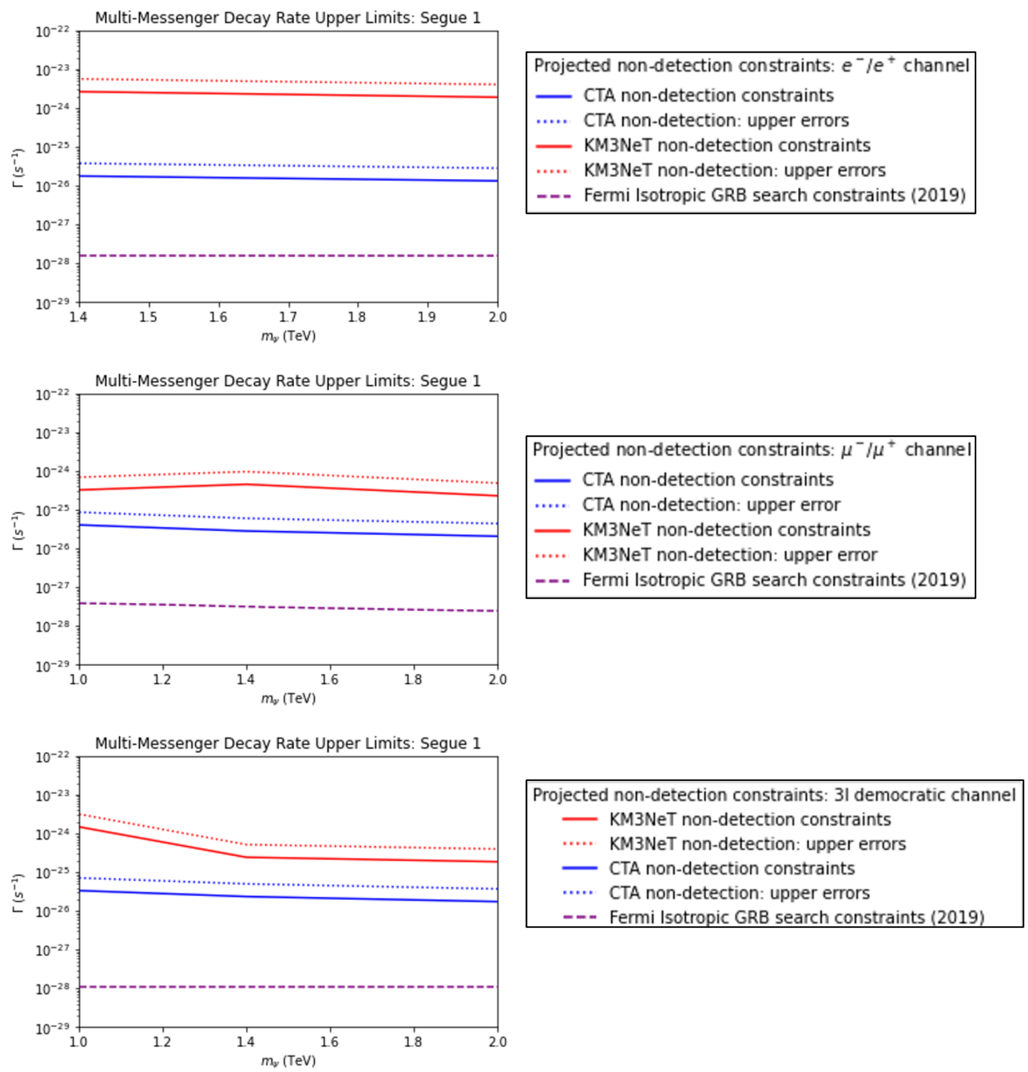

Figure 39: *Projected Γ_ψ upper bounds on account of non-detection by CTA and KM3NeT observations of the Ultrafaint Segue 1 in the gamma ray and neutrino domains respectively.*

ii Reticulum II and Sculptor

Figure 40 presents the respective non-detection upper bounds imposed upon $\langle \sigma v \rangle_\psi$ by observations of the Reticulum II Ultrafaint and the Sculptor Classical utilising CTA and KM3NeT, for the μ^-/μ^+ Annihilation channel. This is taken in comparison to constraints upon WIMP Annihilation along the μ^-/μ^+ channel by Indirect DM searches using ATCA in [23] and Super-Kamiokande in [24].

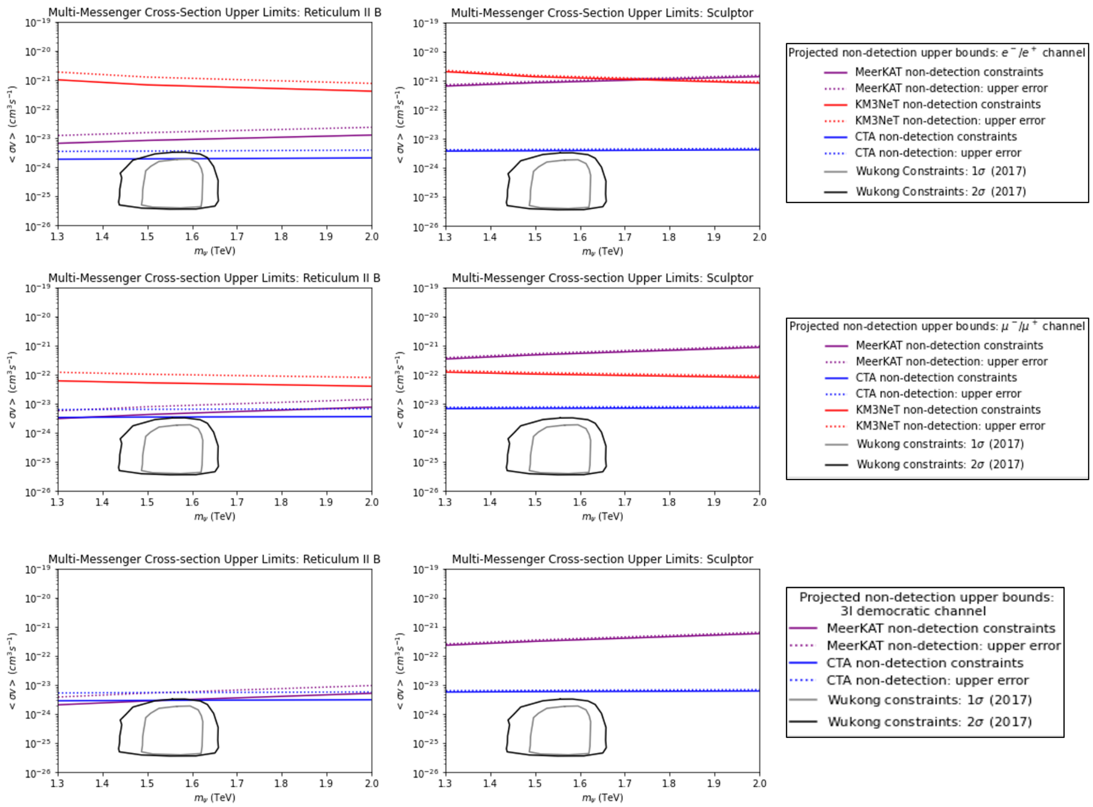

Figure 40: *Projected $\langle \sigma v \rangle_\psi$ upper bounds from non-detection by CTA gamma ray observations, MeerKAT radio observations and KM3NeT neutrino observations of Reticulum II and Sculptor respectively.*

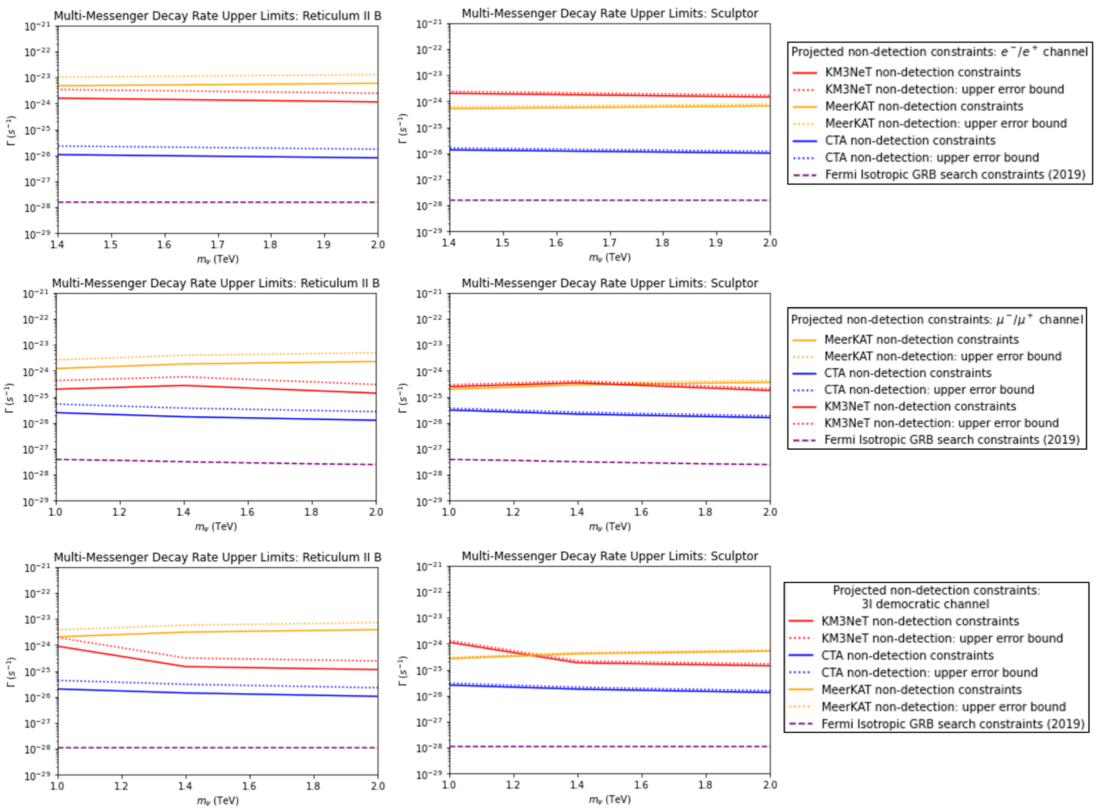

Figure 41: *Projected Γ_ψ upper bounds from non-detection by CTA gamma ray observations, MeerKAT radio observations and KM3NeT neutrino observations of Reticulum II and Sculptor respectively*

VI. Summary and Conclusions

By tracing the historical trajectory of the Dark Matter mystery, through the formulation of the broad WIMP hypothesis considered in this work [10] [11], followed by consecutive failures to detect these hypothetical DM particles through Collider experiments such as those conducted at the LEP collider [12] and the LHC [13] [14] and Direct detection experiments such as LUX [15], PandaX-II and Xenon1T, we illustrate the extent to which the WIMP parameter space has already been constrained, particularly over the past two decades. DM Indirect detection is explored as a third approach, with next generation telescopes able to probe regions of the parameter space that are beyond the capabilities of Direct detection and Collider experiments.

We then explore the results of four Indirect searches in the gamma ray, neutrino and radio domains as points of comparison. For the Annihilation channel, these were the 2017 ATCA Indirect radio search in Reticulum II [23], the 2020 Super-Kamiokande Indirect neutrino search in the Milky Way halo and centre [24] and the 2021 ASKAP/EMU Indirect radio search in the Large Magellanic Cloud [35]. In the Decay case, we consider the 2019 Indirect search in Fermi gamma ray observations of the Isotropic Gamma Ray Background [25].

Thereafter, we consider the unexplained e^-/e^+ flux at approximately 14. TeV detected by Wukong, the Chinese DArk Matter Particle Explorer (DAMPE) cosmic ray detector [21], along with a number of hypothetical Leptophilic WIMP models that were put forward to explain the excess flux detected by Wukong [18] [20] [19]. In devising a model independent test of these proposed models, we consider a mass-energy range of 1 TeV - 2 TeV, with a self-annihilating, fermionic WIMP that couples exclusively to Standard Model leptons - electrons, muons and tauons, along with their associated neutrino flavours [2]. For the purposes of this work, this generalised TeV WIMP hypothesis is termed the Massive Leptophilic Majorana Particle (MLMP) model.

We thereafter explore the potential of dwarf spheroidal galaxies orbiting the Milky Way as astrophysical target environments for DM Indirect detection [22] and motivate six such dwarf spheroidals, four Ultrafaints and two Classicals, as observational targets for the multi-messenger analysis in this work, based primarily upon their astrophysical J- and D-factors, as metrics of suitability for DM Indirect searches for the Annihilation and Decay cases respectively [26].

In laying the theoretical foundations of this work, we consider the mathematical definitions of the J- and D-factors and proceed to re-derive the equations for the WIMP Annihilation Cross-section, $\langle \sigma v \rangle_\psi$ and the Decay Rate, $\langle \Gamma \rangle_\psi$. We thereafter derive equations which account for oscillations in the neutrino domain and synchrotron emission in the radio domain, in addition to an equation to calculate the 3l democratic constraints from the constraints imposed when each leptonic channel is considered exclusively, for both $\langle \sigma v \rangle_\psi$ and $\langle T \rangle_\psi$. Having established the mathematical basis for the WIMP Annihilation cross-section and Decay rate calculations, we then derive equations for the WIMP Mean Free Path, $\langle \lambda \rangle_\psi$ and Mean Annihilation Period, $\langle T \rangle_\psi$, within the DM Halo under consideration, considering cases where the Halo boundary is set to the scale radius and virial radius respectively.

In the gamma ray domain, with 50 hours of observation time [49], CTA observations of the Ultrafaints generally produce stronger non-detection upper bounds upon $\langle \sigma v \rangle_\psi$, although the associated error margins are larger, as seen in Figure 19. In Figure 21, we see that non-detection by CTA yields no new constraints upon the Decay rate upper limits, in comparison to the constraints imposed by the Isotropic GRB search in [25], for all six dwarf spheroidals.

In the case of LHAASO, with an exposure time of 1 year [50], the non-detection bounds, for both $\langle \sigma v \rangle_\psi$ and Γ_ψ even for the Ultrafaints Segue 1 and Triangulum II (at the J-factor upper limit), are the weakest of all the next-generation telescopes, as seen in Figure 38. For the respective Leptonic Annihilation channels, the LHAASO non-detection upper bounds for observations of Segue 1 are approximately five orders of magnitude weaker than the CTA non-detection constraints.

In the neutrino domain, with 10 years of exposure time [49], KM3NeT non-detection imposes no novel constraints upon the $\langle \sigma v \rangle_\psi$ parameter space for observations of all dwarf spheroidals, even in the Triangulum II upper limit special case, as seen in figures 28 and 29. KM3NeT non-detection also imposes no new constraints upon the Decay rate upper limit, with the non-detection limits for observations of all dwarfs being several orders of magnitude less stringent than the constraints in [25].

In the radio domain, with 20 hours of observation time, the MeerKAT non-detection upper bounds upon $\langle \sigma v \rangle_\psi$ are stronger in the case of the Ultrafaint Reticulum II than they are in the case of the Classicals Sculptor and Sextans, although Sculptor does produce significantly stronger constraints than Sextans, with a smaller error margin than is the case for Reticulum II observations. For the μ^-/μ^+ channel, the projected MeerKAT non-detection bounds are competitive with the ASKAP/EMU bounds [35] and more stringent than the Super-Kamiokande constraints [24] and ATCA Indirect radio constraints [23]. For both Reticulum II and Sculptor observations, no novel constraints can be placed upon Γ_ψ for all Leptonic channels, in comparison to the Fermi IGRB constraints [25].

From the multi-messenger analysis, we see that the strongest non-detection upper bounds are yielded from CTA observations of Segue 1 and MeerKAT observations of Reticulum II.

By fixing the value of $\langle \sigma v \rangle_\psi$ at the Dark Matter Relic density limit, we see that the *Virial Annihilation Period* $\left(\langle T \rangle_{\psi,\mathrm{vir}}\right)$ is independent of the Halo features, holding at the virial radius boundary of any DM Halo. The limit we calculate is an absolute upper limit upon the Mean Annihilation Period at the virial radius, at 14 orders of magnitude greater than the Hubble time. If the MAP of a WIMP exceeds our calculated bound on $\langle T \rangle_{\psi,\mathrm{vir}}$ (when $\langle \sigma v \rangle_\psi$ is set to the DM Relic Density limit calculated in [42]), then the MAP corresponds to a WIMP model which cannot account for the DM Relic Density.

As a point of comparison, the mean WIMP lifetime τ_ψ lower limits from [25] are approximately 10-11 orders of magnitude greater than the age of the universe. These stringent lower bounds upon the WIMP mean lifetime are taken as a metric of the severe extent to which the Decay channel has been suppressed. Similarly, the large lower limits on $\langle T \rangle_{\psi,\mathrm{vir}}$, derived from the non-detection upper limits on $\langle \sigma v \rangle_\psi$ for the next generation telescopes under consideration, serve as metrics of the severe extent to which the Annihilation channel has been suppressed, on account of consecutive instances of non-detection by Collider experiments, Direct detection experiments and Indirect detection experiments.
In light of this, astrophysical, non-Dark Matter explanations for the detection of the excess flux by DAMPE, such as those proposed in [18], are favourable. This is on account of the fact that they do not require the introduction of novel hypotheses, which lack empirical support, in order to explain the Wukong flux detected in 2017 [21]. This will be explored further in Appendix A.

VII. Appendices

1. Appendix A: Alternate Explanations for the DAMPE Excess Flux

If the MLMP hypothesis under consideration here is proven to be false, then the excess e^-/e^+ flux detected by DAMPE in [21] must be accounted for by some other astrophysical phenomenon. In [18], Yuan et. al. propose a number of alternative, non-Dark Matter astrophysical explanations for the excess flux, highlighting pulsars, pulsar wind nebulae and/or supernova remnants as sources of high energy electrons and positrons. They focus specifically on a pulsar scenario to account for the Wukong flux [18], with the model fit to the DAMPE data (along with the AMS-02 data) presented in Figure 42.

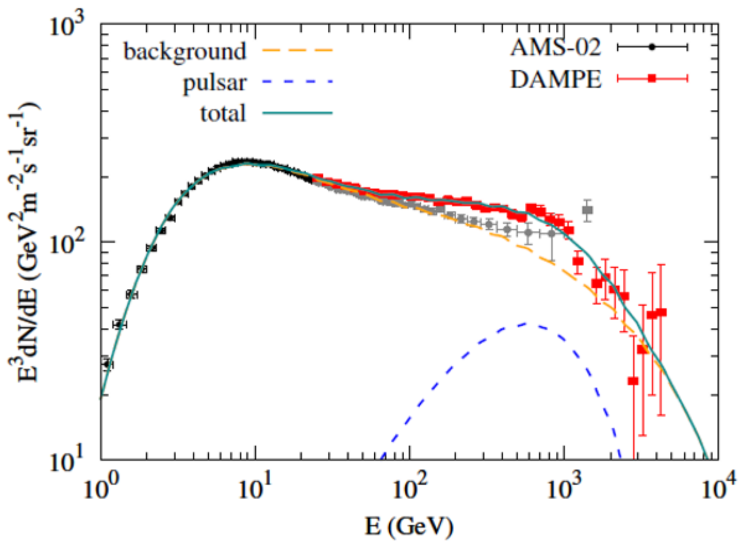

Figure 42: *Pulsar model in [18] which best fits the DAMPE data*

The model assumes that the source is a relatively young ($\leq 10^5$ years old) pulsar, with a rotation period of ~ 0.1 s, at a relatively close distance (≤ 1 kpc) [18].

2. Appendix B: Empirical Scaling Relations for J- and D-Factors

The authors of [26] derive the following scaling relations for the J- and D-factors:

$$J(0.5^\circ) = 10^{17.87} \left(\frac{\sigma_{\rm los}}{5kms^{-1}}\right)^4 \left(\frac{D_L}{100kpc}\right)^{-2} \left(\frac{r_h}{100pc}\right)^{-1} \tag{74}$$

$$D(\theta) = 10^{16.57} \left(\frac{\sigma_{\rm los}}{5kms^{-1}}\right)^2 \left(\frac{D_L}{100kpc}\right)^{-2} \left(\frac{r_h}{100pc}\right)^{+1} \tag{75}$$

These relations are particularly useful for DM Indirect detection for newly-discovered systems where the full dynamical analysis cannot be performed, given the absence of high quality stellar kinematic data for these systems [26]. Thus, the J- (and D-) factors can be ascertained without the need to choose a particular Halo density profile [26]. However, it must be noted that relation 75 for the D-factor scaling only applies when $\theta = \frac{\alpha_c}{2}$, where α_c is the angle which minimises the error for the J-factor analysis [26].

Furthermore, in [63], which utilises mock data sets, the J-factor was shown to be systematically overstated when it is not assumed that the scale radius is larger than the half-light radius. In line with this result, the authors of [26] impose a $r_s > r_h$ Halo prior. In analytically deriving the J-factor scaling relation, the authors of [26] find the same normalisation as their original scaling relation when $r_s \approx 4r_h$.

3. Appendix C: D-factor Relation at the Virial Radius Boundary

At the virial radius, $r = r_{\rm vir}$, Equation 52 for $\langle\lambda\rangle_\psi$must be equivalent to the equation for $\langle\lambda\rangle_\psi$in Equation 56, yielding the following relation for the D-factor:

$$D(\theta_{\rm vir}) = 6\pi^2\rho_c \frac{r_{\rm vir}^3}{D_L^2} \tag{76}$$

To obtain the virial radius, we can combine the virial relation for the average density in Equation 55 with the simply definition of the average density of the dwarf at $r = r_{\rm vir}$. For convenience, we find the virial radius cubed:

$$\langle\rho\rangle_{\rm vir} = 18\pi^2\rho_c = \frac{M_{\rm vir}}{\frac{4}{3}\pi r_{\rm vir}^3} \to r_{\rm vir}^3 = \frac{M_{\rm vir}}{24\pi^3\rho_c} \tag{77}$$

We substitute Equation 77 into Equation 76:

$$D\left(\theta_{\rm vir}\right) = \frac{M_{\rm vir}}{4\pi D_L^2} \tag{78}$$

The D-factors at the virial radius boundaries $\theta = \theta_{\rm vir}$ of three of our target dwarf spheroidals, along with their virial masses $M_{\rm vir}$, are presented in Table 7.

Dwarf Spheroidal	$M_{\rm vir}\ (10^6 M_\odot)$	$\log\left(D(\theta_{\rm vir})\right)$
Reticulum II B	23.34	$17.33^{+0.05}_{-0.06}$
Sculptor	720.10	$18.82^{+0.05}_{-0.06}$
Sextans	636.10	$17.84^{+0.02}_{-0.02}$

Table 7: *Logarithm of the D-factors, in units of GeV* cm^{-2} *at the virial boundaries of the Ultrafaint Reticulum II and the Classicals Sculptor and Sextans.*

4. Appendix D: Literature Review on Alternative Dark Matter models to WIMPs

i Sterile Neutrinos

Neutrinos are long-lived particles with no charge and in general, it has been empirically shown that at least two of the three neutrino flavours are not massless [88]. These relatively stable, neutral particles do not interact with the electromagnetic force, but they can participate in Weak interactions, particularly in the early universe, where the Weak interactions allowed the neutrinos to maintain thermal equilibrium for a period, until the universe expanded and cooled sufficiently for the neutrinos to *freeze out* [88]. In this *Hot Dark Matter* (HDM) model, the neutrinos decouple at relativistic velocities, before primordial nucleosynthesis, only entering the non-relativistic domain later during the matter-dominated epoch [88].

The upper limit on the sum of the SM neutrino masses across all three flavors is experimentally determined to be around 2 TeV, while cosmological data reduces this cumulative mass even further, as detailed in [88]. However, non-relativistic neutrinos, in the current, matter-dominated era, must have a cumulative mass of approximately 11.5 eV in order for the associated neutrino mass density to account for the total abundance of DM at present, thus eliminating SM neutrinos as candidates for particle DM [88].

In extending the SM, sterile, heavy neutrinos are presented as a candidate for particle DM [88]. In 1994, Dodelson and Widrow published a paper extending the analysis of the sterile neutrino particle DM hypothesis from the HDM paradigm into the CDM paradigm, accounting for structure formation with a sterile neutrino with a mass on the order of 1 keV [33].

ii Modified Newtonian Dynamics

In 1983, Mordehai Milgrom published three papers in the Astrophysical Journal, with the first laying out a hypothesis which modifies standard Newtonian physics [31]. The second lays out the consequences of this Modified Newtonian Dynamics (MOND) hypothesis on the galactic scale [89] and the third calculates its consequences for the physics of galaxy clusters [32].

Mordehai's MOND hypothesis relies upon a number of assumptions, so as to create a model wherein the observed DM gravitational phenomena could be explained without the need for an extension to the Standard Model, thereby eliminating the need for Particle DM, or any "Hidden Mass Hypothesis" [31].

The first MOND assumption relies upon the modification of the gravitational acceleration, $a(r)$, of a massive particle located at a particularly large radial distance away from a (larger) massive body with mass M. where gravity is taken to be the only acting force [31]. For a particular acceleration constant a_0 , which is radially-independent and arbitrary, the following equation is derived as a modification of Newton's Second Law in the small acceleration limit, where $a(r) << a_0$ [31].

$$\frac{a(r)^2}{a_0} = \frac{a(r)}{a_0} a(r) \approx \frac{GM}{r^2} \tag{79}$$

The term on the right-hand-side of Equation 79 is the familiar Newtonian formula for the gravitational acceleration, a(r), of any particle gravitationally interacting with mass M at a distance

r. The equivalent acceleration on the left-hand-side, valid only in the small acceleration limit, is equivalent to the usual gravitational acceleration derived from Newton II, multiplied by the ratio of the acceleration at r to the acceleration constant, a_0.

iii Axions

In 1977, the same year that the WIMP model was first formulated [10] [11], Roberto Peccei and Helen Quinn published two papers on Charge-Parity (CP) conservation, the first of which explores CP symmetry in the presence of pseudo-particles [28] and the second of which then fleshes out the further constraints imposed by that pseudo-particle presence [29]. The first paper considers CP conservation in the case of the Strong Nuclear force, theoretically accounting for the *'Strong CP problem'* by assuming that at least one fermion flavour acquires its mass by virtue of a Yukawa coupling to an introduced pseudo-scalar field [28]. The next year, in a paper exploring the Peccei-Quinn pseudo-scalar field, Steven Weinberg terms the neutral quanta of this field, which has a non-vanishing vacuum expectation value, *Axions*, after a brand of laundry detergent [90].

The second paper extends the theoretical analysis from the Quantum Chromodynamics (QCD) analysis in the prior paper [28] to now account for the Electromagnetic and Weak Nuclear forces [29]. Thus, the scalar field proposed by Peccei and Quinn [28] accounts for the problem of CP Conservation, which, alongside the Dark Matter mystery, is an enduring enigma in contemporary physics.

In 1990, following a related conference, Fermilab's Michael Turner published a report reviewing experimental constraints established upon the hypothetical Axion mass at the time [30].

In 2020, Co and Harigaya published a paper proposing a process termed *Axiogenesis* to account for the abundance of ordinary, baryonic matter over the respective anti-particle counterparts, another enduring mystery in contemporary physics [91]. By assuming the postulation that there are no Global symmetries in nature, the authors demonstrate that the matter-anti matter asymmetry can be accounted for by Axions [91].

Probing Axion-like particles using next-generation telescopes like MeerKAT via DM Indirect detection is discussed further in [92].

5. Appendix E: Error Analysis

i WIMP Annihilation Cross-Section

The only error associated with $\langle\sigma v\rangle_\psi$ in Equation 18 is the error associated with the empirical J-factor. Thus, the error on the Annihilation Cross Section is given by:

$$\Delta\langle\sigma v\rangle_\psi = \frac{\partial\langle\sigma v\rangle_\psi}{\partial J}\Delta J = -\frac{\langle\sigma v\rangle_\psi}{J}\Delta J \tag{80}$$

The literature values (and their respective errors) are quoted as the logarithm of the J-factor. We write:

$$J = J(x) = 10^x \tag{81}$$

where x is the value quoted in the literature. Thus:

$$\Delta J = \frac{\partial J}{\partial x}\Delta x = ln(10)10^x\Delta x = ln(10)J\Delta x \tag{82}$$

The error in $\langle\sigma v\rangle_\psi$ is hence given by:

$$\Delta\langle\sigma v\rangle_\psi = -ln(10)\langle\sigma v\rangle_\psi\Delta x \tag{83}$$

ii WIMP Decay Rate

Similarly to the case with the Annihilation Cross-Section, the only error associated with the MLMP Decay Rate is the error on the empirical D-Factor. Thus, the error on Γ_ψ is:

$$\Delta\Gamma_\psi = \frac{\partial\Gamma_\psi}{\partial D}\Delta D = \frac{\partial\Gamma_\psi}{\partial D}ln(10)D\Delta y \tag{84}$$

where y is the logarithm of the D-factor quoted in the literature. The partial derivative of Γ_{psi} with respect to the D-factor is given by:

$$\frac{\partial\Gamma_\psi}{\partial D} = -\frac{\Gamma_\psi}{D} \tag{85}$$

The error on the Decay Rate is hence given by:

$$\Delta\Gamma_\psi = -ln(10)\Gamma_\psi\Delta y \tag{86}$$

iii WIMP Mean Free Path and Mean Annihilation Period

Halo boundary at the scale radius: $r = r_s$

For $\langle\lambda\rangle_\psi$ there are four variables with associated errors: the velocity dispersion, the luminosity distance, the annihilation cross section and the astrophysical D-factor. The error in $\langle\lambda\rangle_\psi$ in this case is hence given by:

$$\Delta\langle\lambda\rangle_\psi = \frac{\partial\langle\lambda\rangle_\psi}{\partial\sigma_{\text{los}}}\Delta\sigma_{\text{los}} + \frac{\partial\langle\lambda\rangle_\psi}{\partial\langle\sigma v\rangle_\psi}\Delta\langle\sigma v\rangle_\psi + \frac{\partial\langle\lambda\rangle_\psi}{\partial D}\Delta D + \frac{\partial\langle\lambda\rangle_\psi}{\partial D_L}\Delta D_L \tag{87}$$

Performing the necessary partial differentiation yields the following expression for the error on the Mean Free Path:

$$\Delta\langle\lambda\rangle_{\psi} = \langle\lambda\rangle_{\psi}\left(\frac{\Delta\sigma_{\rm los}}{\sigma_{\rm los}} - \frac{\Delta\langle\sigma v\rangle_{\psi}}{\langle\sigma v\rangle_{\psi}} - ln(10)\Delta y - \frac{\Delta D_L}{2D_L}\right) \tag{88}$$

Through partial differentiation of $\langle T\rangle_{\psi}$ with respect to both $\sigma_{\rm los}$ and $\langle\lambda\rangle_{\psi}$ the error on the Mean Annihilation Period at the virial radius is given by:

$$\Delta\langle T\rangle_{\psi} = \langle T\rangle_{\psi}\left(\frac{\Delta\langle\lambda\rangle_{\psi}}{\langle\lambda\rangle_{\psi}} - \frac{\Delta\sigma_{\rm los}}{\sigma_{\rm los}}\right) = -\langle T\rangle_{\psi}\left(\frac{\Delta\langle\sigma v\rangle_{\psi}}{\langle\sigma v\rangle_{\psi}} + ln(10)\Delta y + \frac{\Delta D_L}{2D_L}\right) \tag{89}$$

Halo boundary at the virial radius: $r = r_{\rm vir}$

At the virial radius Halo boundary, $\langle\lambda\rangle_{\psi}$ has three variables with associated errors: the line-of-sight velocity dispersion, $\sigma_{\rm los}$, the critical density, ρ_c and the Annihilation Cross-section, $\langle\sigma v\rangle_{\psi}$. The error in $\langle\lambda\rangle_{\psi}$ is hence given by:

$$\Delta\langle\lambda\rangle_{\psi} = \frac{\partial\langle\lambda\rangle_{\psi}}{\partial\sigma_{\rm los}}\Delta\sigma_{\rm los} + \frac{\partial\langle\lambda\rangle_{\psi}}{\partial\rho_c}\Delta\rho_c + \frac{\partial\langle\lambda\rangle_{\psi}}{\partial\langle\sigma v\rangle_{\psi}}\Delta\langle\sigma v\rangle_{\psi} = \langle\lambda\rangle_{\psi}\left(\frac{\Delta\sigma_{\rm los}}{\sigma_{\rm los}} - \frac{\Delta\rho_c}{\rho_c} - \frac{\Delta\langle\sigma v\rangle_{\psi}}{\langle\sigma v\rangle_{\psi}}\right) \tag{90}$$

Employing the expression for $\Delta\langle\sigma v\rangle_{\psi}$ in 83 and expressing the error on the critical density in terms of the error on the Hubble constants H_0, we have the error on $\langle\lambda\rangle_{\psi}$ as:

$$\Delta\langle\lambda\rangle_{\psi} = \langle\lambda\rangle_{\psi}\left(\frac{\Delta\sigma_{\rm los}}{\sigma_{\rm los}} - 2\frac{\Delta H_0}{H_0} + ln(10)\Delta x\right) \tag{91}$$

For the WIMP MAP at the virial radius $\left(\langle T\rangle_{\psi,\rm vir}\right)$, the only variables with associated errors are ρ_c and $\langle\sigma v\rangle_{\psi}$. Writing again the error on the critical density in terms of the error on the Hubble constant H_0 and substituting the error in $\langle\sigma v\rangle_{\psi}$ from Equation 83, yields the following error on $\langle T\rangle_{\psi,\rm vir}$:

$$\Delta\langle T\rangle_{\psi,vir} = -\langle T\rangle_{\psi,vir}\left(2\frac{\Delta H_0}{H_0} - ln10\Delta x\right) \tag{92}$$

6. Appendix F: Table Cross-Referencing Dark Matter History Timeline

Each alphabetical reference in Figure 1 corresponds to a reference in the Bibliography of this work. Table 8 details the cross-references for the DM history timeline in Figure 1.

Year	Timeline Reference	Bibliography Reference	Year	Timeline Reference	Bibliography Reference
1933	*a*	[1]	2008	*s*	[36]
1965	*b*	[5]	2012	*t*	[13]
1965	*c*	[6]	2014	*u*	[14]
1970	*d*	[3]	2015	*v*	[7]
1973	*e*	[4]	2016	*w*	[17]
1973	*f*	[27]	2017	*x*	[23]
1977	*g*	[11]	2017	*y*	[15]
1977	*h*	[10]	2017	*z*	[2]
1977	*i*	[28]	2017	*aa*	[21]
1977	*j*	[29]	2017	*ab*	[20]
1978	*k*	[93]	2017	*ac*	[18]
1978	*l*	[90]	2017	*ad*	[19]
1983	*m*	[31]	2018	*ae*	[16]
1983	*n*	[89]	2019	*af*	[25]
1983	*o*	[32]	2020	*ag*	[24]
1994	*p*	[33]	2021	*ah*	[37]
1994	*q*	[88]	2021	*ai*	[35]
2006	*r*	[12]			

Table 8: *Cross-references for the red, italicised references on the DM history timeline in Figure 1.*

References

[1] F. Zwicky. The Redshift of Extragalactic Nebulae. *Helvetica Physica Acta*, 6:110–127, 1933.

[2] N.F. Bell, Y. Cai, R.K. Leane, and A.D Medina. Leptophilic Dark Matter with Z' interactions. *Physical Review D*, 90 (3), 2014.

[3] V. C. Rubin and Jr. Ford, W. K. Rotation of the Andromeda Nebula from a Spectroscopic Survey of Emission Regions. *Astrophysical Journal*, 159, 1970.

[4] J. Ostriker and P. Peebles. A Numerical Study of the Stability of Flattened Galaxies: Or, Can Cold Galaxies Survive? *The Astrophysical Journal*, 186:467 – 480, 1973.

[5] A. A. Penzias and R. W. Wilson. A Measurement of Excess Antenna Temperature at 4080 Mc/s. *Astrophysical Journal*, 142, 1965.

[6] R. H. Dicke, P. J. E. Peebles, P. G. Roll, and D. T. Wilkinson. Cosmic Black-Body Radiation. *Astrophysical Journal*, 142, 1965.

[7] P. A. R. Ade, N. Aghanim, M. Arnaud, M. Ashdown, J. Aumont, C. Baccigalupi, A. J. Banday, R. B. Barreiro, et al. Planck 2015 results. XIII. Cosmological parameters. *Astronomy and Astrophysics*, 594, 2016.

[8] J. Primack. Dark Matter and Structure Formation in the Universe. 1997.

[9] Robert H. Sanders. *The Dark Matter Problem*. Cambridge University Press, 2010.

[10] B. W. Lee and S. Weinberg. Cosmological Lower Bound on Heavy Neutrino Masses. *Physical Review Letters*, 39, 1977.

[11] P. Hut. Limits on Masses and Number of Neutral Weakly Interacting Particles. *Physics Letters B*, 69, 1977.

[12] J. Alcaraz et al. A Combination of Preliminary Electroweak Measurements and Constraints on the Standard Model. 2006.

[13] S. Chatrchyan, V. Khachatryan, et al. Observation of Z decays to four leptons with the CMS detector at the LHC. *Journal of High Energy Physics*, 2012 (34), 2012.

[14] G. Aad, B. Abbott, J. Abdallah, S. Abdel Khalek, O. Abdinov, et al. Measurement of the 4l Cross Section at the Z Resonance and Determination of the Branching Fraction of Z->4l in pp Collisions at sqrt(s) = 7 and 8 TeV with ATLAS. *Physical Review Letters*, 112, 2014.

[15] D.S. Akerib, S. Alsum, H.M. Araújo, X. Bai, A.J. Bailey, J. Balajthy, P. Beltrame, et al. Results from a search for dark matter in the complete LUX exposure. *Physical Review Letters*, 118, 2017.

[16] E. Aprile, J. J. Aalbers, F. Agostini, M. Alfonsi, et al. Dark Matter Search Results from a One Tonne × Year Exposure of XENON1T. *Physical Review Letters*, 121, 2018.

[17] A. Tan, M. Xiao, X. Cui, X. Chen, Y. Chen, and others. Dark Matter Results from First 98.7-day Data of PandaX-II Experiment. *Physical Review Letters*, 117, 2016.

[18] Q. Yuan, L. Feng, P.F. Yin, and Fan Y.Z. Interpretations of the DAMPE Electron Data. 2017.

[19] F. Yang and M. Su. Dark Matter Annihilation from Nearby Ultra-Compact Micro Halos to Explain the Tentative Excess at 1.4 TeV in DAMPE data. 2017.

[20] Y.Z. Fan, W.C. Huang, M. Spinrath, Y.L.S. Tsai, and Q. Yuan. A model explaining neutrino masses and the DAMPE cosmic ray electron excess. *Physics Letters B*, 781:83–87, 2018.

[21] DAMPE. Collaboration. Direct Detection of a Break in the Terraelectronvolt Cosmic-Ray Spectrum of Electrons and Positrons. *Nature*, 552:63, 2017.

[22] L. E. Strigari. Dark Matter in Dwarf Spheroidal Galaxies and Indirect Detection: A Review. *Reports on progress in physics. Physical Society*, 81 5, 2018.

[23] M. Regis, L. Richter, and S. Colafrancesco. Dark matter in the Reticulum II dSph: a radio search. *Journal of Cosmology and Astroparticle Physics*, 2017, 2017.

[24] K. Abe, C. Bronner, Y. Haga, Y. Hayato, M. Ikeda, S. Imaizumi, H. Ito, K. Iyogi, J. Kameda, Y. Kataoka, Y. Kato, Y. Kishimoto, Lluis Marti Magro, M. Miura, Sae Moriyama, T. Mochizuki, Y. Nagao, M. Nakahata, Y. Nakajima, and G. Pintaudi. Indirect search for dark matter from the Galactic Center and halo with the Super-Kamiokande detector. *Physical Review D*, 102, 2020.

[25] C. Blanco and D. Hooper. Constraints on decaying dark matter from the isotropic gamma-ray background. *Journal of Cosmology and Astroparticle Physics*, 2019, 2019.

[26] A. Pace and L. Strigari. Scaling Relations for Dark Matter Annihilation and Decay Profiles in Dwarf Spheroidal Galaxies. *Monthly Notices of the Royal Astronomical Society*, pages 1 – 19, 2018.

[27] M.S. Roberts and A.H. Rots. Comparison of Rotation Curves of Different Galaxy Types. *Astronomy & Astrophysics*, 26, 1973.

[28] R. D. Peccei and Quinn H.R. CP Preservation in the Presence of Pseudoparticles. *Physical Review Letters*, 38, 1977.

[29] R. D. Peccei and Quinn H.R. Constraints imposed by CP conservation in the presence of pseudoparticles. *Physical Review D*, 16, 1977.

[30] M. S. Turner. Windows on the Axion. *Physics Reports*, 197, 1990.

[31] M. Milgrom. A modification of the Newtonian dynamics as a possible alternative to the hidden mass hypothesis. *Astrophysical Journal*, 270, 1983.

[32] M. Milgrom. A modification of the Newtonian dynamics: Implications for galaxy systems. *Astrophysical Journal*, 270, 1983.

[33] S. Dodelson and L. M. Widrow. Sterile neutrinos as dark matter. *Physical Review Letters*, 72, 1994.

[34] M. L. Benabderrahmane. Latest results from the XENON1T experiment. *Journal of Physics: Conference Series*, 1258, 2019.

[35] M. Regis, J. Reynoso-Cordova, M. D. Filipović, and others. The EMU view of the Large Magellanic Cloud: Troubles for sub-TeV WIMPs. *Journal of Cosmology and Astroparticle Physics*, 2021, 2021.

[36] R. Bernabei, P. Belli, F. Cappella, R. Cerulli, C. J. Dai, A. d'Angelo, H. L. He, A. Incicchitti, H. H. Kuang, J. M. Ma, F. Montecchia, F. Nozzoli, D. Prosperi, X. D. Sheng, and Z. P. Ye. First results from DAMA/LIBRA and the combined results with DAMA/NaI. *The European Physical Journal C*, 56, 2008.

[37] J. Amaré, S. Cebrián, D. Cintas, I. Coarasa, et al. Annual modulation results from three-year exposure of ANAIS-112. *Journal of Physics: Conference Series*, 2156, 2021.

[38] C. F. P. da Silva et al. Dark Matter Searches with LUX. 2017.

[39] Gianfranco Bertone, editor. *Particle Dark Matter*. Cambridge University Press, 2010.

[40] J. Heisig, M. Korsmeier, and M. Winkler. Dark matter or correlated errors? Systematics of the AMS-02 antiproton excess. 2020.

[41] Y. Zhao, K. Fang, M. Su, and M.C. Miller. A Strong Test of the Dark Matter Origin of the 1.4 TeV DAMPE Signal Using IceCube Neutrinos. *Journal of Cosmology and Astroparticle Physics*, 2018, 2018.

[42] G. Steigman, B. Dasgupta, and J.F. Beacom. Precise Relic WIMP Abundance and its Impact on Searches for Dark Matter Annihilation. *Physical Review D.*, 86, 2012.

[43] G. Jungman, M. Kamionkowski, and K. Griest. Supersymmetric Dark Matter. *Physics Reports*, 267, 1996.

[44] T. R. Slatyer, N. Padmanabhan, and D. P. Finkbeiner. CMB Constraints on WIMP Annihilation: Energy Absorption During the Recombination Epoch. *Physical Review D*, 80, 2009.

[45] P. J. Fox, R. Harnik, J. Kopp, and Y. Tsai. LEP Shines Light on Dark Matter. *Physical Review D*, 84, 2011.

[46] F. D'Eramo, B. J. Kavanagh, and P. Panci. Probing Leptophilic Dark Sectors with Hadronic Processes. *Physics Letters B*, 771, 2017.

[47] A. Genina and M. Fairbairn. The potential of the Dwarf Galaxy Triangulum II for Dark Matter indirect detection. *Monthly Notices of the Royal Astronomical Society*, 463:3630–3636, 2016.

[48] B.P.M. Laevens, N.F. Martin, R.A. Ibata, H. Rix, et al. A New Faint Milky Way Satellite Discovered in the Pan-STARRS 3 π Survey. *The Astrophysical Journal Letters*, 802 (2), 2015.

[49] L. Ambrogi, S. Celli, and F. Aharonian. On the potential of Cherenkov Telescope Arrays and KM3 Neutrino Telescopes for the detection of extended sources. *Astro Particle Physics*, 100:69 – 79, 2018.

[50] A. Neronov and D. Semikoz. LHAASO sensitivity for diffuse gamma-ray signals from the Galaxy. *Phys. Rev. D*, 102, 2020.

[51] Z. Cao, D. della Volpe, S. Liu, et al. The Large High Altitude Air Shower Observatory (LHAASO) Science Book (2021 Edition). *Chinese Physics C*, 46, 2022.

[52] J. L. Jonas and the MeerKAT team. The MeerKAT Radio Telescope. 2016.

[53] M. Bailes, A. Jameson, F. Abbate, E. D. Barr, et al. The MeerKAT Telescope as a Pulsar Facility: System verification and early science results from MeerTime. *Publications of the Astronomical Society of Australia*, 37, 2020.

[54] G. Beck and S. Makhathini. Just a MeerKAT, or a dark matter machine?, 2023.

[55] J. A. R. Cembranos, A. de la Cruz-Dombriz, V. Gammaldi, and M. Mendez-Isla. SKA-Phase 1 sensitivity to synchrotron radio emission from multi-TeV Dark Matter candidates. *Physics of the Dark Universe*, 27, 2020.

[56] G. Beck. Radio-Frequency Searches for Dark Matter in Dwarf Galaxies. *Galaxies*, 2019.

[57] G. Beck. An Excess of Excesses Examined via Dark Matter Radio Emissions from Galaxies. *Journal of Cosmology and Astroparticle Physics*, 2019:019–019, 2019.

[58] J. Einasto. On the Construction of a Composite Model for the Galaxy and on the Determination of the System of Galactic Parameters. *Trudy Astrofizicheskogo Instituta Alma-Ata*, 5, 1965.

[59] A. Burkert. The Structure of Dark Matter Haloes in Dwarf Galaxies. *Astrophysical Journal Letters*, 447, 1995.

[60] J.F. Navarro, C.S. Frenk, and S.D.M. White. The Structure of Cold Dark Matter Halos. *Astrophysical Journal*, 462, 1996.

[61] H. Zhao. Analytical Models of Galactic Nuclei. *Monthly Notices of the Royal Astronomical Society*, 278, 1996.

[62] J. S. B. Wyithe, E. L. Turner, and D. N. Spergel. Gravitational Lens Statistics for Generalized NFW Profiles: Parameter Degeneracy and Implications for Self-Interacting Cold Dark Matter. *The Astrophysical Journal*, 555, 2001.

[63] V. Bonnivard, C. Combet, M. Daniel, et al. Dark Matter Annihilation and Decay in Dwarf Spheroidal Galaxies: The Classical and Ultrafaint dSphs. *Monthly Notices of the Royal Astronomical Society*, 453:849 – 867, 2015.

[64] N. Evans, J. Sanders, and A. Geringer-Sameth. Simple J-Factors and D-Factors for Indirect Dark Matter Detection. *Physical Review D*, 93, 2016.

[65] G. Beck and S. Colafrancesco. Dark Matter gets DAMPE, 2018. Conference proceedings.

[66] G. Fantini, A. G. Rosso, F. Vissani, and V. Zema. The formalism of neutrino oscillations: an introduction. In A. Ereditato, editor, *The State of the Art of Neutrino Physics*. World Scientific Publishing Company, 2018.

[67] G. Beck and M. Sarkis. Galaxy clusters in high definition: A dark matter search. *Physical Review D*, 107, 2023.

[68] S. Colafrancesco, S. Profumo, and P. Ullio. Multi-frequency analysis of neutralino dark matter annihilations in the Coma cluster. *Astronomy and Astrophysics*, 455, 2006.

[69] M. Sarkis and G. Beck. Simulating the radio emissions of dark matter for new high-resolution observations with MeerKAT. 2023.

[70] G. Beck and M. Sarkis. Galaxy clusters in high definition: a dark matter search. *Physical Review D*, 107, 2023.

[71] G.L. Bryan and M.L. Norman. Statistical Properties of X-ray Clusters: Analytic and Numerical Comparisons. *The Astrophysical Journal*, 495:80 – 99, 1998.

[72] A. Friedmann. Über die Krümmung des Raumes (On the Curvature of Space). *Zeitschrift fur Physik*, 10, 1922.

[73] A. Friedmann. Über die Möglichkeit einer Welt mit konstanter negativer Krümmung des Raumes (On the Possibilitiy of a Universe with Constant Negative Curvature of Space). *Zeitschrift für Physik*, 21, 1924.

[74] H. Shapley. A Stellar System of a New Type. *Monthly Notices of the Royal Astronomical Society*, 908, 1938.

[75] H. Shapley. Two Stellar Systems of a New Kind. *Harvard College Observatory Bulletin*, 142, 1938.

[76] M.J. Irwin, P.S. Bunclark, M.T. Bridgeland, and R.G. McMahon. A new satellite galaxy of the Milky Way in the constellation of Sextans. *Monthly Notices of the Royal Astronomical Society*, 244, 1990.

[77] V. Belokurov, D. B. Zucke, N. W. Evans, J. T. Kleyna, S. Koposov, S. T. Hodgkin, M. J. Irwin, G. Gilmore, et al. Cats and Dogs, Hair and a Hero: A Quintet of New Milky Way Companions. *The Astrophysical Journal*, 654, 2007.

[78] N.F. Martin, J.T.A. de Jong, and H. Rix. A comprehensive Maximum Likelihood analysis of the structural properties of faint Milky Way satellites. *The Astrophysical Journal*, 684, 2008.

[79] M. Niederste-Ostholt, V. Belokurov, N. W. Evans, G. Gilmore, R. F. G. Wyse, and J. E. Norris. The origin of Segue 1. *Monthly Notices of the Royal Astronomical Society*, 398, 2009.

[80] D. S. Joshua, G. Marla, E. M. Quinn, D. M. Gregory, Evan N. K. Kirby, et al. A Complete Spectroscopic Survey of the Milky Way Satellite Segue 1: The Darkest Galaxy. *The Astrophysical Journal*, 733, 2011.

[81] S. Koposov, V. Belokurov, G. Torrealba, and N. Evans. Beasts of the Southern Wild: Discovery of nine Ultra Faint satellites in the vicinity of the Magellanic Clouds. *The Astrophysical Journal*, 805, 2015.

[82] K. Bechtol, A. Drlica-Wagner, E. Balbinot, A. Pieres, J.D. Simon, et al. EIGHT NEW MILKY WAY COMPANIONS DISCOVERED IN FIRST YEAR DARK ENERGY SURVEY DATA. *The Astrophysical Journal*, 807, 2015.

[83] A. Chiti, A. Frebel, J.D. Simon, et al. An extended halo around an ancient dwarf galaxy. *Nature Astronomy*, 5, 2021.

[84] M. Cirelli, G. Corcella, A. Hektor, et al. PPPC 4 DM ID: A Poor Particle Physicist Cookbook for Dark Matter Indirect Detection. *Journal of Cosmology and Astroparticle Physics*, 51, 2011.

[85] P. Ciafaloni, D. Comelli, A. Riotto, F. Sala, A. Strumia, and A. Urbano. Weak corrections are relevant for dark matter indirect detection. *Journal of Cosmology and Astroparticle Physics*, 19, 2011.

[86] S. Colafrancesco and P. Blasi. Clusters of Galaxies and the Diffuse Gamma Ray Background. *Astroparticle Physics*, 9, 1998.

[87] Planck Collaboration. Planck 2018 Results. VI. Cosmological Parameters. *Astronomy and Astrophysics*, 641, 2020.

[88] A. Boyarsky, M. Drewes, T. Lasserre, S. Mertens, and O. Ruchayskiy. Sterile Neutrino Dark Matter. *Progress in Particle and Nuclear Physics*, 104, 2019.

[89] M. Milgrom. A modification of the Newtonian dynamics - Implications for galaxies. *Astrophysical Journal*, 270, 1983.

[90] S. Weinberg. A New Light Boson? *Physical Review Letters*, 40, 1978.

[91] R. T. Co and K. Harigaya. Axiogenesis. *Physical Review Letters*, 124, 2020.

[92] A. Ayad and G. Beck. Potential of the MeerKAT telescope to detect the stimulated decay of axion-like particles, 2022.

[93] F. Wilczek. Problem of Strong P and T Invariance in the presence of Instantons. *Physical Review Letters*, 40, 1978.